

AD-A172 032

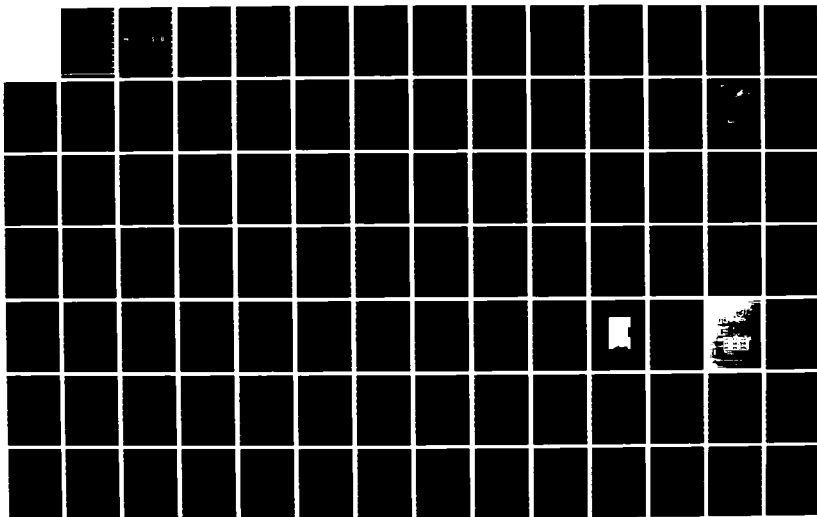
NOSE BOOM B-DOT SENSOR LOCATION OPTIMIZATION FOR NASA
F-106(U) DIKEHOOD ALBUQUERQUE NM V V LIEPA ET AL.
JUN 85 DC-FR-1026. 330-4A AFML-TR-85-94 F29601-82-C-0027

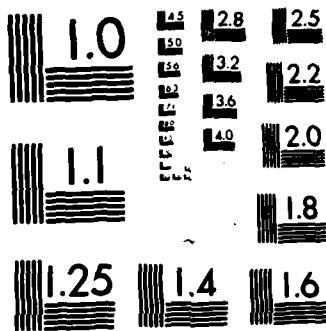
1/2

UNCLASSIFIED

F/G 1/3

NL





MICROCOPY RESOLUTION TEST CHART
NATIONAL BUREAU OF STANDARDS-1963-A

AD-A172 032

NOSE BOOM B-DOT SENSOR LOCATION OPTIMIZATION FOR NASA F-106

V. V. Liepa
M. W. Folkert

Dikewood, Division of Kaman Sciences Corporation
1613 University Boulevard NE
Albuquerque, New Mexico 87102

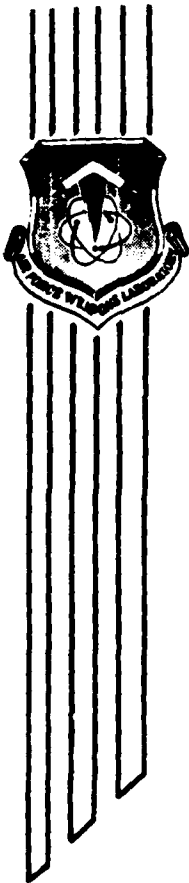
June 1986

Final Report

DTIC
ELECTE
SEP 19 1986
S D
D

Approved for public release; distribution unlimited.

AIR FORCE WEAPONS LABORATORY
Air Force Systems Command
Kirtland Air Force Base, NM 87117-6008



NOT FILED

This final report was prepared by Dikewood, Division of Kaman Sciences Corporation, Albuquerque, New Mexico, under Contract F29601-82-C-0027, Job Order 37630131, with the Air Force Weapons Laboratory, Kirtland Air Force Base, New Mexico. Captain Dennis J. Andersh (NTAA) was the Laboratory Project Officer-in-Charge.

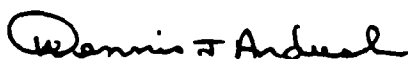
When Government drawings, specifications, or other data are used for any purpose other than in connection with a definitely Government-related procurement, the United States Government incurs no responsibility or any obligation whatsoever. The fact that the Government may have formulated or in any way supplied the said drawings, specifications, or other data, is not to be regarded by implication, or otherwise in any manner construed, as licensing the holder, or any other person or corporation; or as conveying any rights or permission to manufacture, use, or sell any patented invention that may in any way be related thereto.

This report has been authored by a contractor of the United States Government. Accordingly, the United States Government retains a nonexclusive, royalty-free license to publish or reproduce the material contained herein, or allow others to do so, for the United States Government purposes.

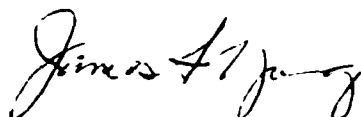
This report has been reviewed by the Public Affairs Office and is releasable to the National Technical Information Service (NTIS). At NTIS, it will be available to the general public, including foreign nationals.

If your address has changed, if you wish to be removed from our mailing list, or if your organization no longer employs the addressee, please notify AFWL/NTAA, Kirtland AFB, NM 87117 to help us maintain a current mailing list.

This report has been reviewed and is approved for publication.

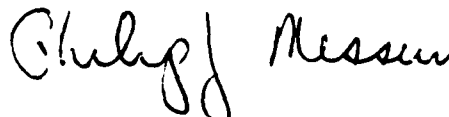


DENNIS J. ANDERSH
Captain, USAF
Project Officer



JAMES F. YOUNG
Maj, USAF
Chief, Applications Branch

FOR THE COMMANDER



PHILIP J. MESSURI
Maj, USAF
Chief, Aircraft and Missiles Division

DO NOT RETURN COPIES OF THIS REPORT UNLESS CONTRACTUAL OBLIGATIONS OR NOTICE ON A SPECIFIC DOCUMENT REQUIRES THAT IT BE RETURNED.

REPORT DOCUMENTATION PAGE

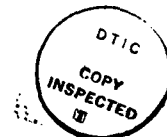
1a. REPORT SECURITY CLASSIFICATION Unclassified			1b. RESTRICTIVE MARKINGS		
2a. SECURITY CLASSIFICATION AUTHORITY			3. DISTRIBUTION / AVAILABILITY OF REPORT Approved for public release; distribution unlimited.		
2b. DECLASSIFICATION / DOWNGRADING SCHEDULE					
4. PERFORMING ORGANIZATION REPORT NUMBER(S) DC-FR-1026.330-4A			5. MONITORING ORGANIZATION REPORT NUMBER(S) AFWL-TR-85-94		
6a. NAME OF PERFORMING ORGANIZATION DIKEWOOD, Division of Kaman Sciences Corporation		6b. OFFICE SYMBOL (if applicable)	7a. NAME OF MONITORING ORGANIZATION Air Force Weapons Laboratory		
6c. ADDRESS (City, State, and ZIP Code) 1613 University Boulevard NE Albuquerque, New Mexico 87102			7b. ADDRESS (City, State, and ZIP Code) Kirtland AFB, New Mexico 87117-6008		
8a. NAME OF FUNDING / SPONSORING ORGANIZATION		8b. OFFICE SYMBOL (if applicable)	9. PROCUREMENT INSTRUMENT IDENTIFICATION NUMBER F29601-82-C-0027		
8c. ADDRESS (City, State, and ZIP Code)			10. SOURCE OF FUNDING NUMBERS		
			PROGRAM ELEMENT NO. 64711F	PROJECT NO. 3763	TASK NO. 01
11. TITLE (Include Security Classification) NOSE BOOM B-DOT SENSOR LOCATION OPTIMIZATION FOR NASA F-106					
12. PERSONAL AUTHOR(S) Liepa, Valdis V.; Folkert, Mathew W.					
13a. TYPE OF REPORT Final		13b. TIME COVERED FROM _____ TO _____		14. DATE OF REPORT (Year, Month, Day) 86 Jun	15. PAGE COUNT 116
16. SUPPLEMENTARY NOTATION					
17. COSATI CODES			18. SUBJECT TERMS (Continue on reverse if necessary and identify by block number) Nose Boom SEM Ground Plane Measurements Electric Field Sensors Free Space Measurements Lightning Measurements (over)		
FIELD	GROUP	SUB-GROUP			
01	03				
14	02				
19. ABSTRACT (Continue on reverse if necessary and identify by block number) Scale model experimental study and the results are presented in which the optimum location of a B-dot sensor to be mounted on an F-106 aircraft to measure the incident magnetic field in the direction of the aircraft fuselage is determined. In the study, measurements were performed in an anechoic chamber using a 1:72 scale F-106 model and a miniature B-dot sensor. Measurements were made in frequency domain using plane wave illumination. Amplitude and phase data were recorded for various locations in front of the aircraft over 118-4400 MHz (1.6--61 MHz full scale). The measurements were made with and without the model and hence, a comparison of the two measurements at a point provides the degree of field distortion or error for a given illumination.					
20. DISTRIBUTION / AVAILABILITY OF ABSTRACT <input checked="" type="checkbox"/> UNCLASSIFIED/UNLIMITED <input type="checkbox"/> SAME AS RPT <input type="checkbox"/> DTIC USERS			21. ABSTRACT SECURITY CLASSIFICATION Unclassified		
22a. NAME OF RESPONSIBLE INDIVIDUAL Capt Dennis J. Andersh			22b. TELEPHONE (Include Area Code) (505) 844-0327		22c. OFFICE SYMBOL NTAA

18. SUBJECT TERMS (Continued)

Magnetic Field Sensor
NASA F-106 Aircraft

CONTENTS

<u>Section</u>	<u>Page</u>
I. INTRODUCTION	1
II. FACILITIES, INITIAL STUDIES AND OPTIMIZATION CRITERIA	2
1. MEASUREMENT FACILITY AND INSTRUMENTATION	2
2. INITIAL STUDIES	6
3. DATA CONDITIONING	10
4. ERROR EVALUATION CRITERION	12
III. GROUND PLANE MEASUREMENTS	15
1. GROUND PLANE DESIGN	15
2. GROUND PLANE MODEL	17
3. MEASUREMENT PROCEDURE	18
4. GROUND PLANE DATA	23
VI. FREE SPACE MEASUREMENTS	57
1. MODEL, SENSORS, AND MEASUREMENTS	57
2. MEASUREMENTS AND DATA	59
V. INTERPRETATION OF RESULTS	80
IV. CONCLUSIONS AND RECOMMENDATIONS	86
APPENDIX A	87
APPENDIX B	101



Accession For	
NTIS CRA&I	<input checked="" type="checkbox"/>
DTIC TAB	<input type="checkbox"/>
Unannounced	<input type="checkbox"/>
Justification	
By	
Distribution/	
Availability Codes	
Dist	Avail and/or Special
A-1	

I. INTRODUCTION

In principle, the concept for determining the optimum location of an electromagnetic sensor on or near an airborne platform such that the sensor responds to the incident field and not to the total field is simple. All one needs to do is to determine a position for the sensor where the scattered component is minimum for all possible excitations and frequencies and locate the sensor at that position. If the sensor is polarization sensitive, only the responding components of the scattered field need to be determined. The problem could be approached analytically, numerically, experimentally, or any combination thereof. Here we present results of the scale model experimental study carried out in the University of Michigan Radiation Laboratory near field measurement facility using 1:72 scale models of F-106 aircraft.

In the anechoic chamber measurements of signal picked up by a miniature sensor that represents the boom 8-dot sensor were made with and without the F-106 model present in both the ground plane (Sec. 3) and the free space configurations (Sec. 4). In total, 17 different excitation situations were simulated. For each excitation nine points in the frontal region of the model were probed over 118-4400 MHz corresponding to 1.64-61.3 MHz at full scale. Since the main aircraft resonances occur at 7.4 MHz and 13.7 MHz for the fuselage and the wings, respectively, the resonances fall well within the frequency range covered in the measurements. For each excitation and measurement location (153 in total) an error due to scattering from the model is determined. In general, the results agree with expectations: the further the sensor is away from the aircraft the smaller is the error and the error is least when the sensor is located in the plane of the wings of the aircraft. The important contribution of this study is the determination of actual errors that can be anticipated for the given sensor location and excitation. In general, these errors are small, mainly due to the almost ideal geometry of the F-106 aircraft that has minimal scattering in the forward region. The assessment and discussion of errors is presented in Section 5.

Other studies performed under this study include (a) SEM studies of F-106 aircraft, and (b) lightning simulation studies in the frequency domain. These are presented in the appendices.

II. FACILITIES, INITIAL STUDIES AND OPTIMIZATION CRITERIA

1. MEASUREMENT FACILITY AND INSTRUMENTATION

The University of Michigan field measurement facility (Ref. 1), that has been used almost exclusively for measurements of aircraft exterior field coupling to the incident electromagnetic field (Refs. 2, 3), is "tailor made" for the present study. A block diagram of this facility is shown in Figure 1. The system is a CW one in which the frequency is swept (stepped) over a wide range. A key part of the facility is a tapered anechoic chamber approximately 50 feet in length with the rectangular test region 18 feet wide and 12 feet high. Its rear wall is covered with 72-inch high-performance pyramidal absorber, with 18-inch material used on the side walls, ceiling and most of the floor. The material in the tapered section (or throat) is two-inch hair-flex absorber. The chamber can be thought of as a lossy-wall horn antenna terminated by the rear wall. The signal is launched from a single exponentially tapered broadband antenna located at the apex of the chamber. The antenna is fixed, and since the radiated signal is horizontally polarized, the pseudoplane wave in the center ('quiet zone') portion of the test region is also horizontally polarized.

The instrumentation is centered around a Hewlett-Packard 8410B network analyzer, and is computer controlled. An HP9830A computer controls the frequency to be generated, switches in the appropriate power amplifiers and low-pass filters, and reads and stores the amplitude and phase of the signal picked up by the sensor. During a run, the frequencies are typically stepped from 118 to 4400 MHz. Because of the limited memory size of the computer, this frequency range is recorded in four bands: 118 to 550 MHz (in 4.8 MHz steps), 550 to 1100 MHz (in 4.8 MHz steps), 1100 to 2000 MHz (in 9.6 MHz

1. EMP Interaction: Principles, Techniques and Reference Data, AFWL-TR-80-402, pp. 267-276, December 1980, EMP Interaction Note 2-1.
2. Liepa, V.V., Y. Hyun, "Free Space Scale Model Measurements of the F-14A," University of Michigan Radiation Laboratory Report No. 017463-4-T; Interaction Application Memo 38, March 1982.
3. Liepa, V.V., "Free Space Mode FB-111A Scale Model Measurements," University of Michigan Radiation Laboratory Report No. 017463-5-T; Interaction Application Memo 35, July 1982.

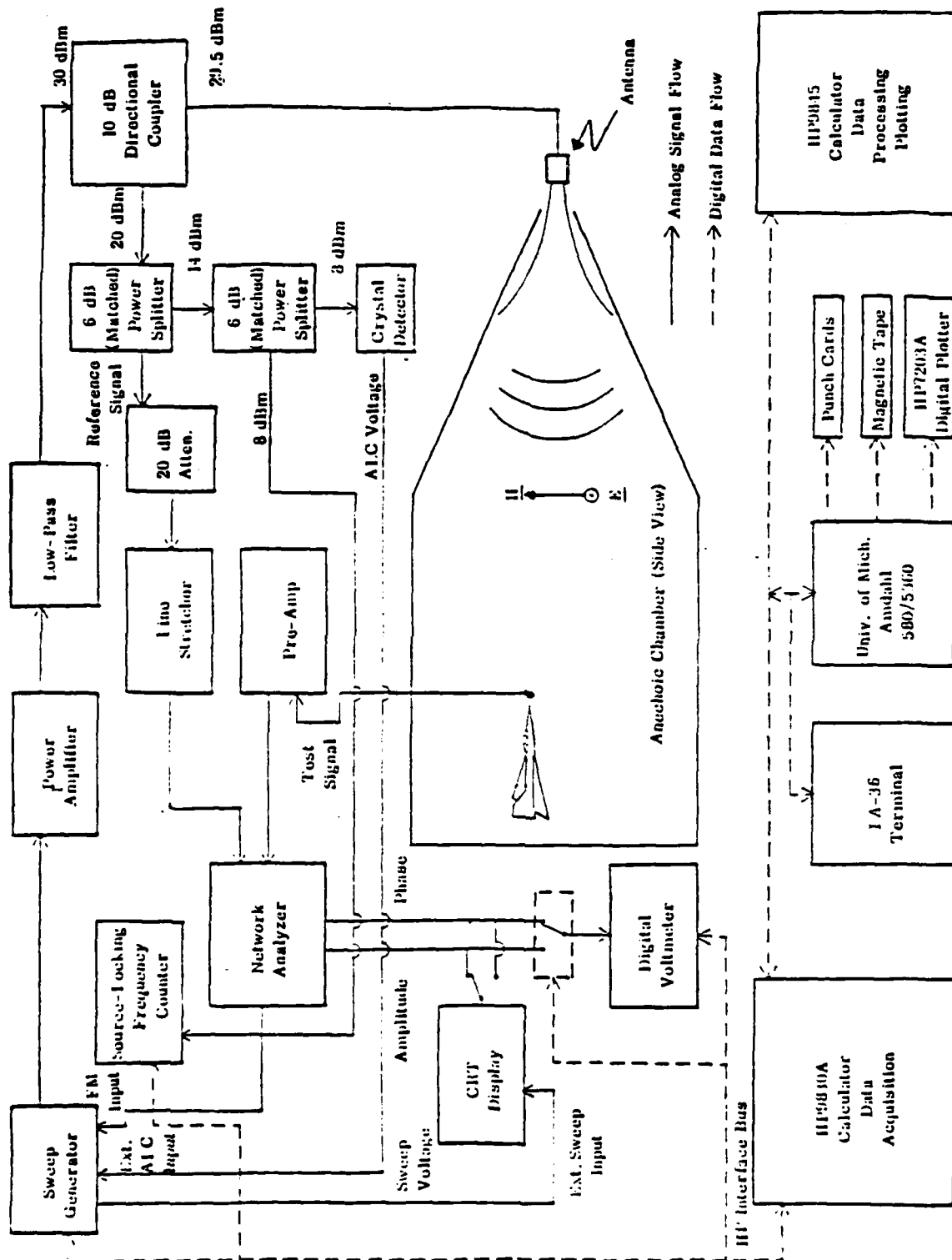


Figure 1. Block diagram of the facility with model positions for nose-on incidence.

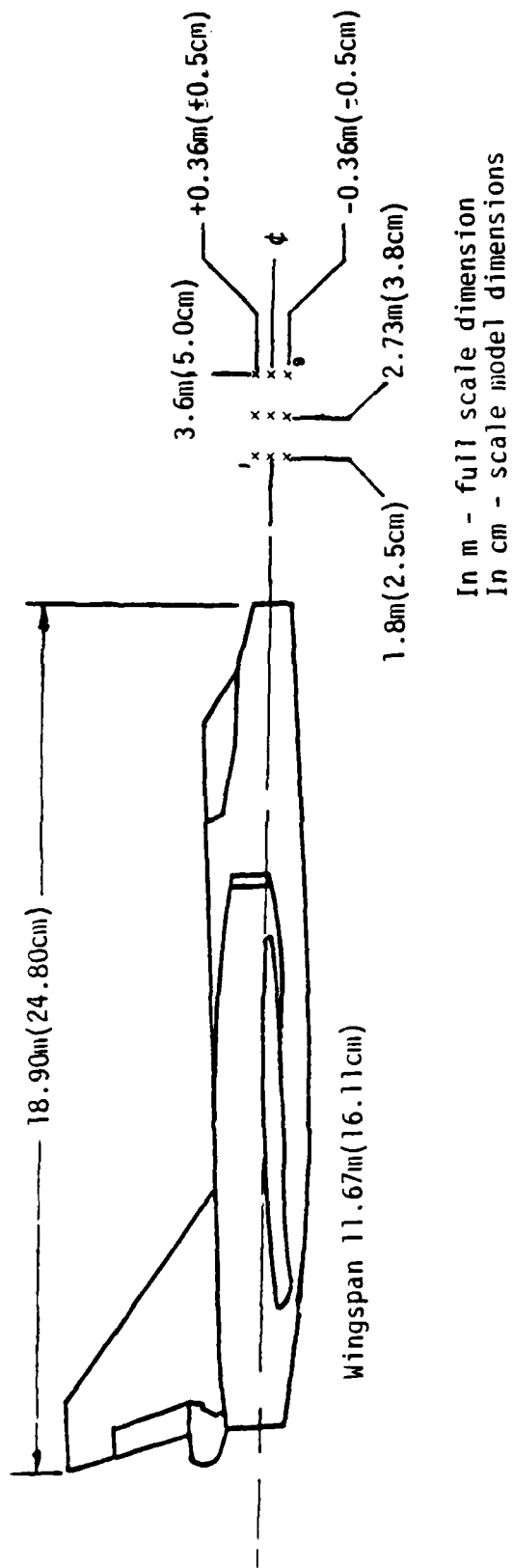
steps), and 2000 to 4400 MHz (in 16.8 MHz steps). The data from each band are stored by the HP9830A computer on a cassette for later transfer to an HP9845B computer which processes and plots the data. If substantial processing or computation is involved, or if a need exists to write the data on standard computer tape, the data are transmitted to the central University of Michigan AMDAHL/5860 (IBM compatible) computer.

The signal measured by the network analyzer as picked up by a miniature probe or a sensor is a function not only of the measured field but of the entire facility, including the probe, chamber, antenna, amplifiers and cabling, and it would be virtually impossible to separate and to correct for the contributions of each. The approach taken in this study is to apply an appropriate calibration or normalization whereby the response of the facility and the instrumentation are eliminated. In short, a measurement is made with an airplane model present (test measurement) and then repeated with the airplane model removed (calibration). Taking the ratio of the measurements produces the required data and cancels out the facility responses and measurement instrumentation responses.

Using the fundamental properties of electromagnetic scattering by simple symmetric bodies, Giri and Baum (Ref. 4) have provided guidelines for placement of the sensors on or near the aircraft, but due to their nonexact analysis, their error estimates are qualitative for most of the frequency ranges of interest. Using their guidelines and the physical constraints imposed by the safety and performance consideration of the F-106 aircraft, the B-dot sensor location was limited to the frontal regions of the aircraft with the sensor axis parallel to the fuselage and in the plane of symmetry of the aircraft.

Our task was to find the optimum position for the sensor, limited to the frontal region of the aircraft. Figure 2 shows a side view of the aircraft with the nine measurement locations indicated by x, where the measurements were made for specified illuminations with and without the model present.

-
4. Giri, D.V. and C.E. Baum, "Airborne Platform for Measurement of Transient of Broadband CW Electromagnetic Fields," Sensor and Simulation Note 284, May 1984.



In m - full scale dimension
 In cm - scale model dimensions

Figure 2. Locations of test points used in scale model measurements; all measurement points lie in the plane of symmetry of the aircraft.

These locations were chosen to cover the area within which the sensor placement is feasible and have been (theoretically) investigated by Giri and Sands (Ref. 5).

2. INITIAL STUDIES

In order to better understand the results of nose area measurements and interpret the various oscillations in the frequency response, surface current measurements were first made to determine the fuselage and the wing resonances of the F-106A using small current loops (Refs. 2,3). Figure 3 shows the normalized axial current density ($\underline{J} = \hat{n} \times \underline{H}$, A/m) on top of the fuselage for the case of top incidence, E-parallel to the fuselage. The location is at midpoint, measured horizontally halfway between the bulkhead and the top of the vertical fin. The (top) curve shows the fuselage resonates at 7.2 MHz and reaches a value of about 10.5 at the peak (relative to the incident field). Note the model used was without the Pitot boom and the radome. The lower curve shows the corresponding phase, with reference plane at the point of the measurement. The physical optics (P.O.) estimates are indicated by the dashed lines, which are twice the incident (magnetic) field for the current and zero degrees for the phase.

Figure 4 shows the wing current measured on the bottom of the fuselage along the line of the flap joins, for bottom incidence, E-perpendicular to the fuselage. In the model the flaps were rigid, without a gap between the wing and the flap. Note the wing resonance occurs at 13.7 MHz, with the maximum current reaching about 3.5.

The basic dimensions of the F-106A are shown in Figure 5. Using the fuselage length of 17.67 m (bulkhead to tail) and the resonant frequency of 7.4 MHz, the fuselage resonance length is 0.436 wavelength, which is as expected for a relatively fat body. The wing resonance, however, occurs when the wing span is 0.533 wavelength (wing span 11.67 m, resonant frequency 13.7 MHz); this contradicts the basic past observations that most of the main resonances occur when the body dimensions are 0.4 to 0.47 wavelengths. Perhaps in this case the resonance observed is not solely due to the mode supported by the wings but characterized by the wing and the vertical fin characteristic dimensions.

5. Giri, D.V., and S.H. Sands, Design of Incident Field B-Dot Sensors for the Nose Boom of the NASA F-106B Aircraft, AFWL-TR-83-141, April 1984.

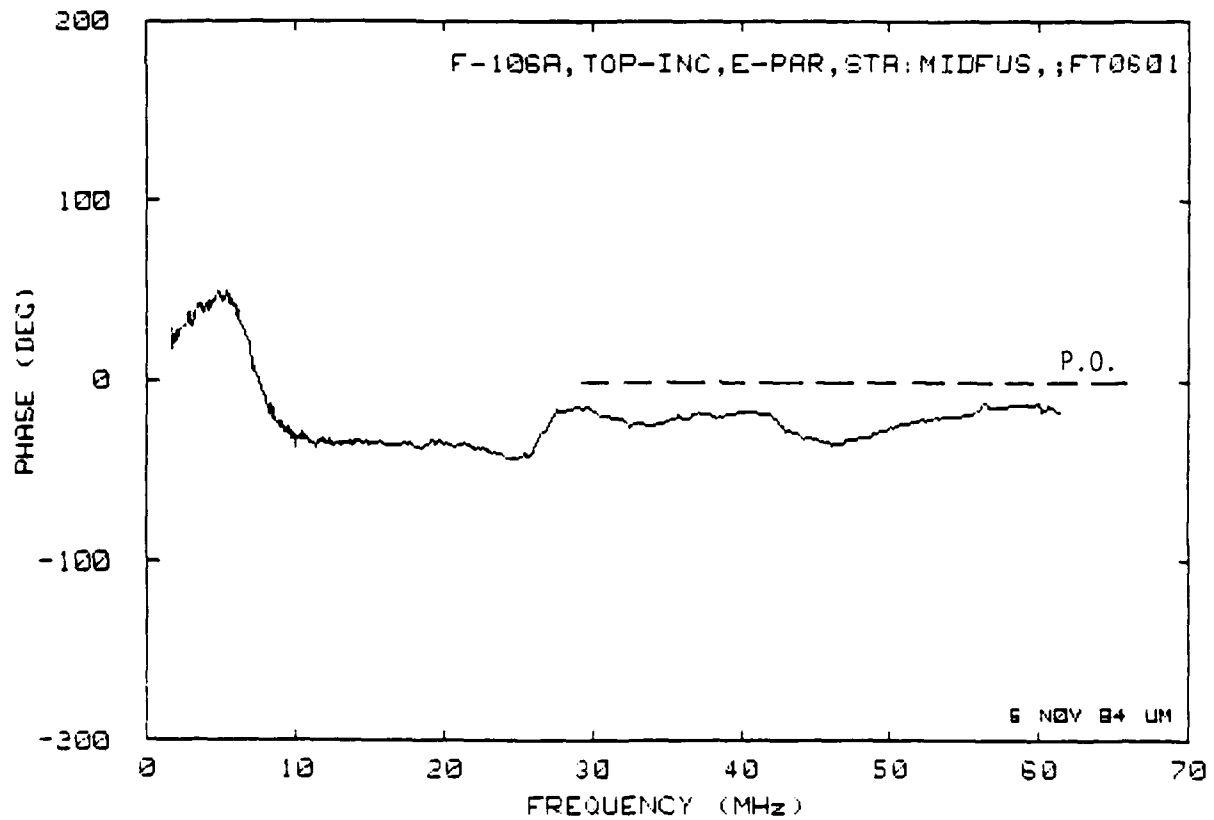
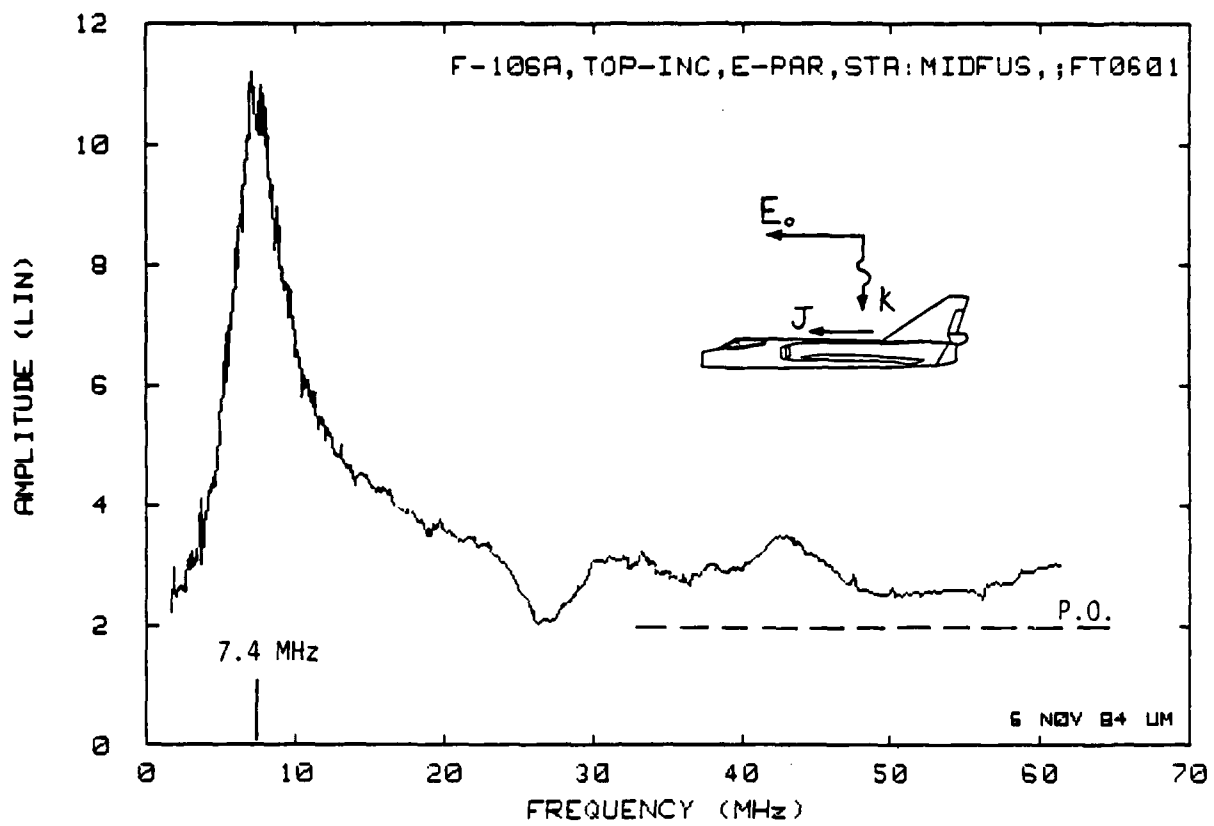


Figure 3. Surface current for F-106A on top of the fuselage, top incidence E-parallel to fuselage.

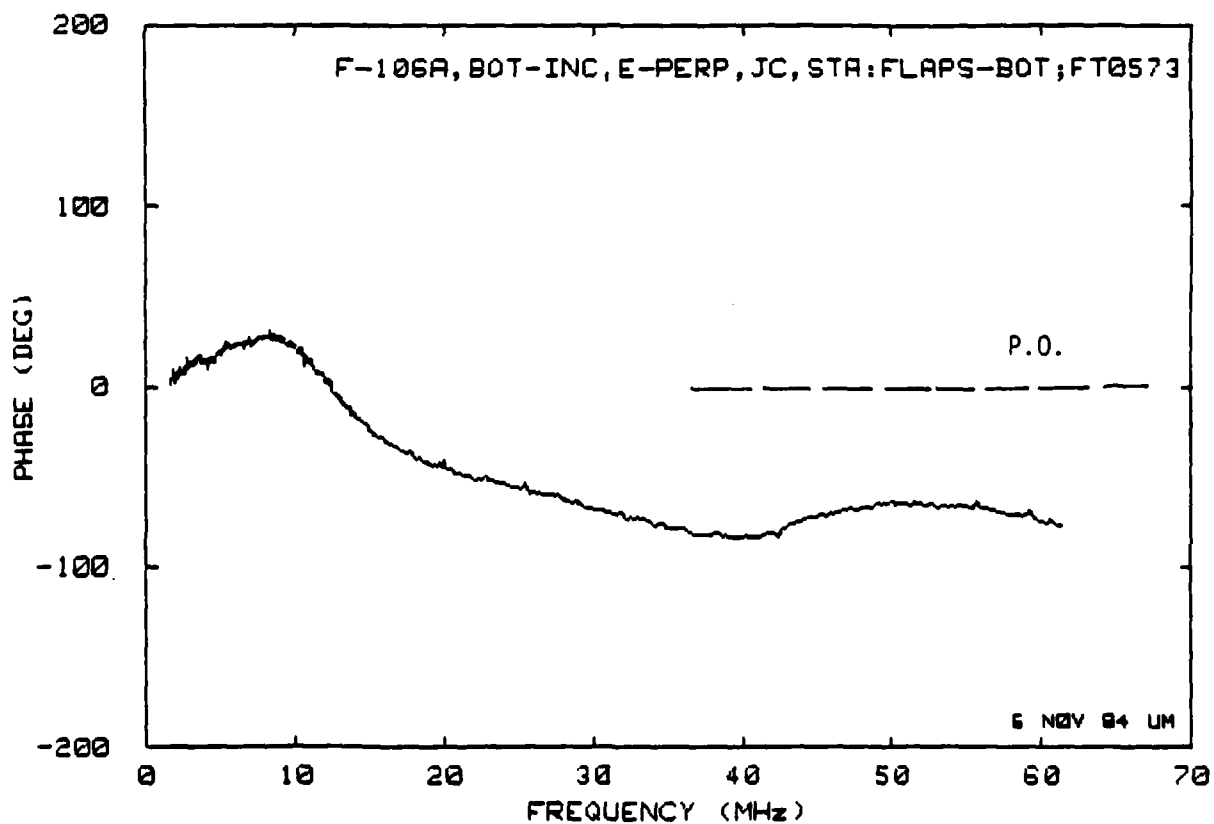
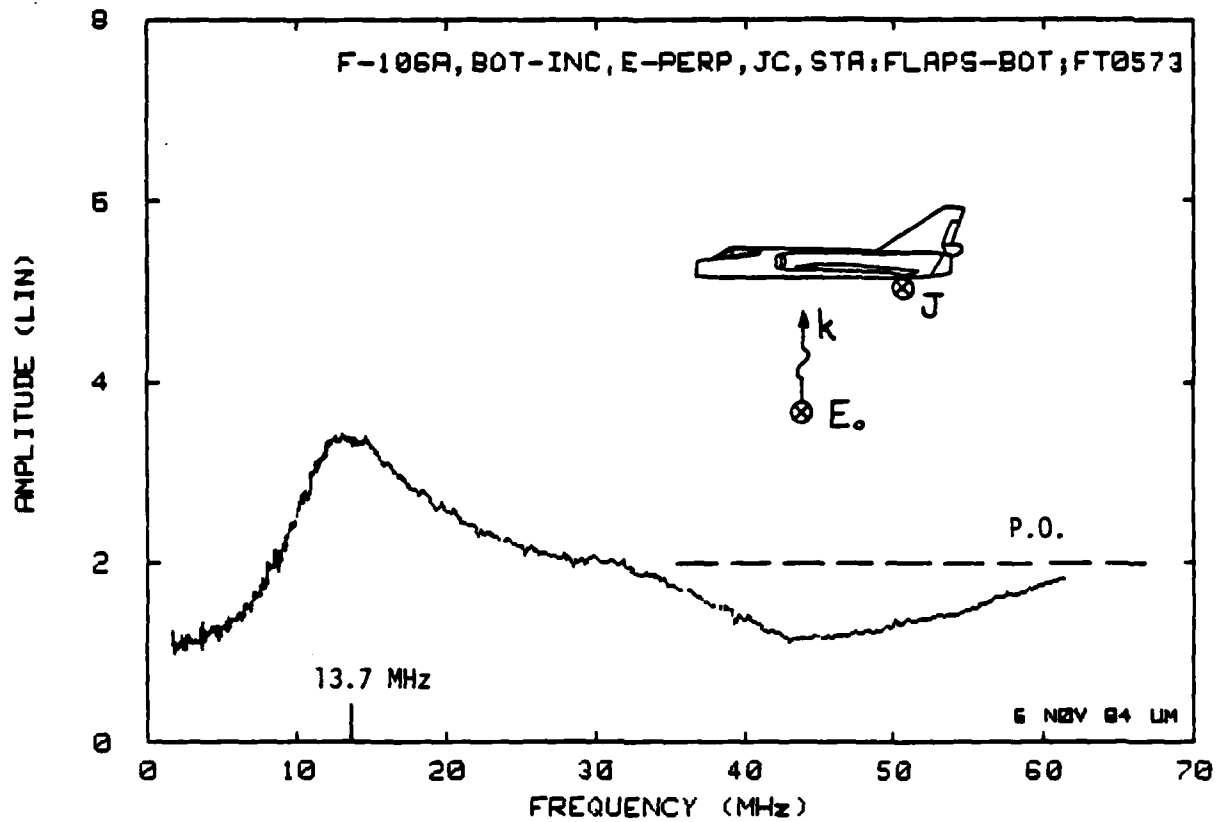


Figure 4. Surface current for F-106A on bottom of the wings, bottom incidence E-perpendicular to the fuselage.

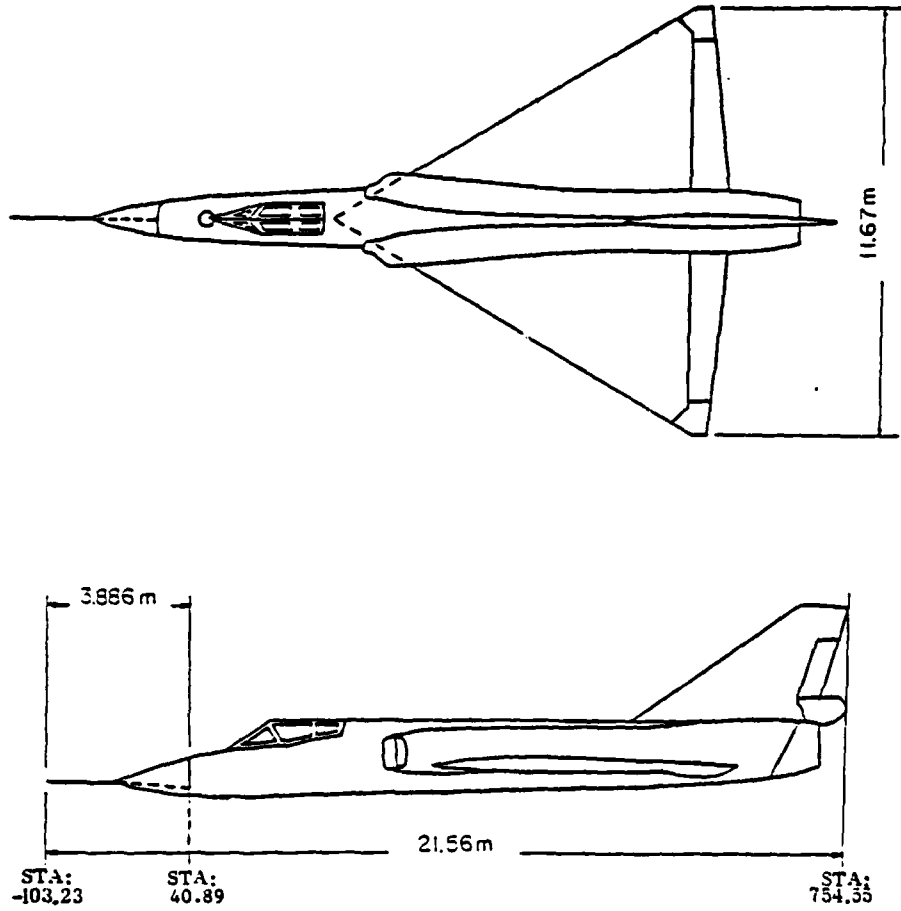


Figure 5. Basic dimensions of F-106A.

3. DATA CONDITIONING

The data plotted in Figures 3 and 4 are as measured without any smoothing or filtering. As seen, it is somewhat noisy at the lower end, and shows some drop outs and small oscillations that definitely are not a part of aircraft response. Hence, some smoothing is justifiable and when done properly will improve the accuracy as well as the appearance of the data. All the data used for optimization of B-dot sensor was filtered using program FILTR5* that is based on the convolution principle and convolves a sinc $(=(\sin x)/x)$ function with the frequency data. The convolution of the sinc function with frequency is equivalent to gating or multiplying the equivalent time domain signal by a window function. For filtering the data (Sec. 3 and 4), 30 cycles were selected as the cut-off frequency for the oscillations on the frequency data. This is equivalent to a range gate of about 130 m or six aircraft lengths. In relation to model measurements (1/71.8 scale modeling) this corresponds to a distance of 1.8 m which is also the distance from the model to the ceiling or to the floor in the chamber. The model to side wall distance is about 2.2 m and hence filtering also removes these interactions if such exists.

On the other hand, if a model shows a high Q response, filtering can also decrease the resonant peak and create erroneous data. Note, a resonance can be treated as a signal bouncing back and forth on the body, and if this bouncing continues longer than the time window, a part of the response would be cut off resulting in a lower peak. It is therefore essential that filtering be tested on the worst case data - high noise and high resonance peaks (or high Q response) to determine the acceptable filtering parameters.

Figure 6 shows the worst case data that was obtained in this study. The measurement has rather high (chamber) interference, dropout noise, and the highest model interaction (i.e., deviation from unity) observed of all the situations measured. The corresponding filtered plot is shown in Figure 7. Note, the noise, the spikes, and the fast wiggles have disappeared, but the major features that arise from the model interaction have remained intact.

* In-house program developed for HP9845T to process the data.

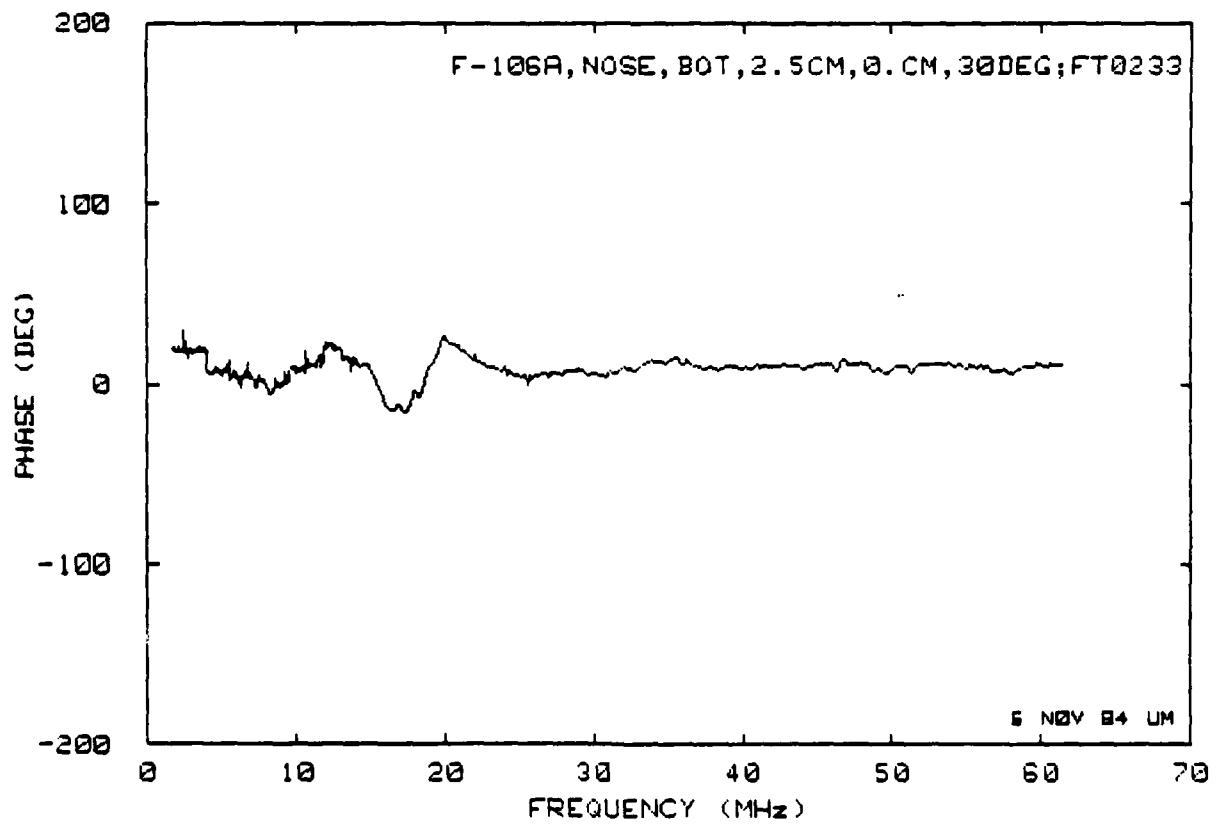
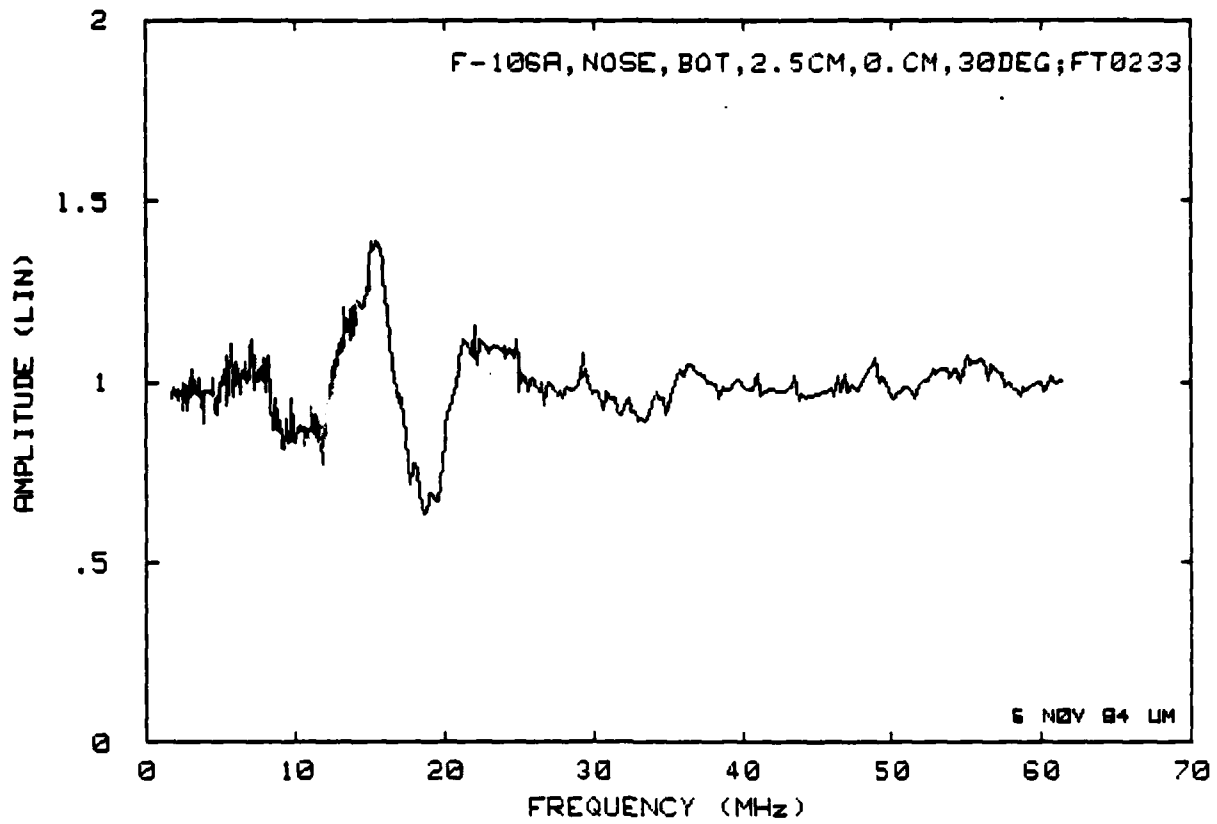


Figure 6. Worst case data measured. (Refer to Data Set 4.4(a) for the particular situation.)

4. ERROR EVALUATION CRITERION

Depending on direction of illumination, polarization, and the location of the sensor, the data recorded varies from the worst case shown in Figure 7 to almost a straight line (no interaction). In total there were 156 curves generated and in order to categorize or evaluate these curves, error values E_1 and E_2 are defined giving a pair of numbers for each data curve. These error definitions follow from average and rms function definitions and are defined (in percent) as

$$E_1 = \frac{1}{\Delta F} \sum_{n=2}^N \left| \frac{v(f_n)}{v_0(f_n)} - \frac{v_1(f_n)}{v_0(f_n)} e^{iKf_n} \right| \Delta f_n \cdot 100 \quad (1)$$

$$E_2 = \sqrt{\frac{1}{\Delta F} \sum_{n=2}^N \left| \frac{v(f_n)}{v_0(f_n)} - \frac{v_1(f_n)}{v_0(f_n)} e^{iKf_n} \right|^2 \Delta f_n} \cdot 100 \quad (2)$$

where

N = the total number of data points (118-4400 MHz, $N = 450$)

f_n = the measurement frequency

ΔF = the total frequency interval

$\Delta f_n = f_n - f_{n-1}$, sampling interval

$v(f_n)$ = the signal measured with the model present

$v_1(f_n)$ = the signal measured without the model

$v_0(f_n)$ = the signal measured without the model, but the sensor rotated for maximum signal and

K = phase correction constant

Note that in a case such as the top incidence, H-parallel to the fuselage $v_0(f_n) = v_1(f_n)$, whereas for top incidence, E-parallel to the fuselage, $v_0(f_n) \neq v_1(f_n)$. In fact, $v_1(f_n) = 0$, and is only non-zero due to the reflection of the signal from the walls of the anechoic chamber, the support pedestal, and other imperfections. The phase term K was added to allow correction for the linear change in the phase between the model and without the model data that results from dimensional changes in the chamber, cabling

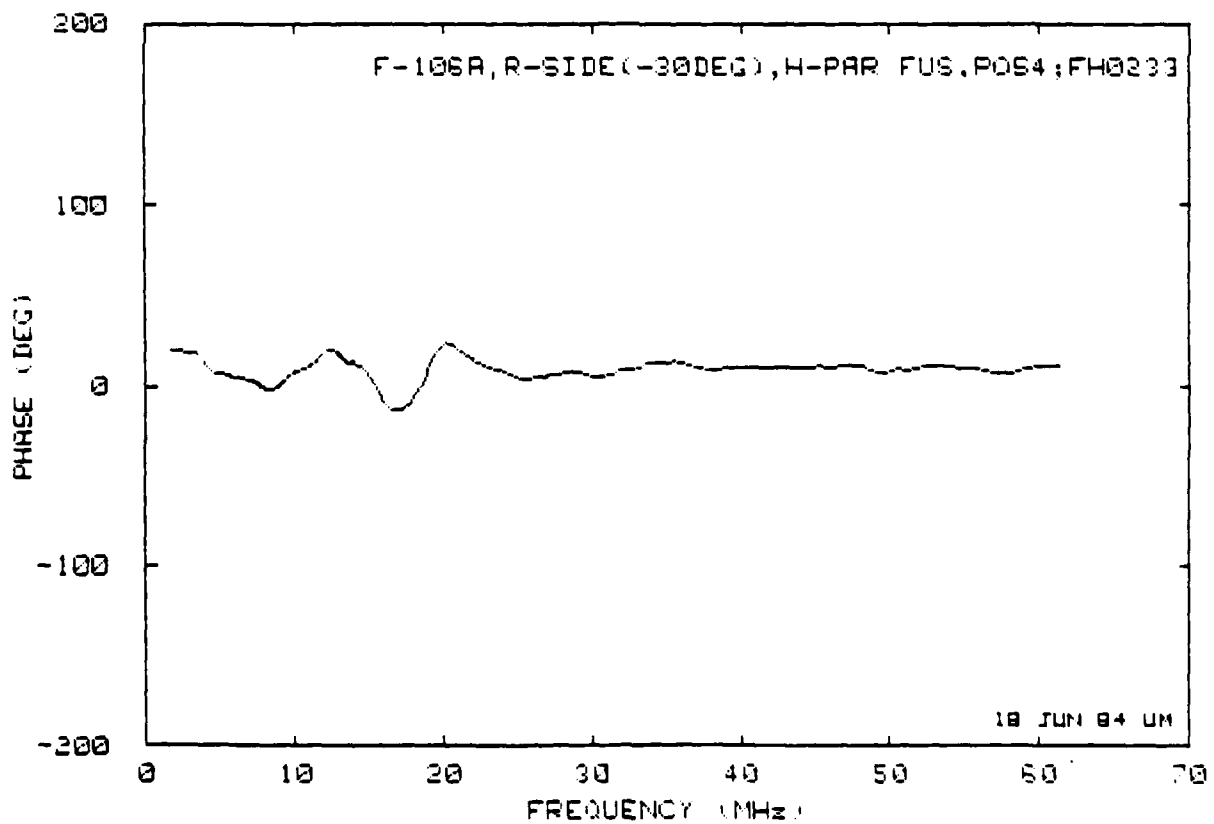
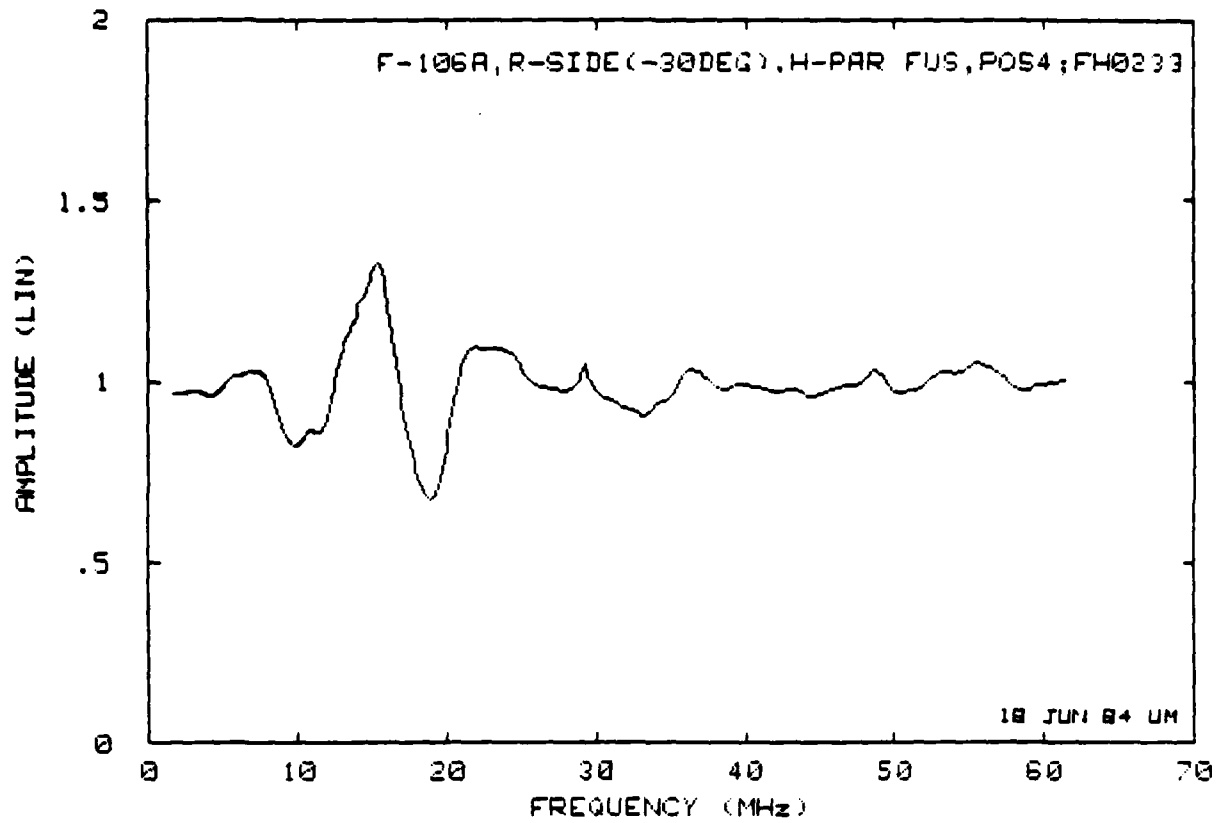


Figure 7. Data of Fig. 2.6 after Filtering.

and even equipment due to changes in temperature, humidity, etc. To minimize such drift, the measurement sequence consisting of one illumination and nine measurement points is completed in the same day, and even then electrical changes in the system occurred which resulted in phase drifts on the order of 10 to 20 degrees. These can be related to a few millimeter changes in the chamber or cable dimensions. In the time domain, a linear phase shift corresponds to the time delay (or advance) with no change in pulse shape, and hence one is justified in adjusting the linear phase term K to minimize the error quantities E_1 and E_2 . Examination of the phase plot in Figure 7 shows a slight rise in phase with the frequency indicating drift in the equipment. If not corrected for this slope, $E_1 = 18$ percent and when corrected, $E_1 = 11$ percent.

For processing the data to evaluate E_1 and E_2 and optimize the phase K , a program SUBTR5*, based on Equations 1 and 2, was written and used.

* In-house program developed for HP9845T to process the data.

III. GROUND PLANE MEASUREMENTS

When a model to be measured is symmetric about a plane and the excitation is such that incident electric field vector is perpendicular to this plane, measurements can be made using one-half the model mounted on a large metal plate. The plate should be large enough to avoid errors caused by edge diffraction and the model-edge interactions. The main advantage of using an image or ground plane technique is to avoid exposing probe leads to the incident fields to interfere with the measurements. In addition, the ground plane has the tendency to improve the field distribution by enforcing that the electric field be perpendicular to the metal plate. On the other hand, the disadvantage of using a ground plane is that it limits the measurements to symmetric bodies and limits the illumination to the case of incident electric vector perpendicular to the ground plane if the free space plane wave incidence is to be simulated.

Because image plane measurements do provide, in general, more accurate results, measurements that were appropriate to such configuration were performed using image plane, and the remaining ones were performed using the free space technique (see Sec. IV).

1. GROUND PLANE DESIGN

As mentioned in Section II the anechoic chamber simulates a free space environment and, since it would require considerable modification to create a ground plane chamber, it was necessary to construct a ground plane that could be inserted into the test region of the present chamber as indicated in Figure 1. In our chamber the incident E-field propagation direction is fixed and the E-field is horizontally polarized. It is therefore necessary to have the ground plane vertical, with the capability of rotating the model relative to the incident field.

For the reasons given below, we chose a circular aluminum ground plane with a resistive sheet extension as shown in Figure 8. The aluminum disk is 1.53 m (5 ft) in diameter and is supported vertically by a wooden stand at a height midway between the floor and ceiling of the chamber, aligned such that the incident field is almost edge-on to the disk. In practice, because of the

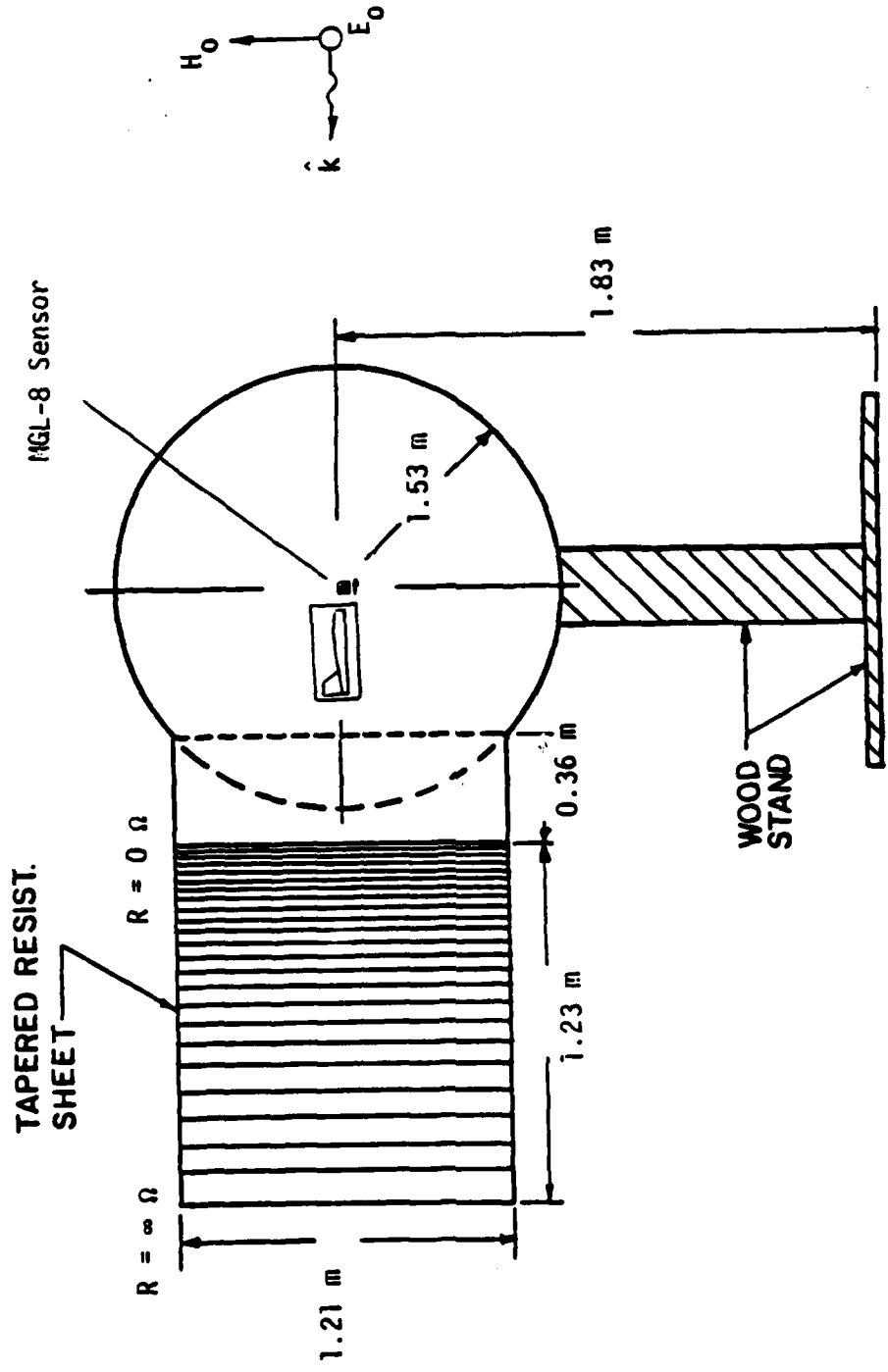


Figure 8. Circular ground plane configuration with resistive sheet extension.

small stray (scattered) signals that are always present in a measurement situation, the ground plane was positioned 5 deg (counterclockwise about a vertical axis) to insure a uniform excitation over the working area of the disk.

It was the original intent to permanently attach the model to the ground plane and to produce the different excitations by rotating the aluminum disk about a horizontal axis. This proved to be impractical, partly because of slight warping and irregularities in the ground plane, but more because of the sheer size and weight of the structure. It was therefore decided to keep the disk stationary and permit the rotation of the model in discrete steps.

Although the disk was not rotated as originally planned, it is believed that the circular shape is still desirable. With any finite ground plane there is the possibility of edge waves which can perturb the uniform field characteristics of an infinite structure and, when the model is introduced, an edge-model interaction can occur which would not be eliminated by the field normalization employed. By virtue of the circular geometry, whatever interaction does occur should, to a first order, be independent of the model rotation.

However, for a given illumination a situation can exist where a traveling wave can be excited on the ground plane. This wave travels in the direction of the incident wave (from right to left in Fig. 8), and can reflect from the left edge and cause disturbance in the field. To minimize such reflections a resistive sheet structure was built and attached to the rear edge as shown in Figure 8. The sheet was curved towards the back to hide the rear edge and was constructed by applying layers of resistive paint to art paper supported by a wooden frame. By varying the paint thickness the resistivity could be controlled, and the final structure had a resistivity which started at about $10 \Omega^2$ at the metal edge and increased uniformly to about $1000 \Omega^2$ at the outer (left-hand) edge.

2. GROUND PLANE MODEL

The ground plane model was constructed from a 1/72 scale plastic model (Hasegawa, No. 1054) which, after assembly, was cut in half and attached to a thin aluminum sheet approximately 0.07 cm thick. The model was then sprayed

with silver paint to simulate the metallic characteristics of the actual aircraft. The use of metal plate insured ruggedness which was necessary for frequent repetitive use of the model on the ground plane.

To mount the model on the ground plane, aluminum tape was used to tape the plate on which the model was mounted. This tape also assured a good electrical continuity between the plate and the ground plane.

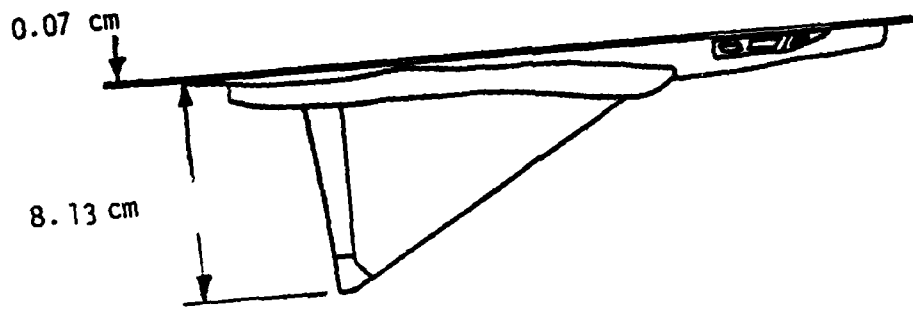
Figure 9 illustrates the model and gives its dimensions. The actual scale factor of the model is 1:71.8 and is based on the ratio of the wingspan dimensions which are the critical ones for E-perpendicular to the fuselage polarization. Figure 10 shows photographs of the model.

3. MEASUREMENT PROCEDURE

The central portion of Figure 8 depicts the model and the probe mounting on the ground plane. The probe, an MGL-8, is mounted at the center of the circular ground plane, and the model with its mounting plate is repositioned on the ground plane to attain the nine probe positions relative to the aircraft as given in Figure 2.

The measurements were made for incidence of (a) Nose-on ($\theta = 180$ deg), (b) Top ($\theta = -10$ deg), (c) Tail-on ($\theta = 0$ deg), (d) Below Tail-on ($\theta = -10$ deg) and (e) Above Tail-on ($\theta = 10$ deg). For cases (a), (b) and (c) as the model was rotated so was the probe to measure the magnetic field component parallel to the fuselage. The cases (d) and (e) were included in the study to verify if a slight tilt of the sensor axis can reduce further the scattering errors from the wings. For convenience in performing the measurements the model was tilted rather than the probe and is justifiable due to the broad (dipole) pattern of the sensor.

In addition to the movement of the model relative to the probe (pos 1 through 9) and the rotation of the model with the sensor to obtain the incidences (a) through (e) given above, the ground plane was also rotated about its vertical axis through $\phi = 5, 20, 45$ and 60 deg. The $\phi = 5$ degrees measurements correspond to the free space plane wave incidence case, and the other cases could imply a dual plane wave incidence exciting only the anti-symmetric current components on the model. Figure 11 defines the θ and ϕ variables.



thin aluminum sheet

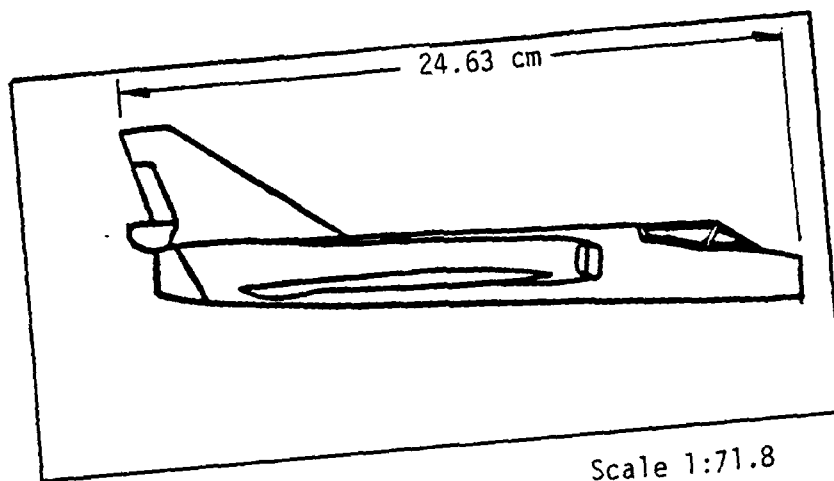
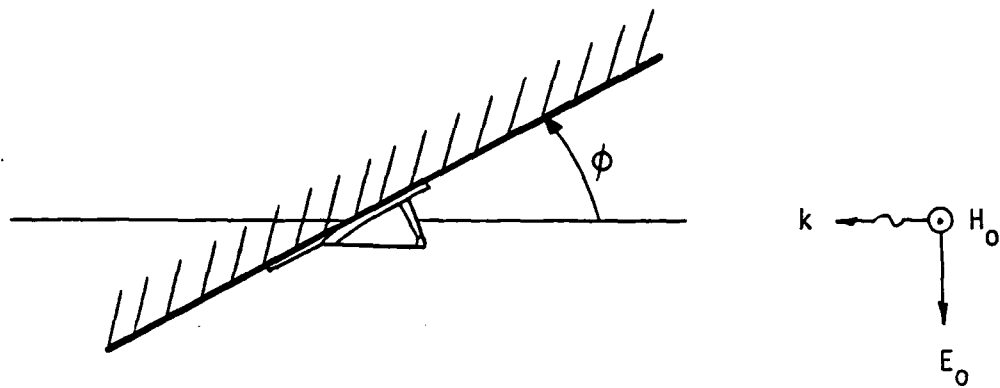


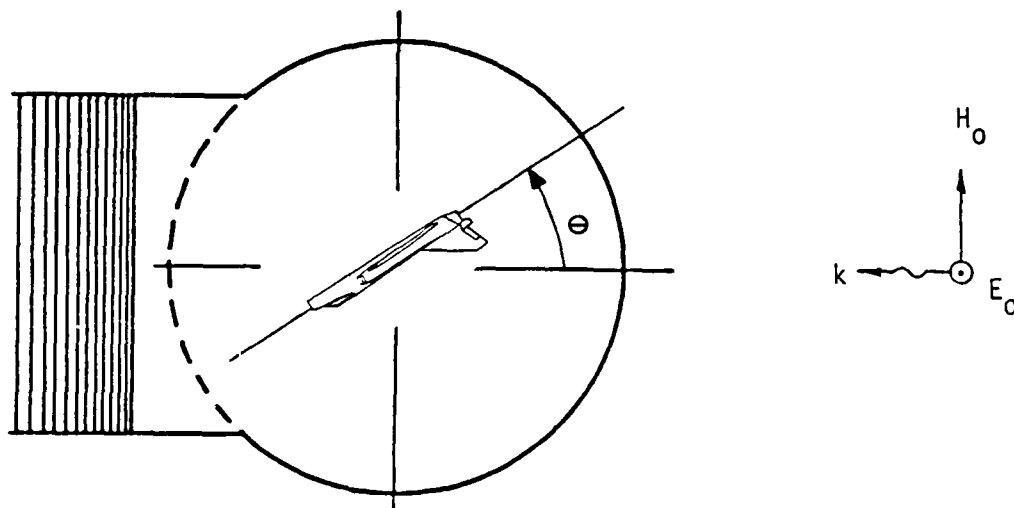
Figure 9. Aircraft model used for the measurements.



Figure 10. Photographs of the ground plane model. Top: model mounted on a thin aluminum plate. Bottom: the same mounted on the ground plane for nose-on incidence H-vertical. Note the MGL-8 sensor near the bulkhead.



Top view (for $\theta = 0$ degrees)



Side view (for $\phi = 0$ degrees)

Figure 11. Ground plane and model rotational angles.

As a test of the facility and the MGL-8 sensor, the sensor was first mounted at the center of the ground plane and the signal recorded as a function of frequency for angles of θ from 0 to 360 deg in increments of 15 deg. The amplitude curves versus θ exhibited sinusoidal variation, but there was a slight shift in the curve implying that the incident signal is not exactly propagating horizontally, but on the average arrived along the line $\theta = -2$ deg. This could be a result of antenna placement below the centerline or a difference in the absorber materials between the top and the bottom in the tapered feed region of the chamber. As the result of this analysis, the $\theta = 0$ deg specification of the model rotation is not exactly horizontal but tilted 2 deg clockwise.

Consider next the procedure for measuring the case of nose-on incidence ($\theta = 180$ deg and $\phi = 5$ deg), the situation for which the layout of Figure 8 is applicable. The loop axis for the sensor is horizontal, but the incident magnetic vector is vertical, a case where there should be no signal (ideally) received by the sensor. Next refer to Equations 1 and 2 and recall the measurements needed to compute the errors E_1 and E_2 . These are:

$v(f_n)$ = sensor output voltage with the model present

$v_1(f_n)$ = sensor output voltage without the model (invisible aircraft)

$v_0(f_n)$ = sensor output voltage with the sensor rotated to measure the maximum magnetic field (without aircraft)

Also refer to Figure 2 showing the placement of the model relative to the sensor. Recall that the sensor is fixed and the model is moved to obtain the needed positioning. For the ground plane measurements the numbers 2.5, 3.7 and 5 cm refer to the distance from the center of the sensor to the bulkhead of the model, and the numbers +0.5 and -0.5 cm refer to the position of the model relative to the sensor. Thus, the set (5.0, +0.5) corresponds to the sensor position 9 (Fig. 2). (For the free space measurements presented in Section 4 the convention was changed whereby the numbers +0.5 and -0.5 cm refer to the position of the sensor relative to the model and hence the set [5.0, +0.5] would correspond to the sensor pos 3.)

In carrying out the measurement sequence the voltages $v(f_n)$ are first recorded for four or five sensor positions, then $v_1(f_n)$ for the case without

the model, and then followed by $v(f_n)$ measurements for the remaining positions. If the sensor needs to rotate 90 degrees to measure the incident field $v_0(f_n)$, such measurement is made last. To minimize the measurements errors due to equipment drift and chamber changes due to the temperature, humidity, etc., the measurements sequence is completed in the same day.

The data are processed using program SUBTR5 based on Equations 1 and 2. For given position, say position 1, minimum E_1 is computed by varying the K. The search was done manually, and typically took on the order of five educated tries to arrive at min E_1 with K increments of 0.01 which correspond to a mere 0.6 deg ambiguity at the maximum measurement frequency.

4. GROUND PLANE DATA

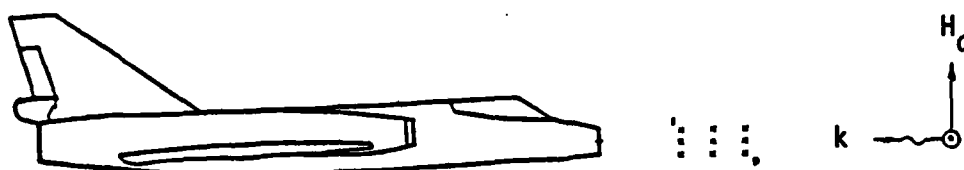
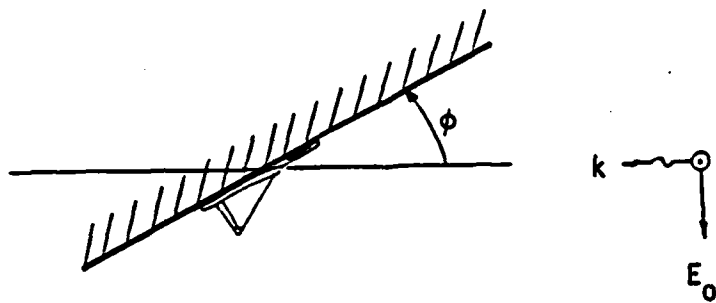
The results are presented for 11 orientations or illuminations of the model. For each situation there were at least 10 data runs generated, 9 for the different probe positions and at least one for the reference, without the model present. For each situation studied, a summary sheet is presented giving E_1 and E_2 error values, data file names, reference (without airplane) file names, and other notes that may be essential for retrieval of the data from storage tapes for further analysis analysis. Each summary sheet is followed by two response curves for sensor positions 4 and 6, respectively. These give a descriptive indication of the behavior of the received signal as a function of frequency for the particular excitation. Curves for the other sensor positions were not included, but data can be provided to subsequent users, if needed, by the authors.

Table 1 summarizes the data presented for the ground plane measurements.

TABLE 1. SUMMARY OF GROUND PLANE MEASUREMENTS

ϕ \ / \ θ	Nose-on $\theta = 180^\circ$	Top $\theta = 90^\circ$	Tail-on $\theta = 0^\circ$	Tail-on $\theta = -10^\circ$	Tail-on $\theta = 10^\circ$
0*	Set 3.1	Set. 3.2	Set 3.3	Set 3.4	Set 3.5
20	Set 3.6	Set 3.9			
45	Set 3.7	Set 3.10			
60	Set 3.8	Set 3.11			

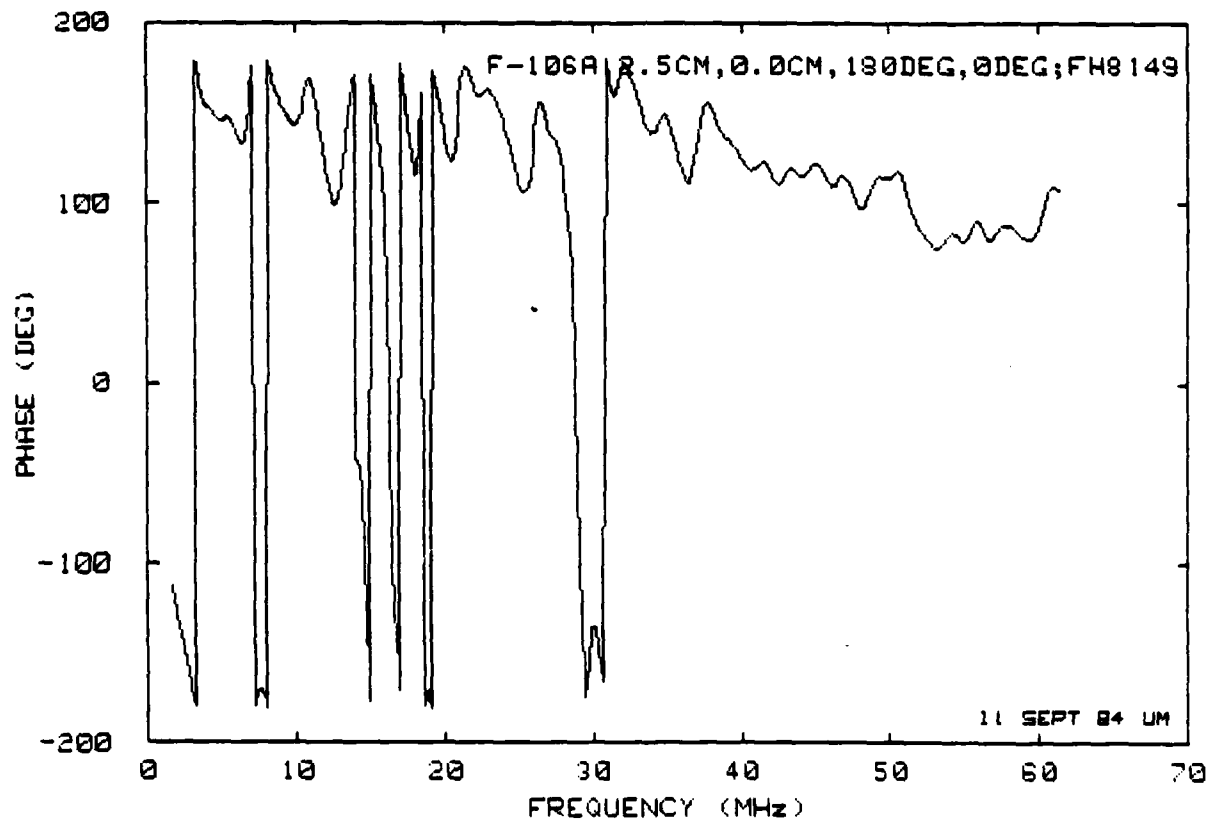
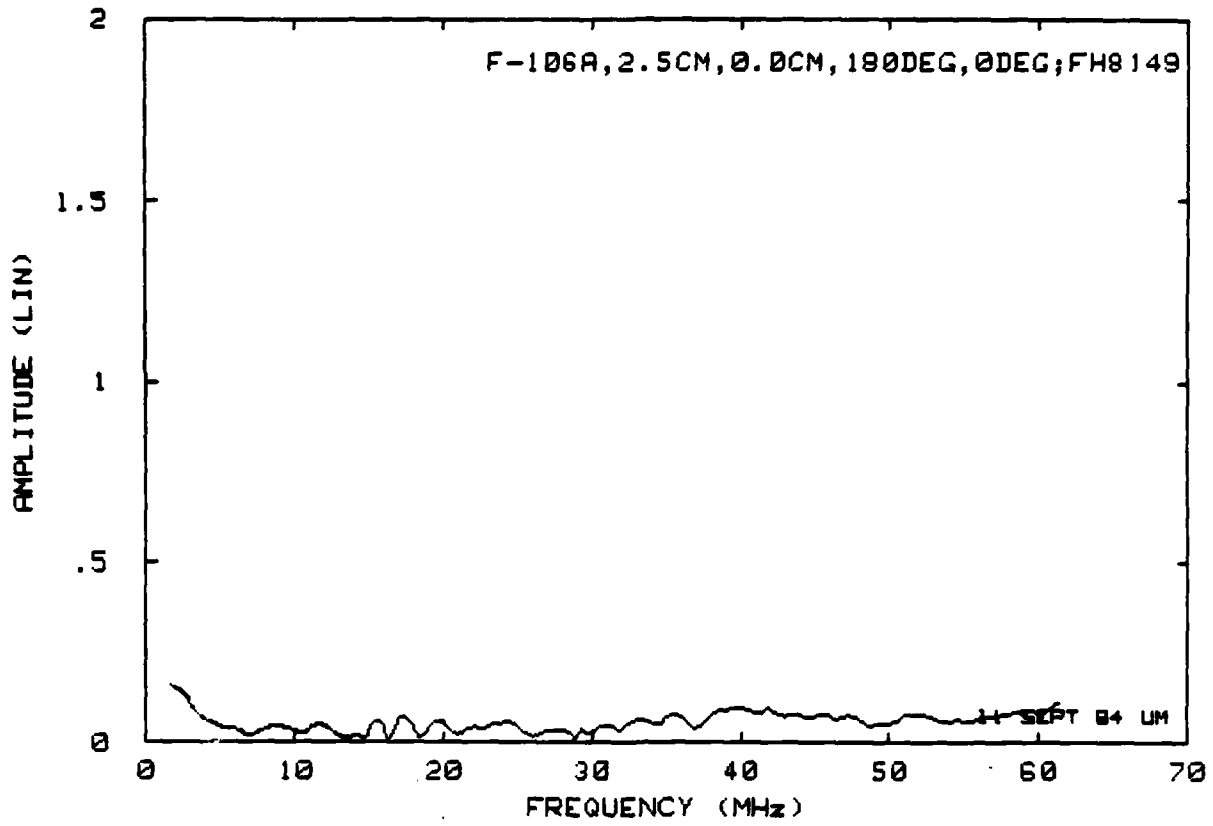
* actually $\theta = 5$ deg (see text)



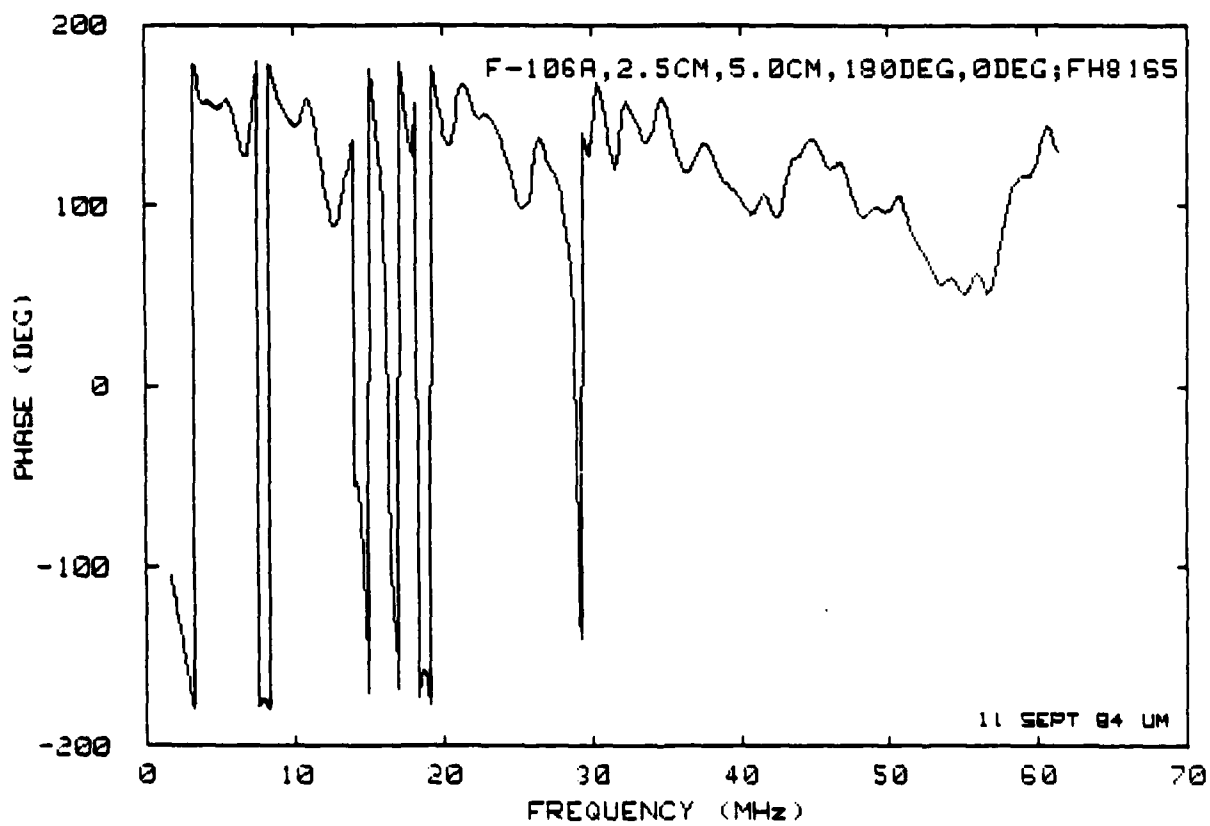
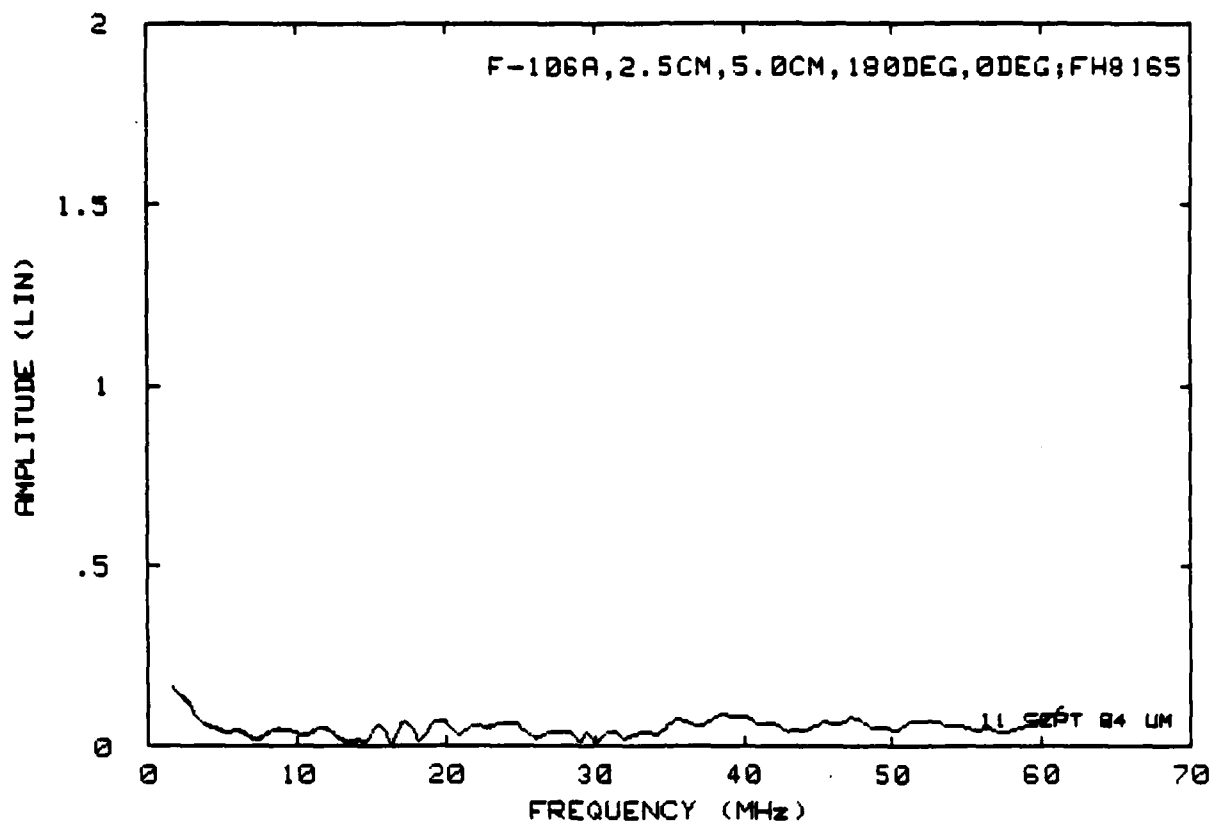
		Position		File		E_1	E_2
1 (1) FH8117	2.50	2 (1) FH8125	1.28	3 (2) FH8133	1.44		
	2.87		1.40		1.73		
4 (2) FH8149	1.57	5 (2) FH8157	1.03	6 (2) FH8165	1.00		
	1.74		1.23		1.19		
7 (3) FH8201	1.51	8 (3) FH8209	1.00	9 (3) FH8217	1.09		
	1.86		1.15		1.39		

Reference files: (1) FH 8109
 (2) FH 8141
 (3) FH 8225

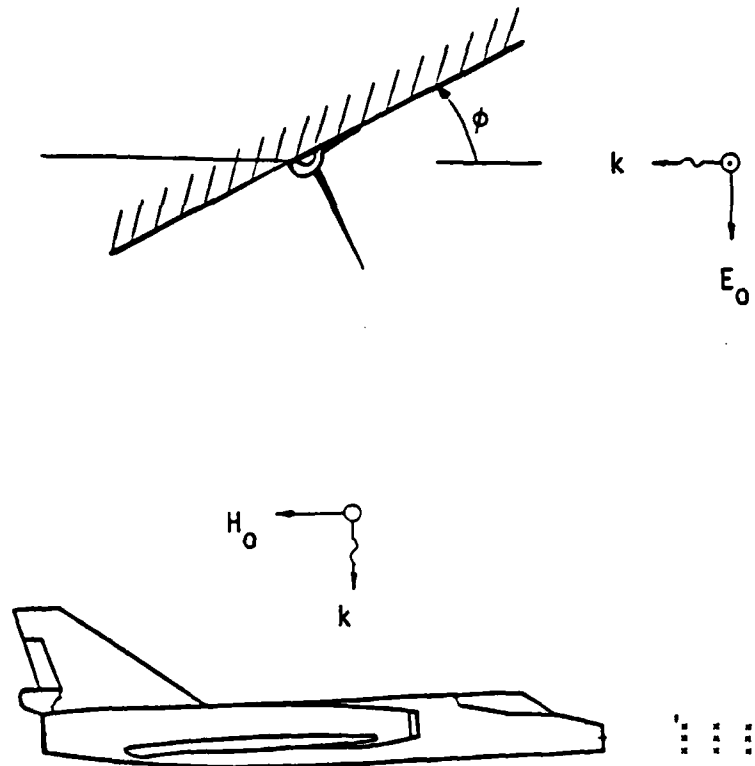
Set 3.1(a): E_1 and E_2 for nose-on incidence, H-vertical, $\phi = 0$ deg.



Set 3.1(b): Normalized field at position 4.



Set 3.1(c): Normalized field at position 6.

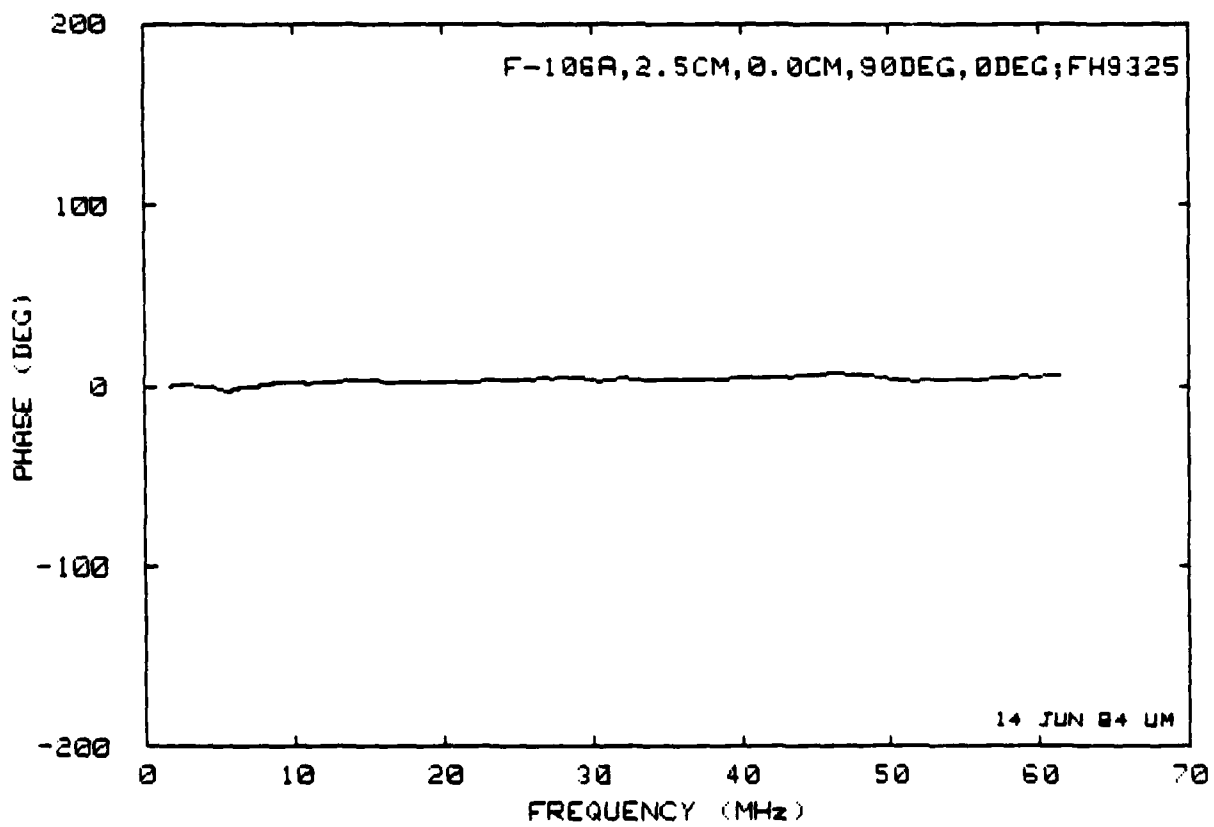
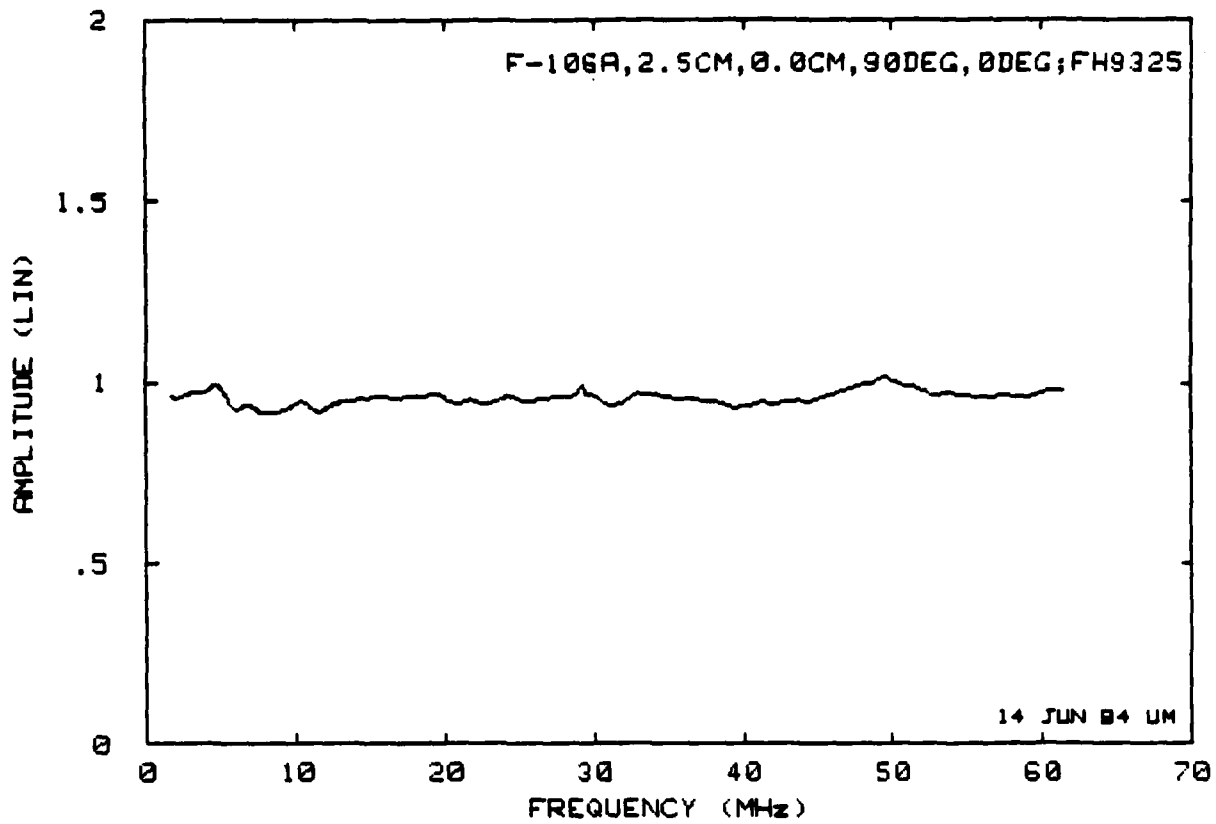


		Position	File		E_1
1	4.62	2	2.81	3	2.10
FH9301	5.37	FH9319	3.05	FH9317	2.41
4	4.90	5	2.88	6	1.61
FH9325	5.15	FH9333	3.09	FH9349	1.89
7	5.23	8	3.23	9	1.61
FH9357	5.53	FH9365	3.49	FH9373	1.83

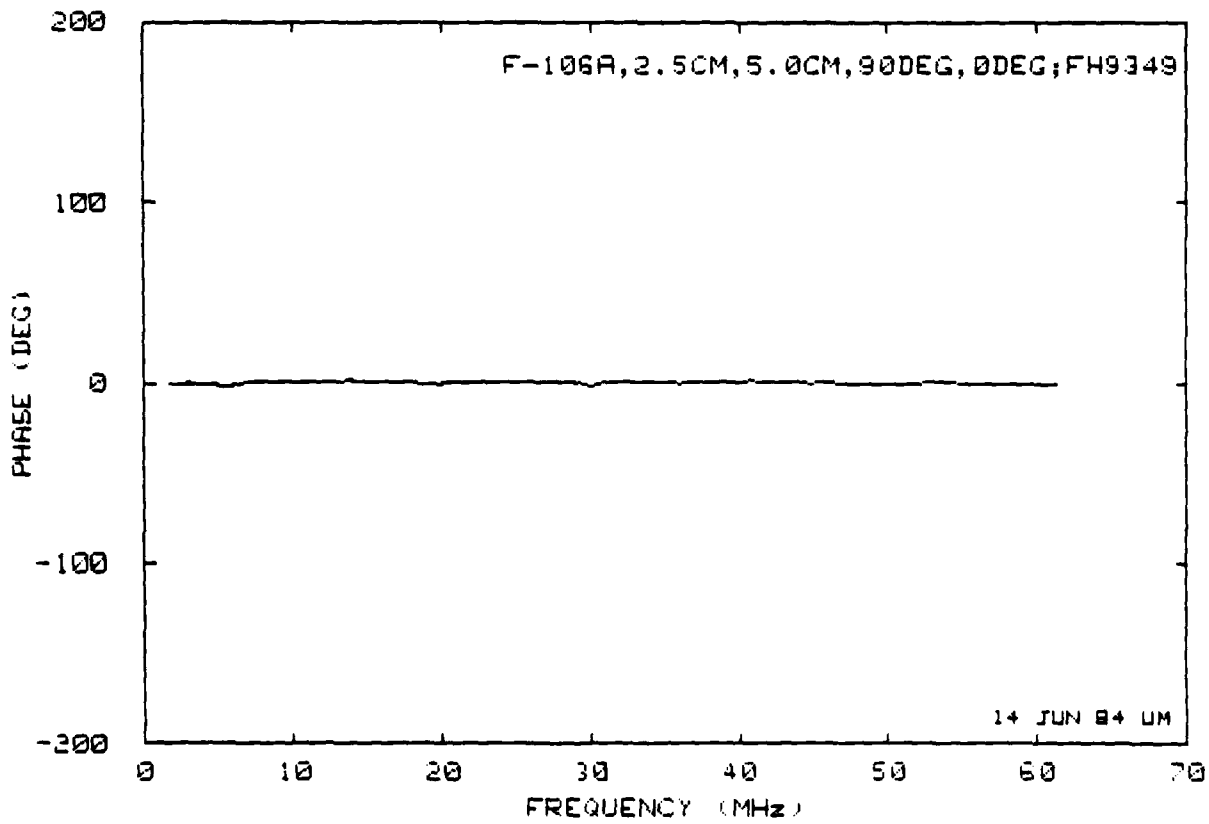
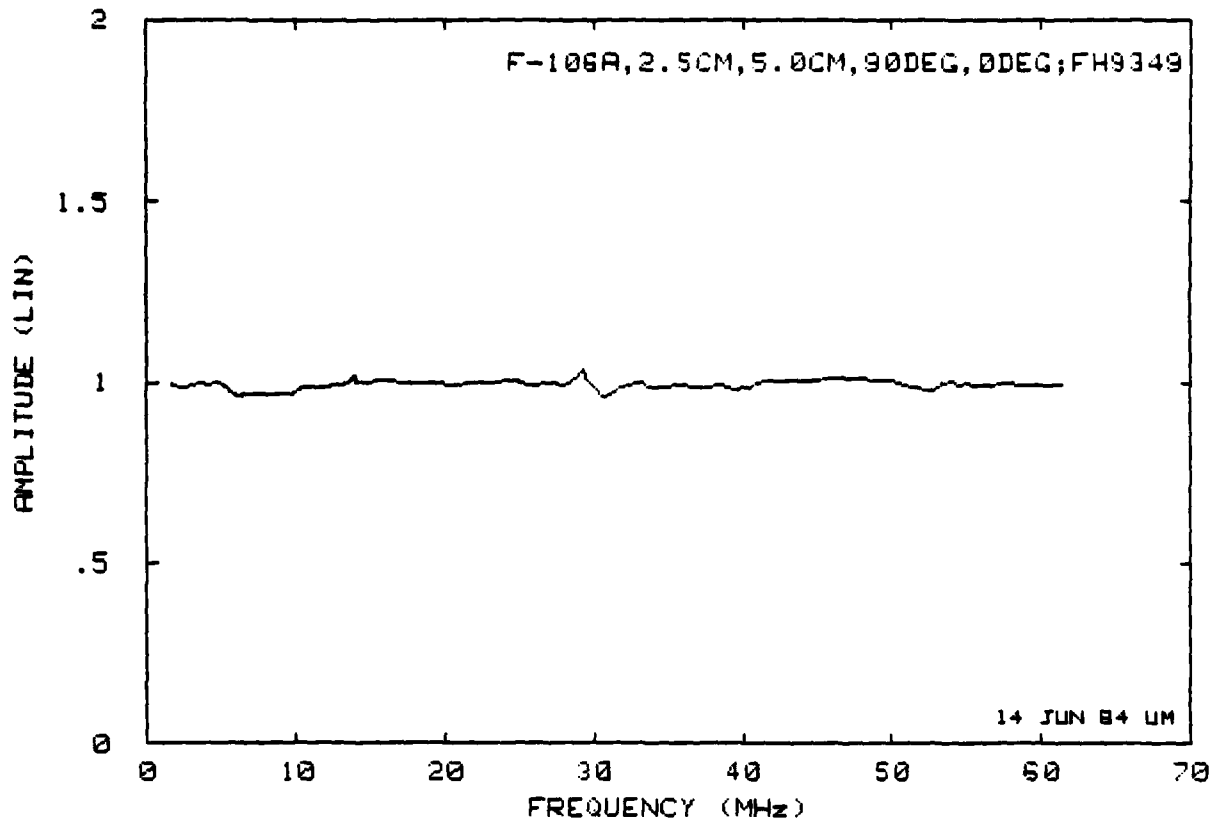
Reference File:

U-F106 (Unity)

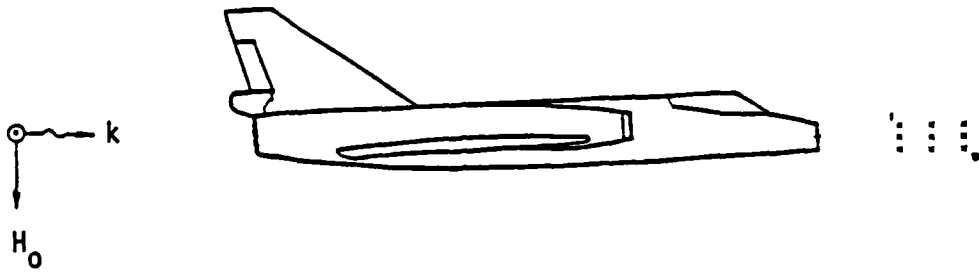
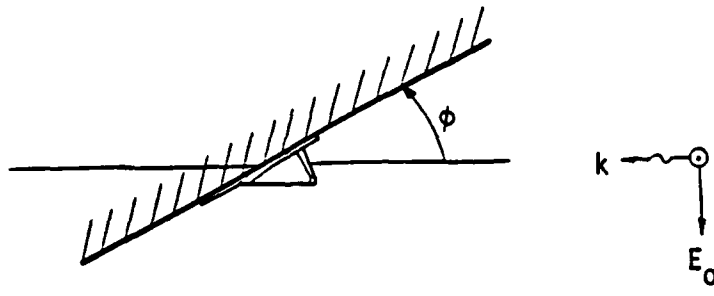
Set 3.2(a): E_1 and E_2 for top incidence, H-parallel on fuselage, $\delta = 0$ deg.



Set 3.2(b): Normalized field at position 4.



Set 3.2(c): Normalized field at position 6.

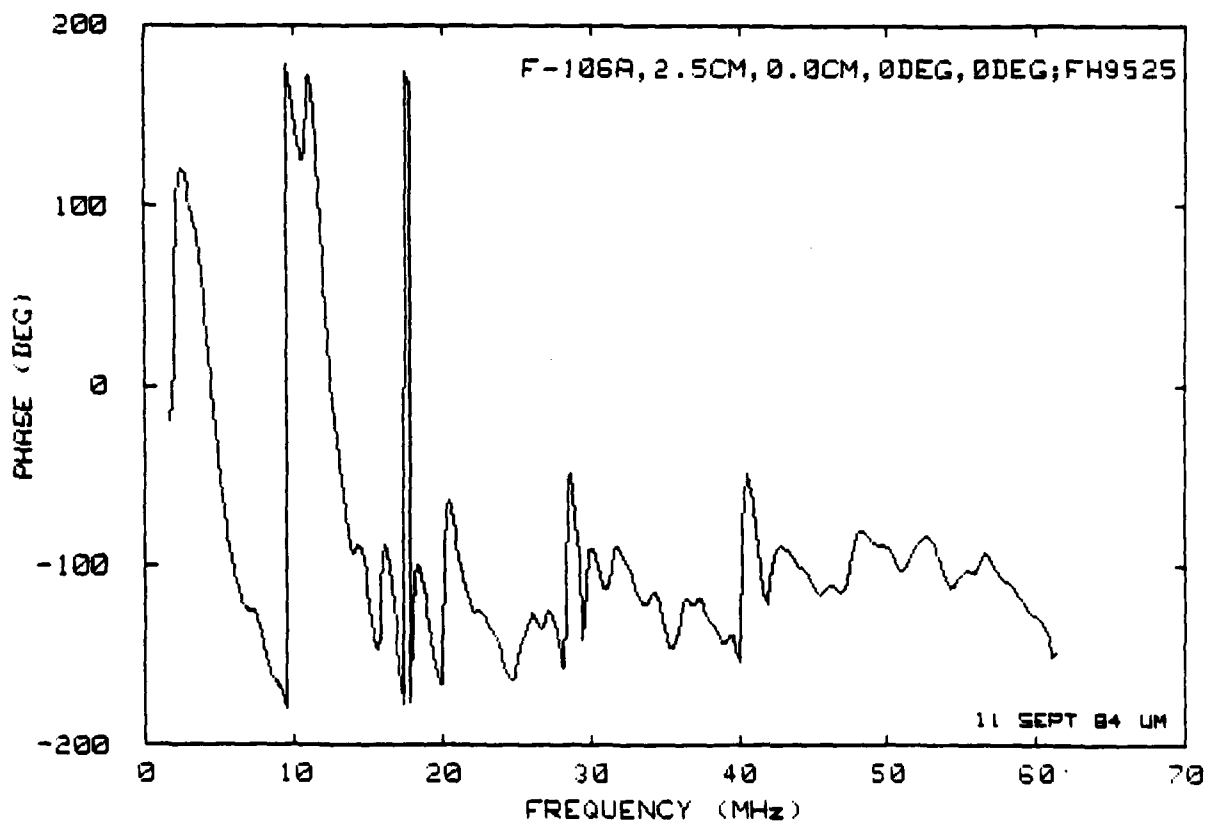
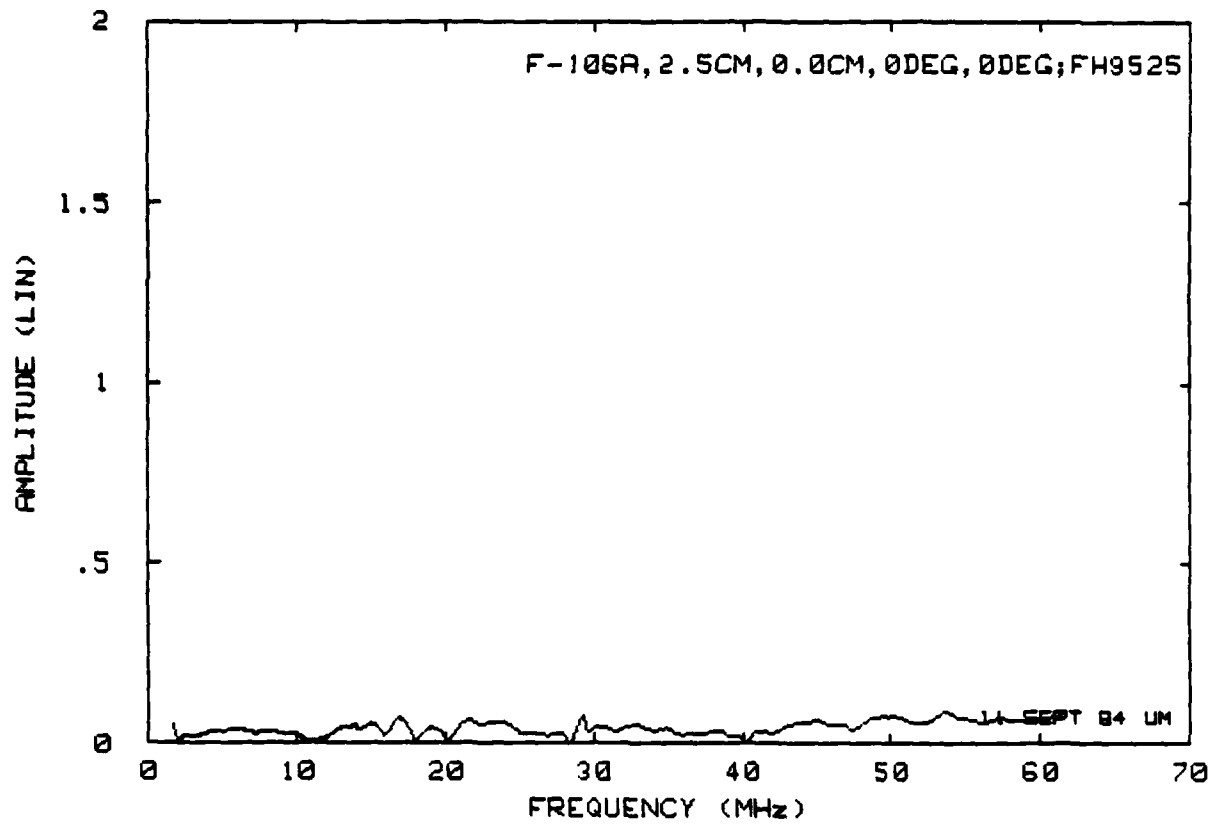


		Position	File	E_1	E_2
1	1.63	2	0.94	3	1.03
FH9501	1.95	FH9509	1.11	FH9517	1.42
4	1.55	5	0.96	6	1.00
FH9525	1.94	FH9541	1.22	FH9549	1.34
7	1.85	8	1.22	9	1.25
FH9557	2.09	FH9565	1.55	FH9573	1.59

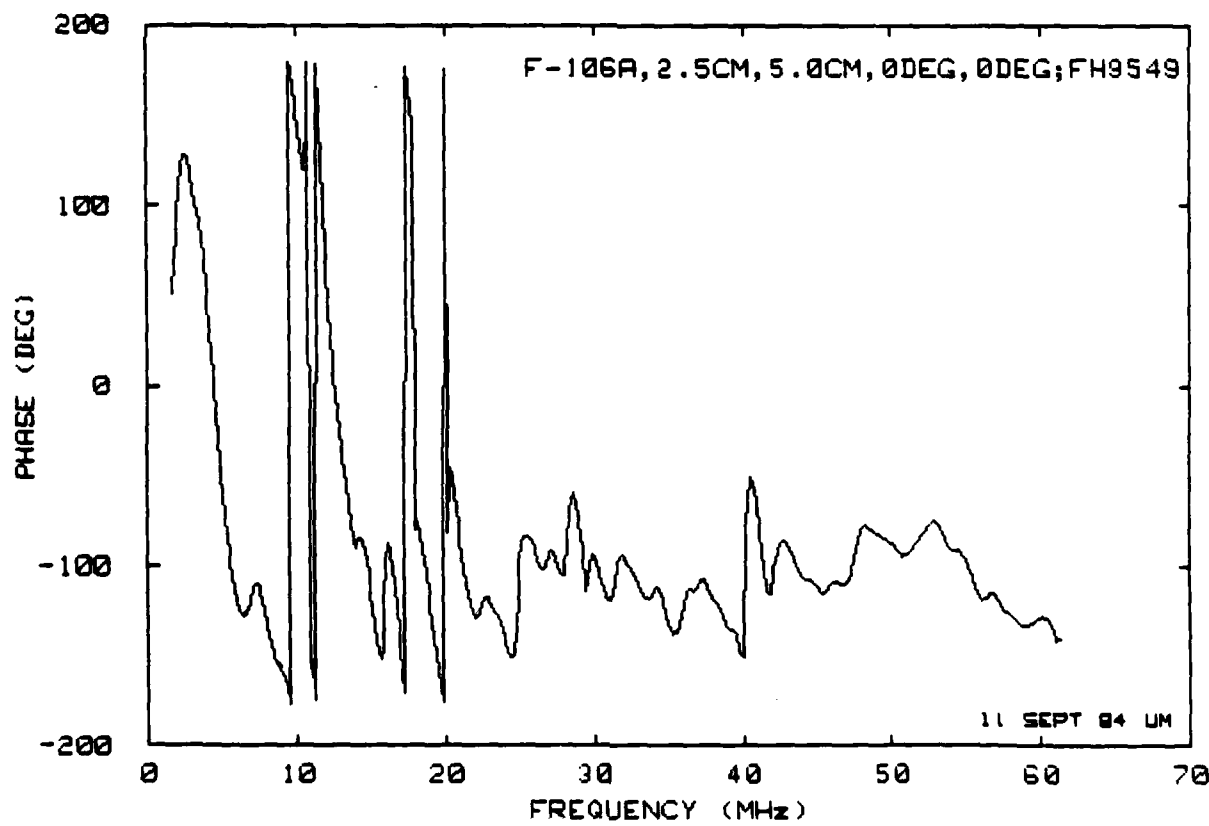
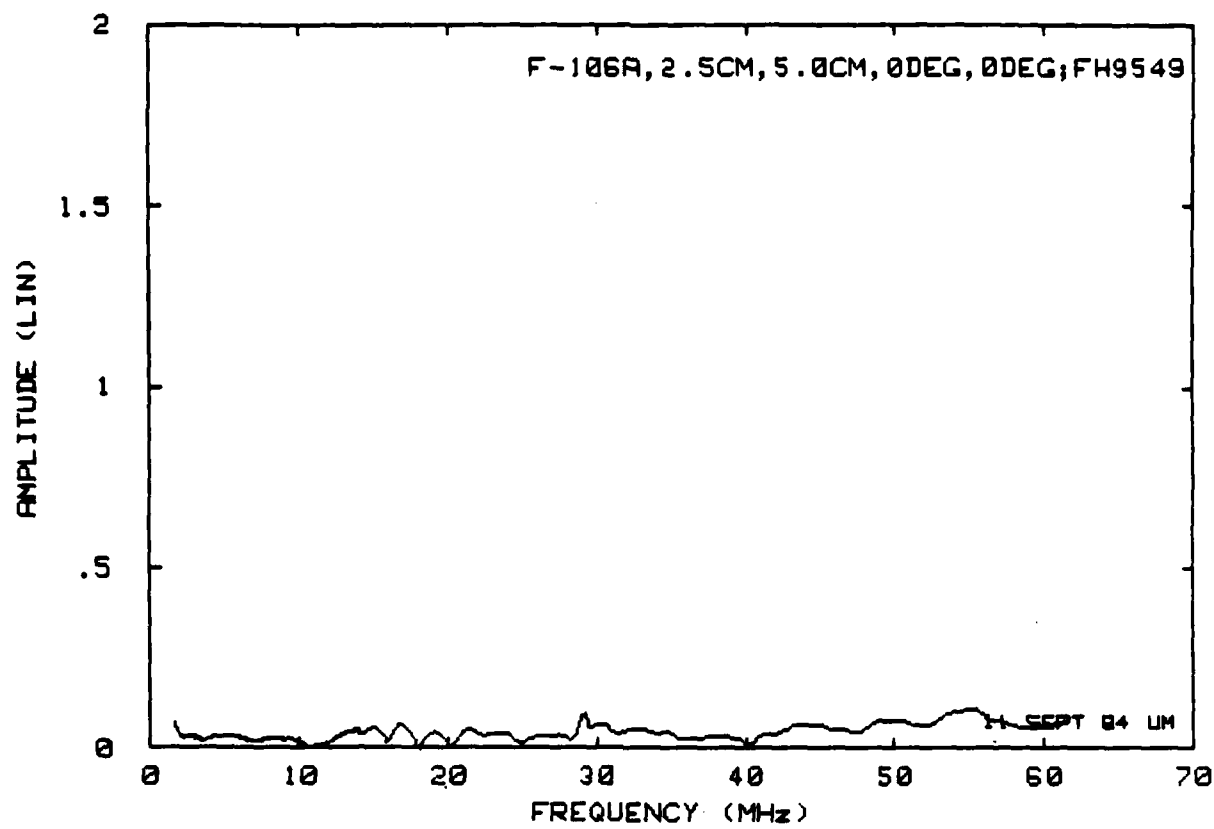
Reference File:

FH9533

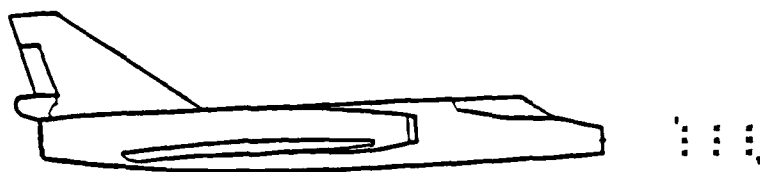
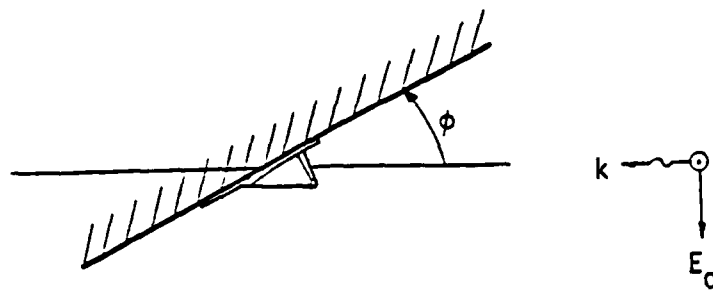
Set 3.3(a): E_1 and E_2 for tail-on incidence, H-vertical, $\phi = 0$ deg.



Set 3.3(b): Normalized field at position 4.



Set. 3.3(c): Normalized field at position 6.

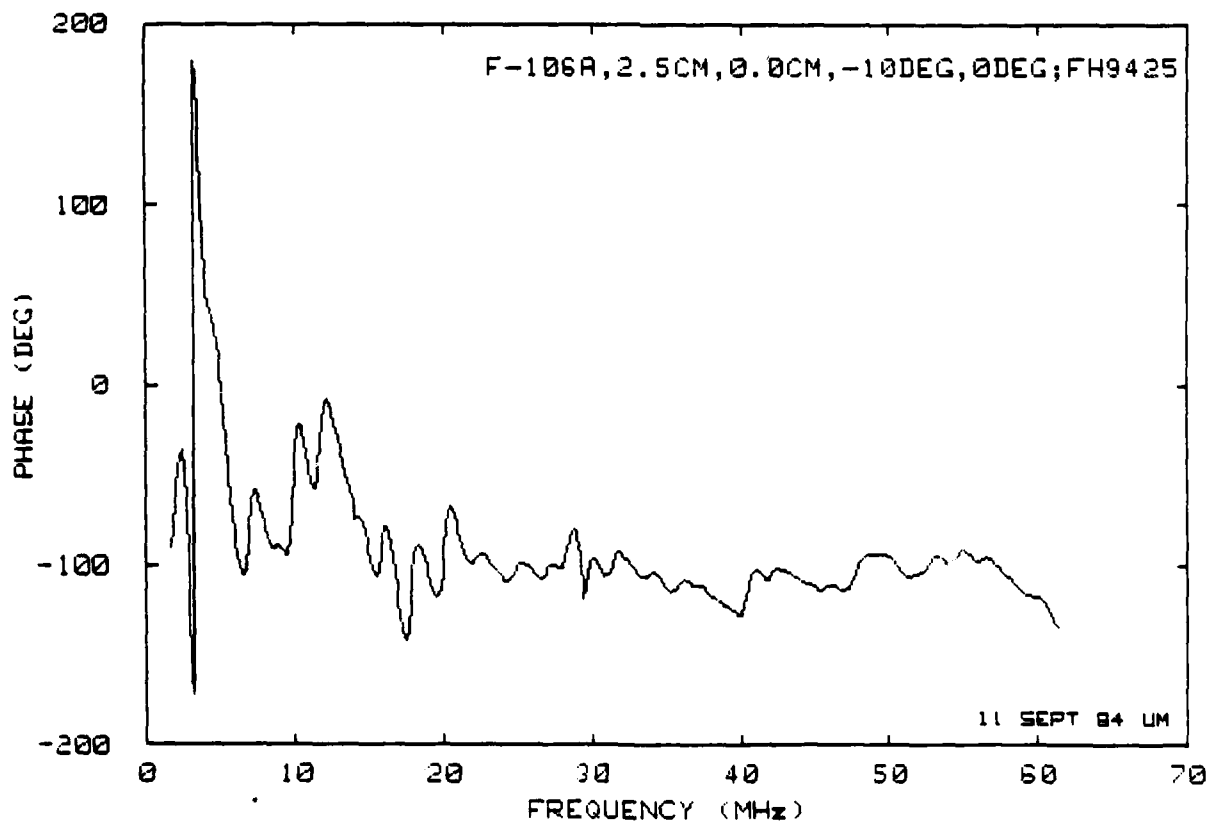
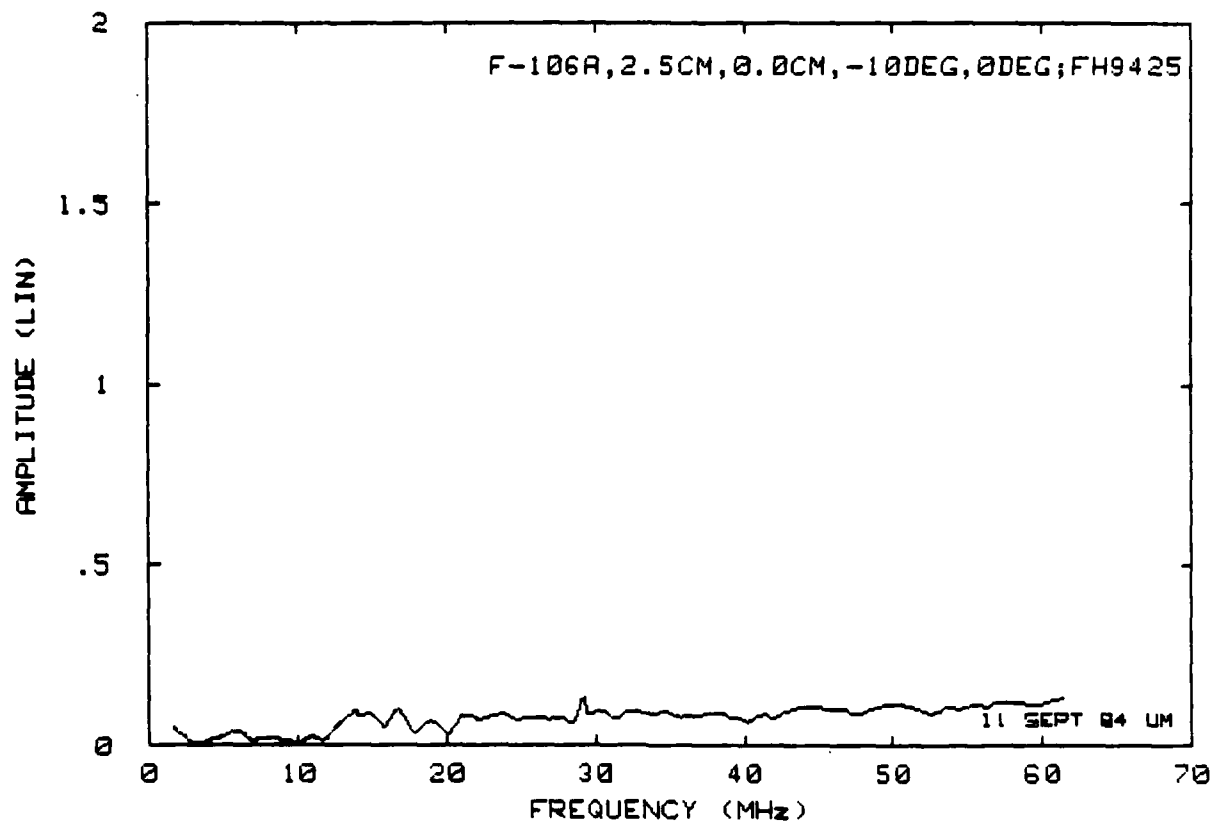


		Position		File		E_1
1	4.63	2	4.34	3	3.82	E_2
FH9401	4.78	FH9409	4.78	FH9417	3.99	
4	4.06	5	4.02	6	3.79	
FH9425	4.28	FH9433	4.22	FH9449	3.91	
7	3.97	8	3.61	9	3.58	
FH9457	4.22	FH9465	3.83	FH9472	3.64	

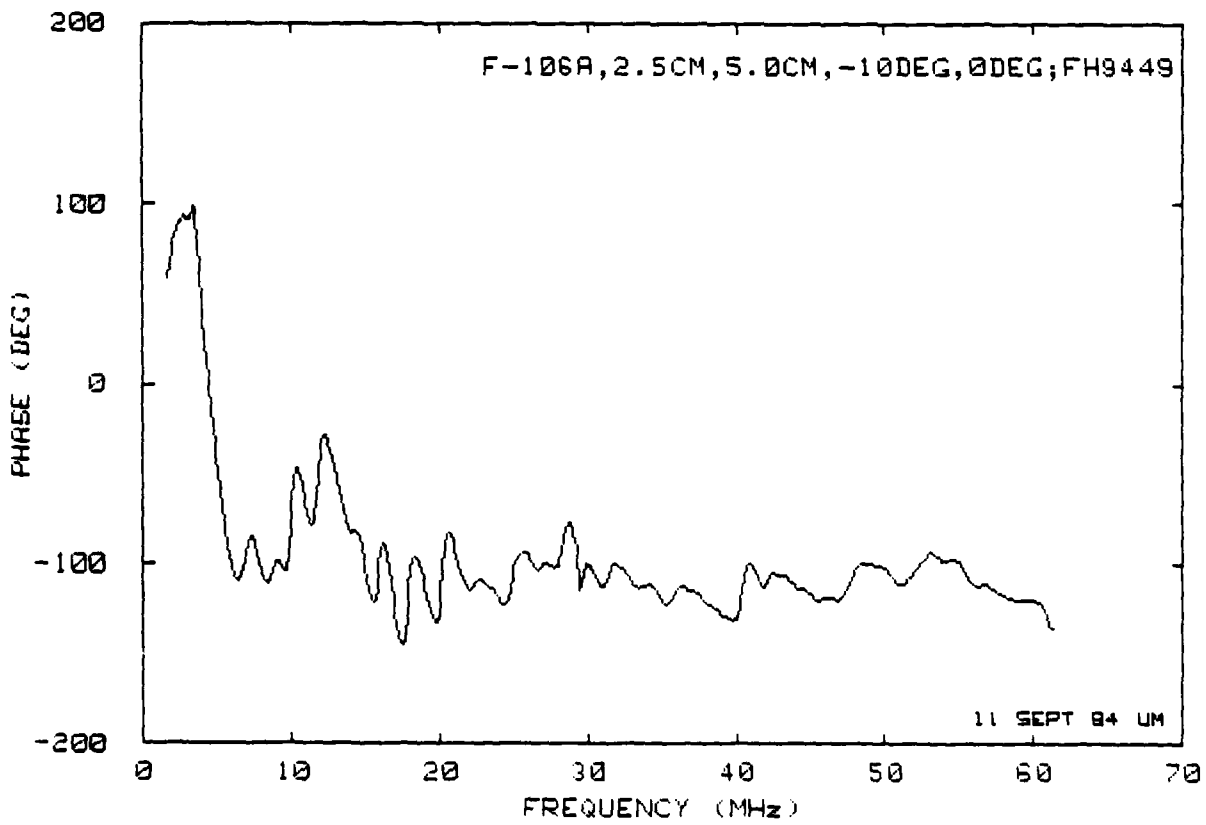
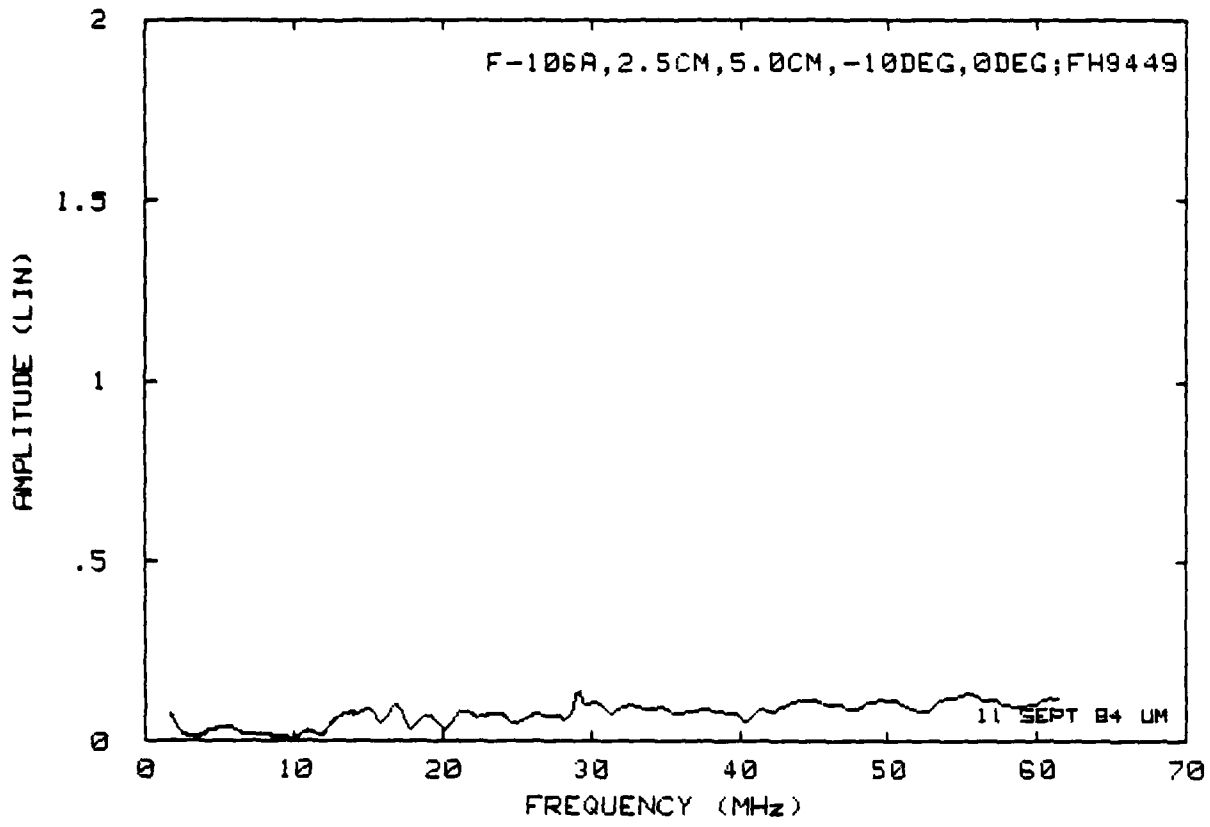
Reference file:

FH9441

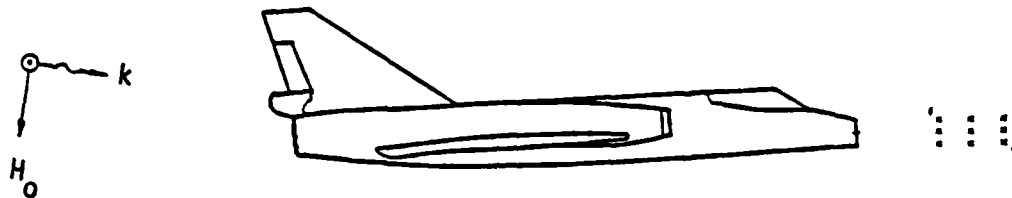
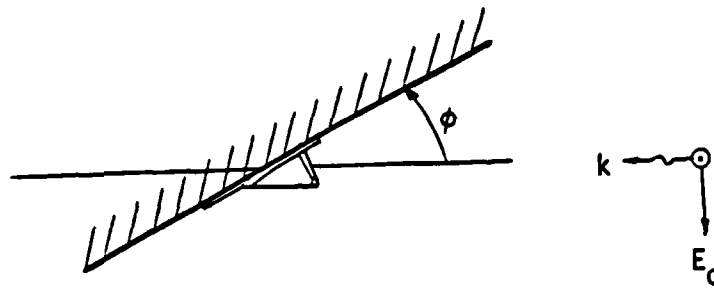
Set 3.4(a): E_1 and E_2 for tail-on incidence (-10 degrees), H-vertical,
 $\phi = 0$ deg.



Set 3.4(b): Normalized field at position 4.



Set 3.4(c): Normalized field at position 6.

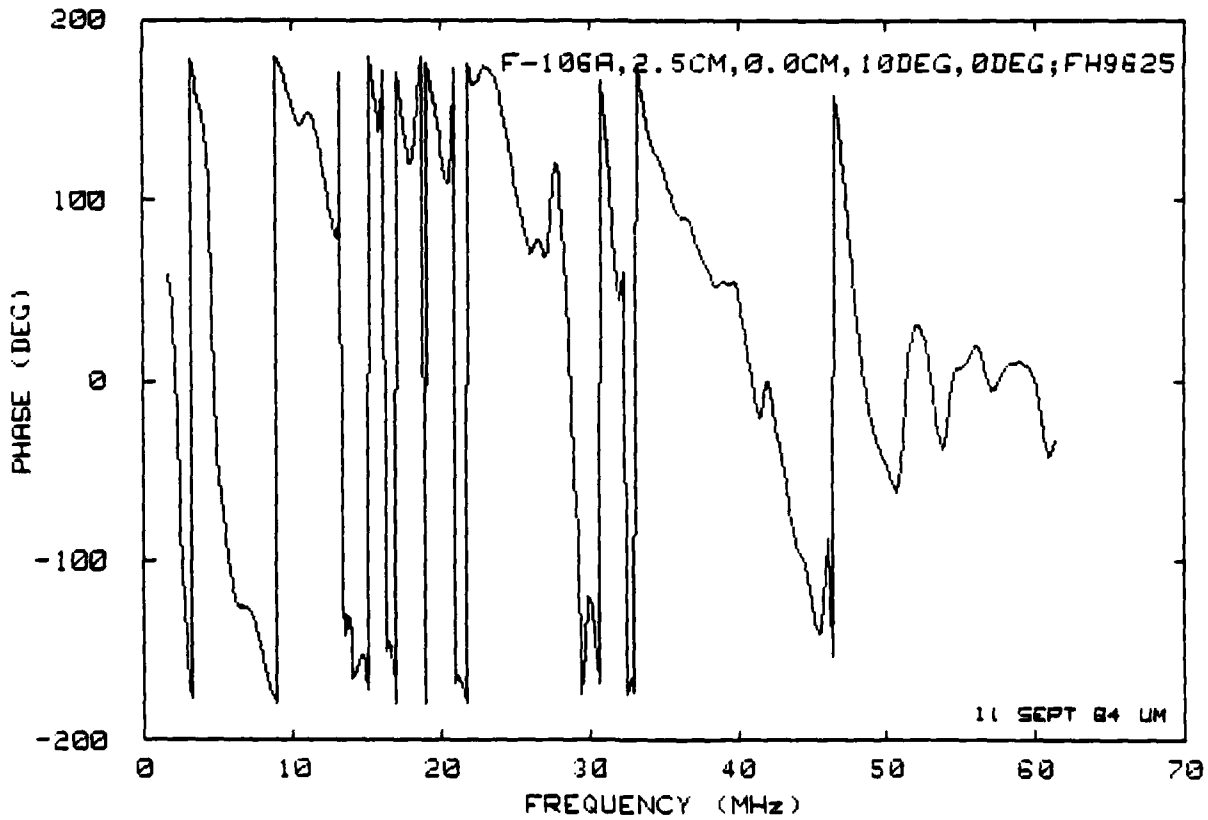
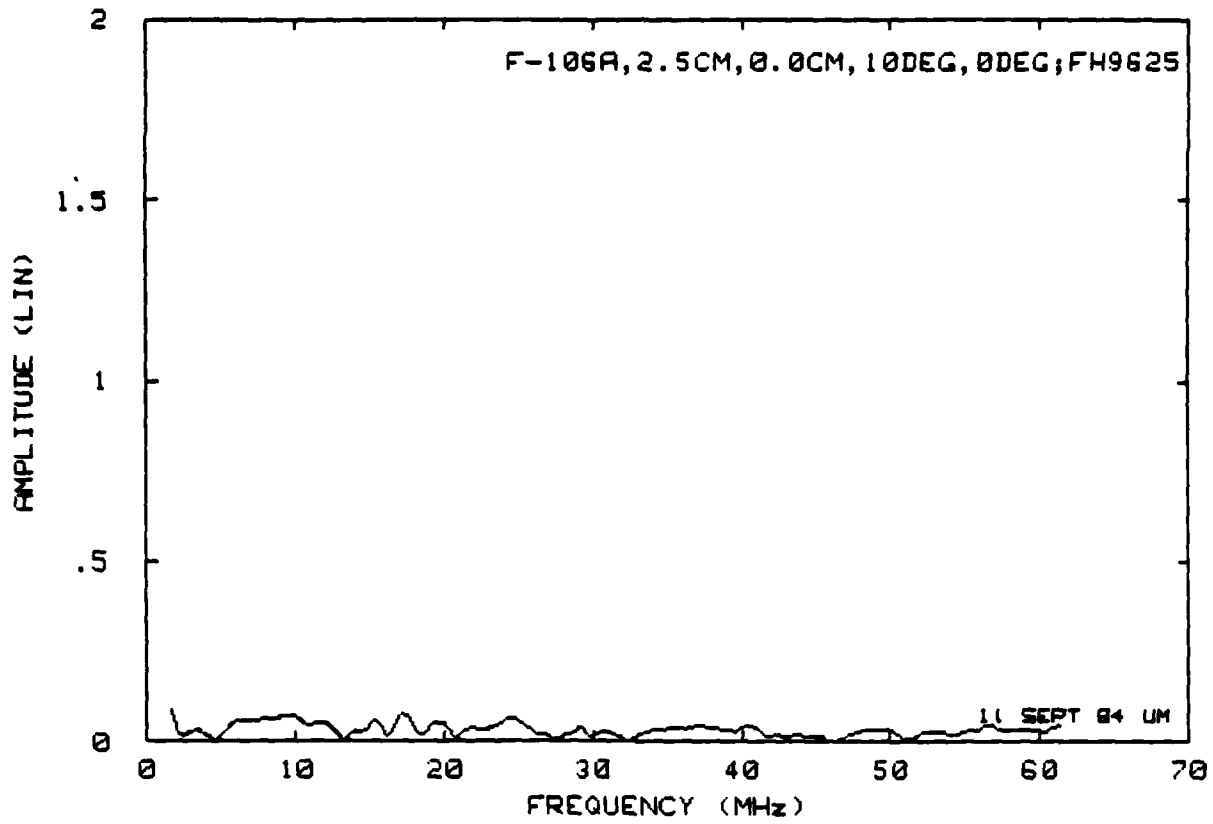


		Position		File	
1	4.01	2	3.51	3	E_1 3.67
FH9601	4.34	FH9609	3.85	FH9617	E_2 3.97
4	5.33	5	4.05	6	4.00
FH9625	5.53	FH9633	4.39	FH9649	4.29
7	5.60	8	4.47	9	4.22
FH9657	5.89	FH9665	4.75	FH9673	4.58

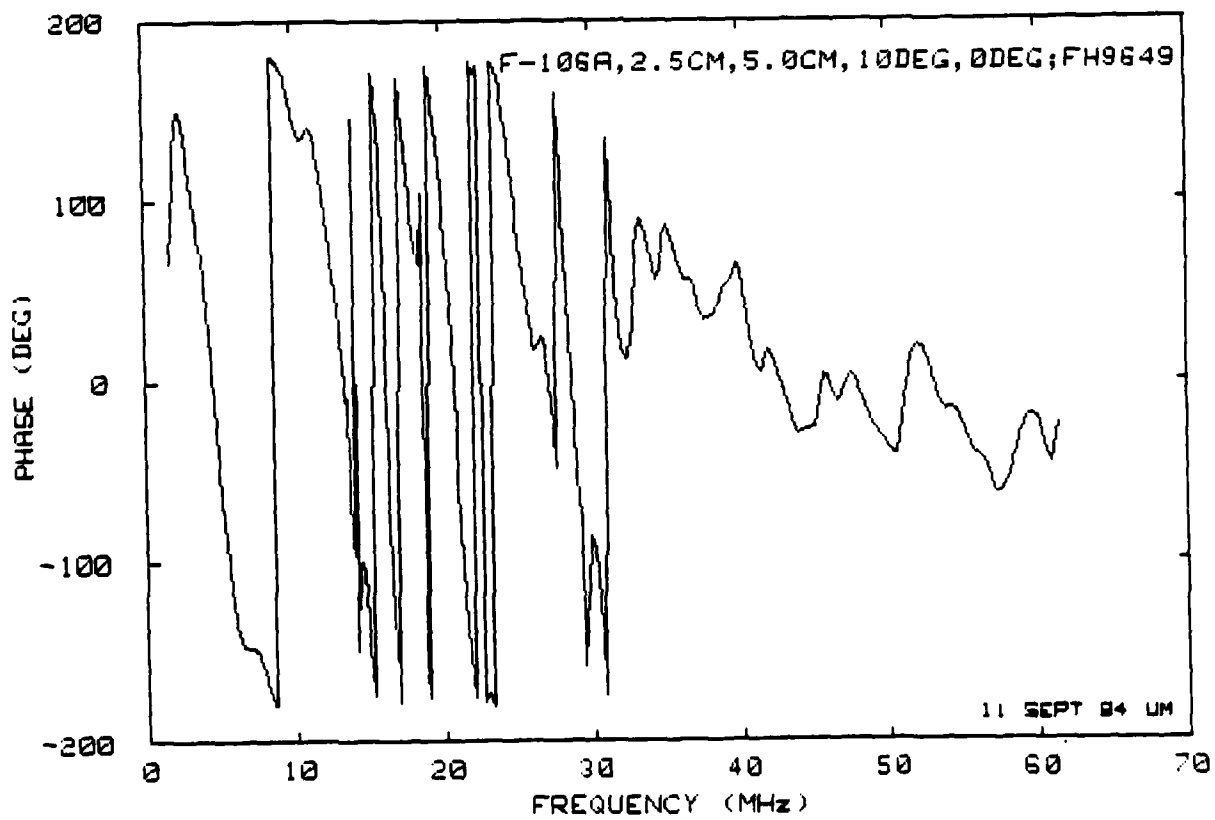
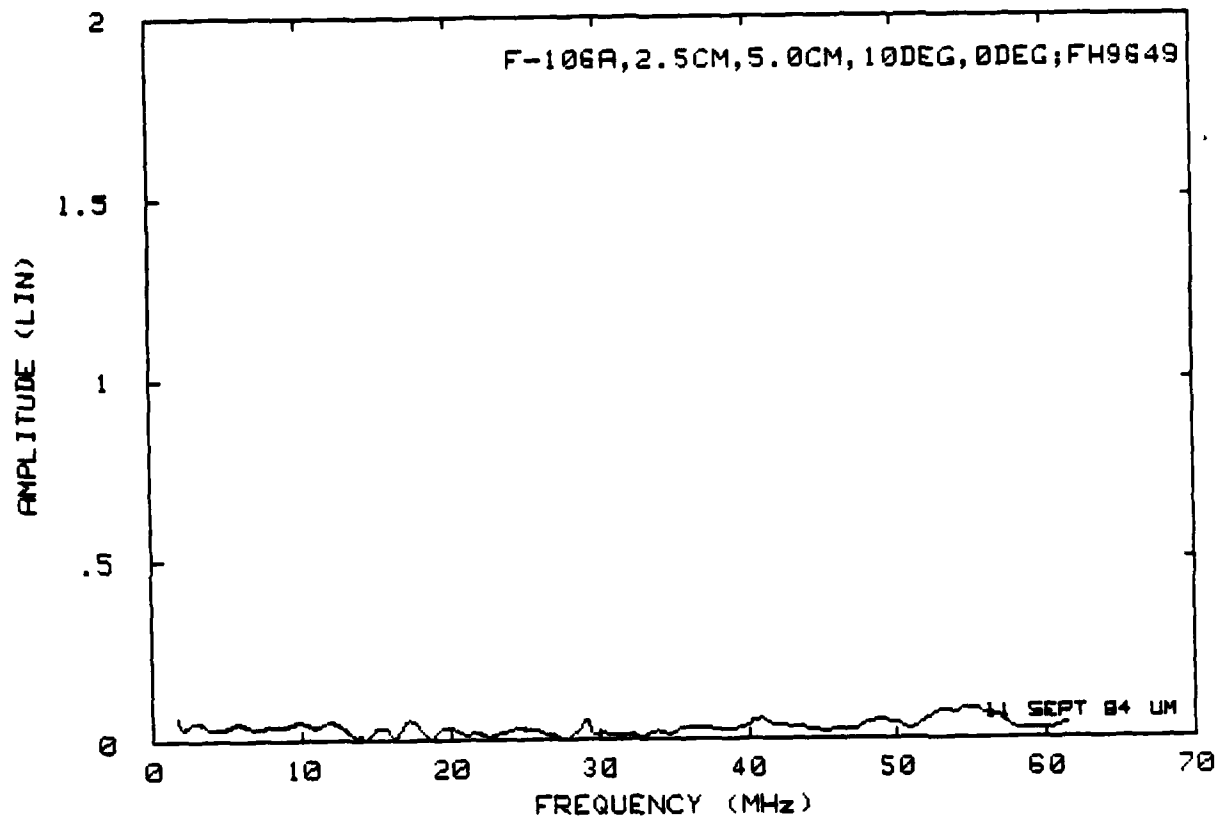
Reference file:

FH9641

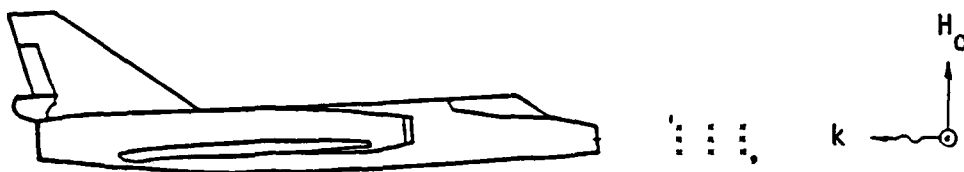
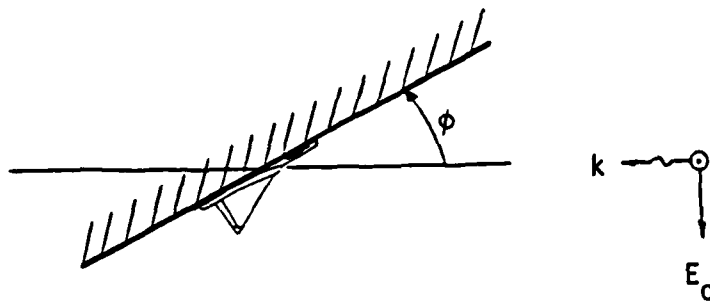
Set 3.5(a): E_1 and E_2 for tail-on incidence (10 degrees), H-vertical,
 $\phi = 0$ deg.



Set 3.5(b): Normalized field at position 4.



Set 3.5(c): Normalized field at position 6.

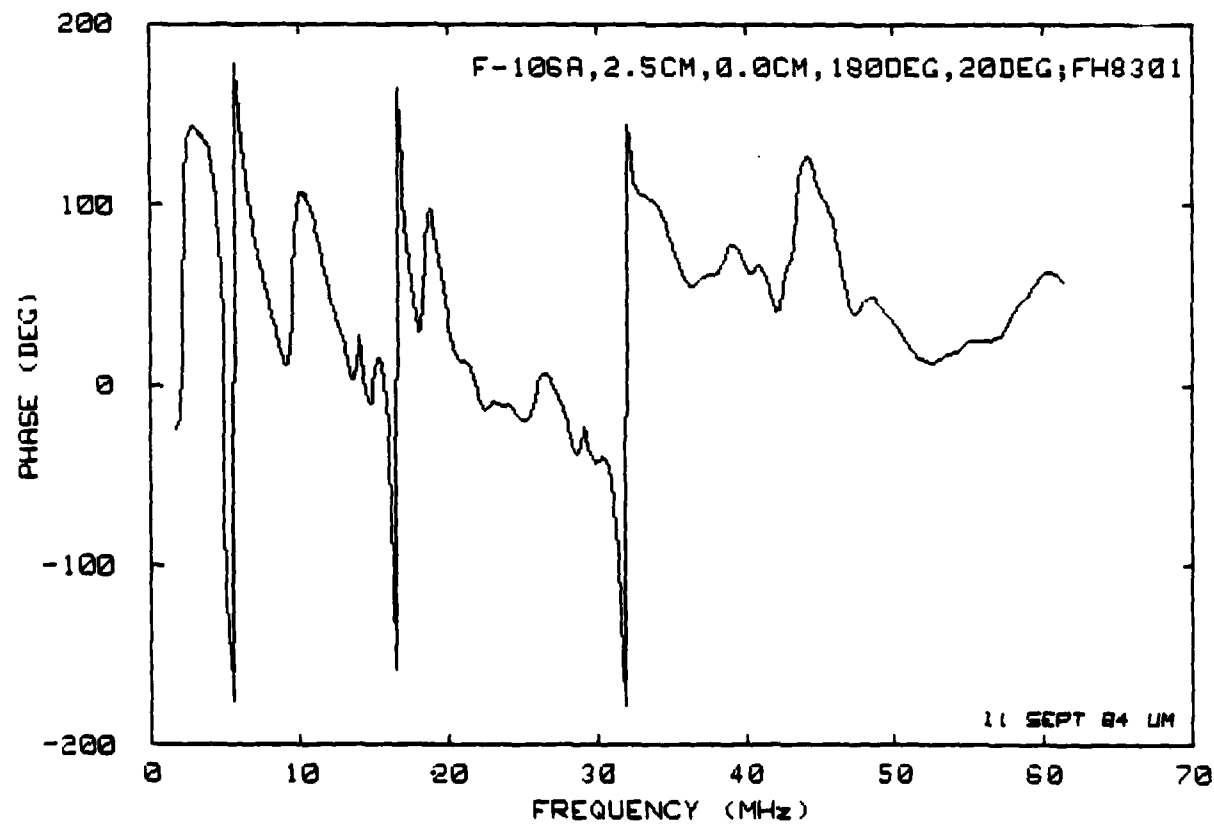
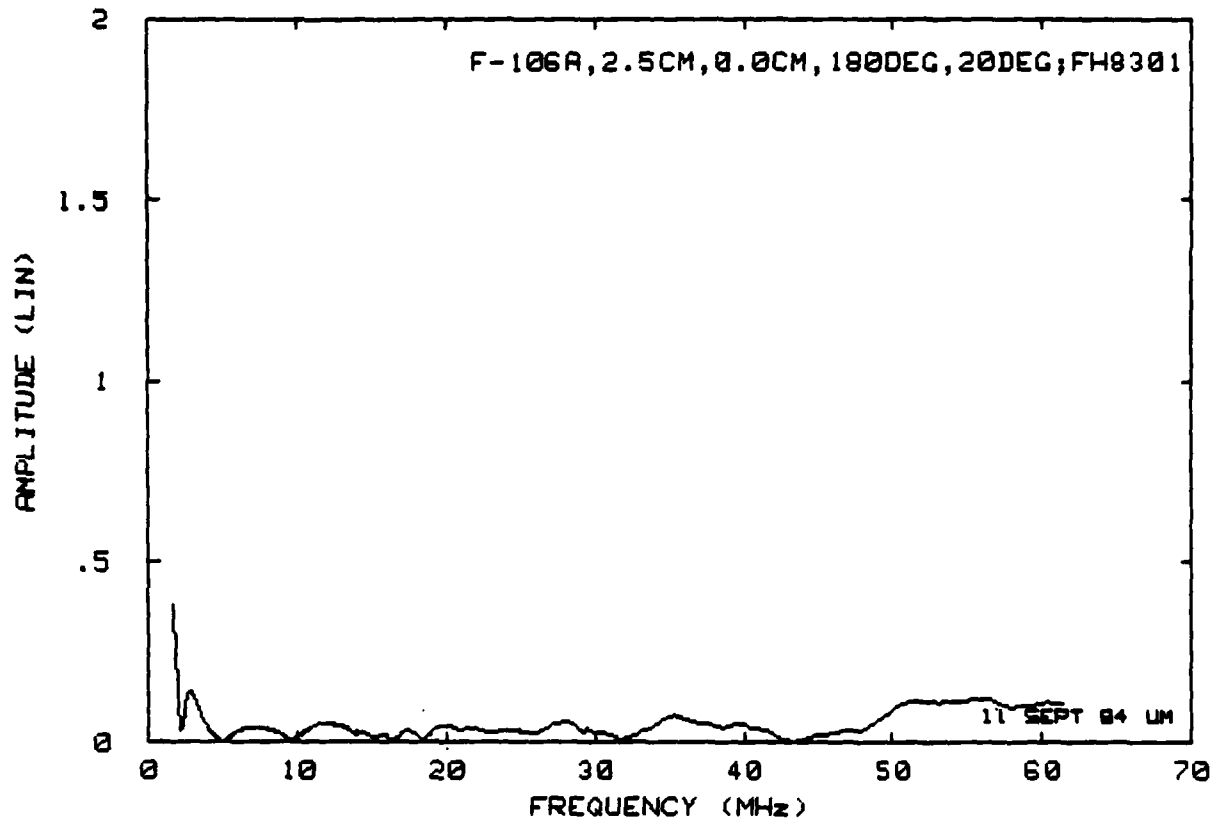


		Position	File		E_1	E_2
1 (1) FH8249	1.67	2 (1) FH8257	1.42	3 (1) FH8273	1.14	
	2.06		1.74		1.34	
4 (2) FH8301	2.42	5 (2) FH8309	1.91	6 (2) FH8317	1.25	
	2.79		3.36		2.96	
7 (2) FH8333	2.25	8 (2) FH8341	1.35	9 (2) FH8349	1.11	
	3.46		1.62		1.25	

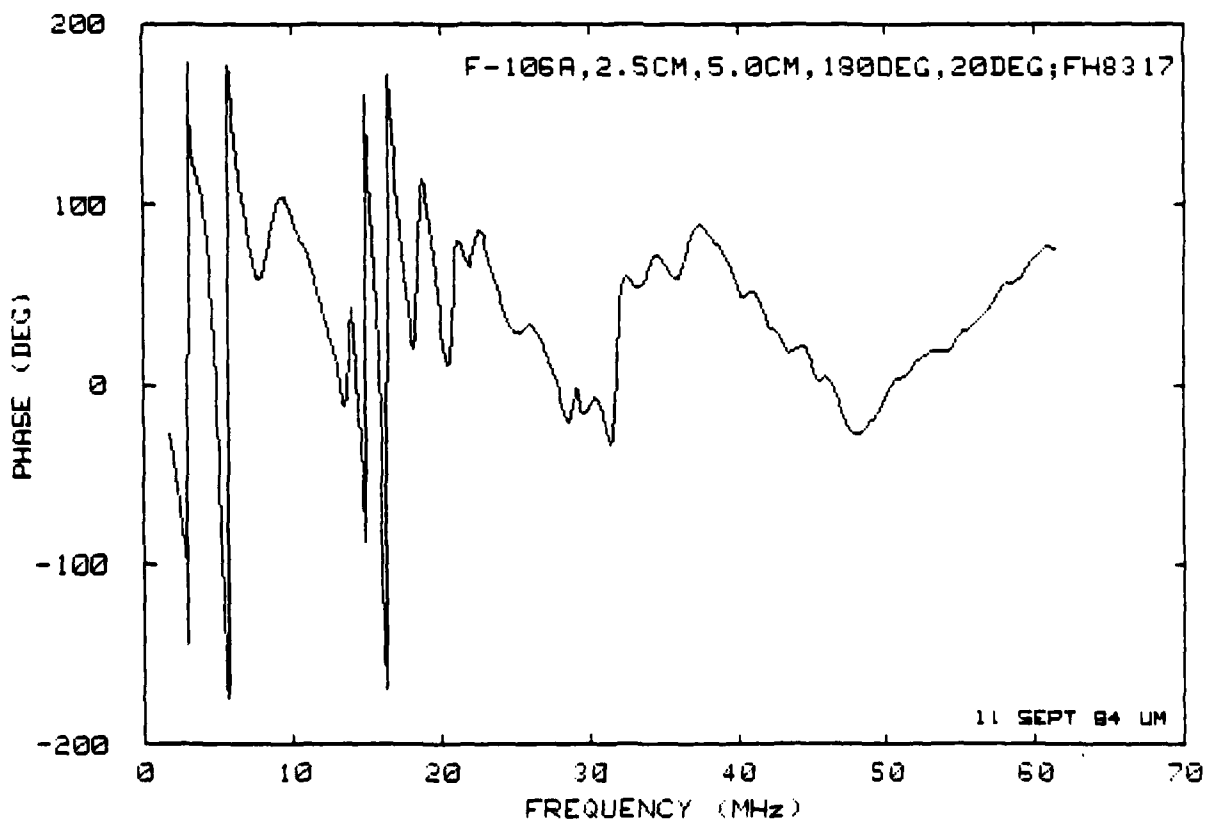
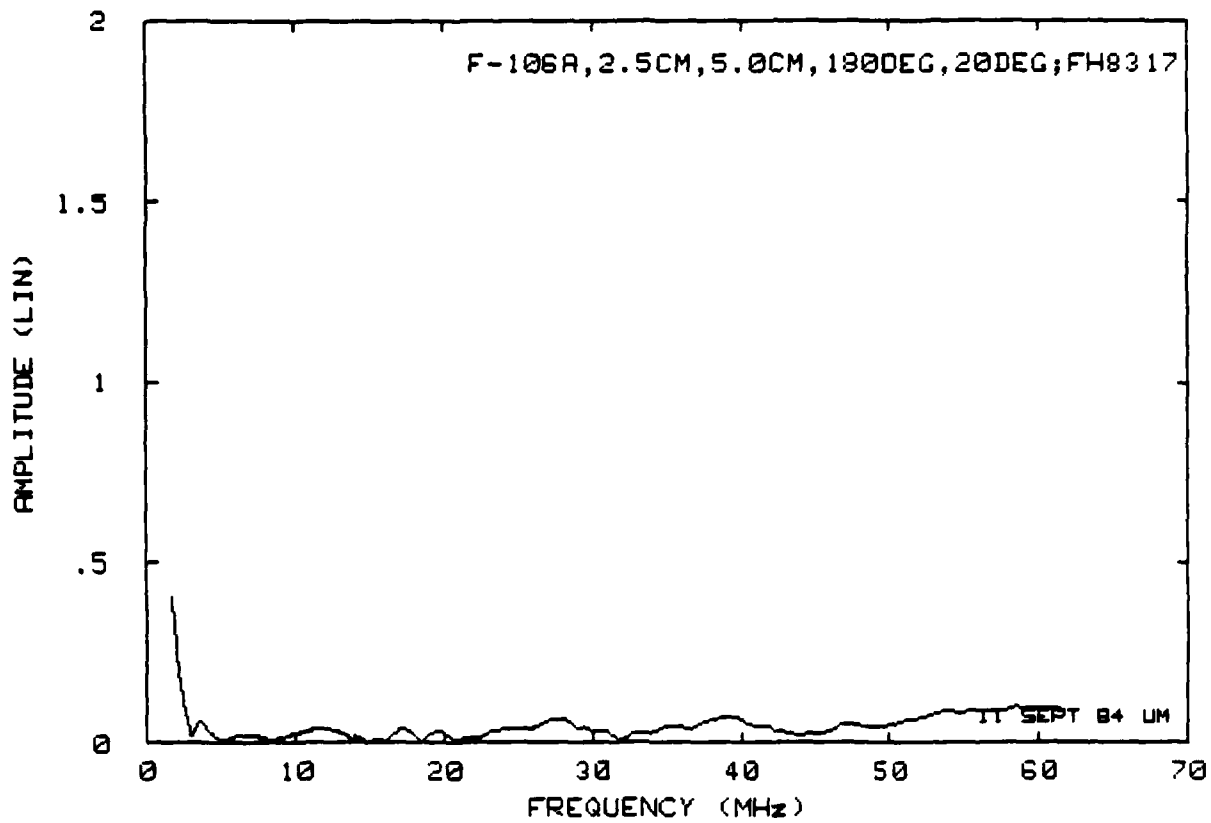
Reference Files:

- (1) FH8265
- (2) FH8325

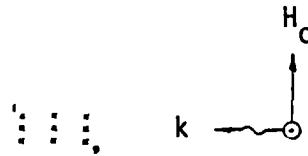
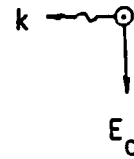
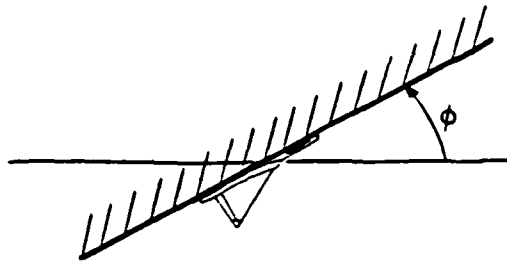
Set 3.6(a): E_1 and E_2 for nose-on incidence, H-vertical, $\phi = 20$ deg.



Set 3.6(b): Normalized field at position 4.



Set 3.6(c): Normalized field at position 6.

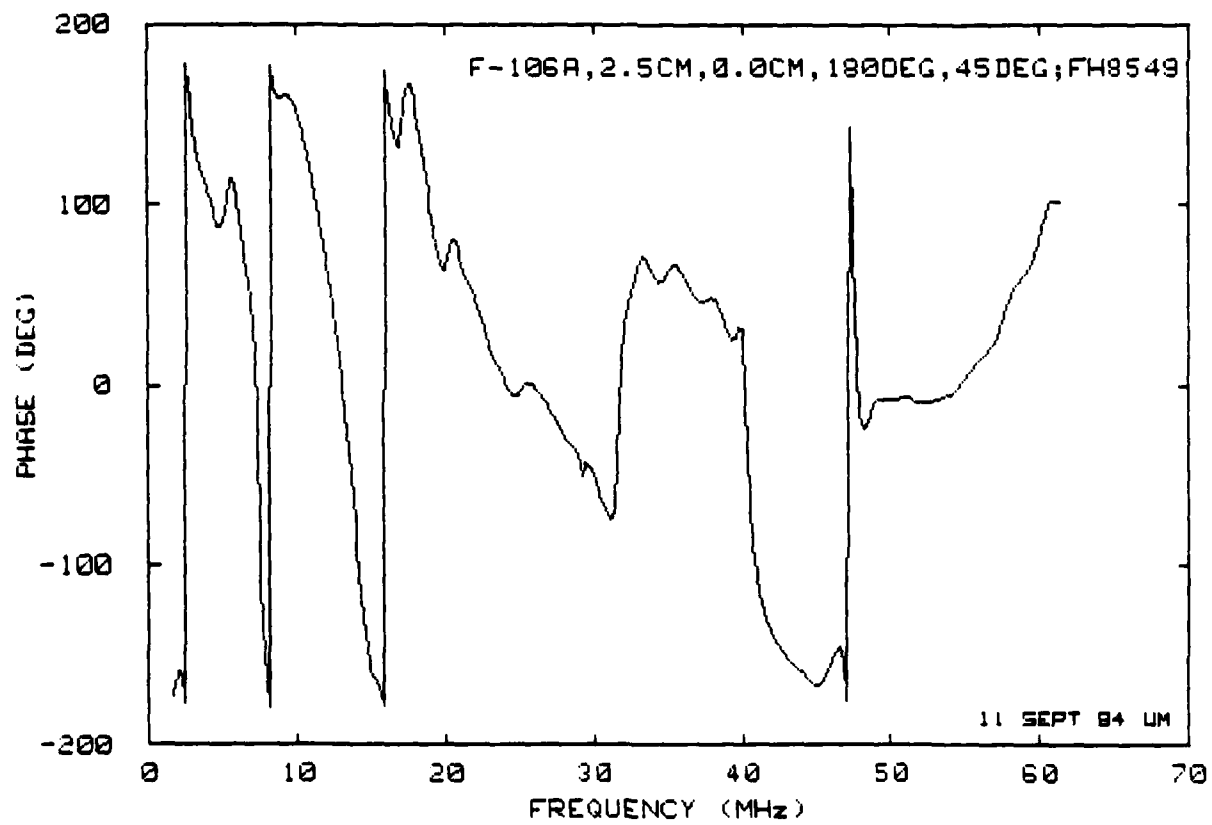
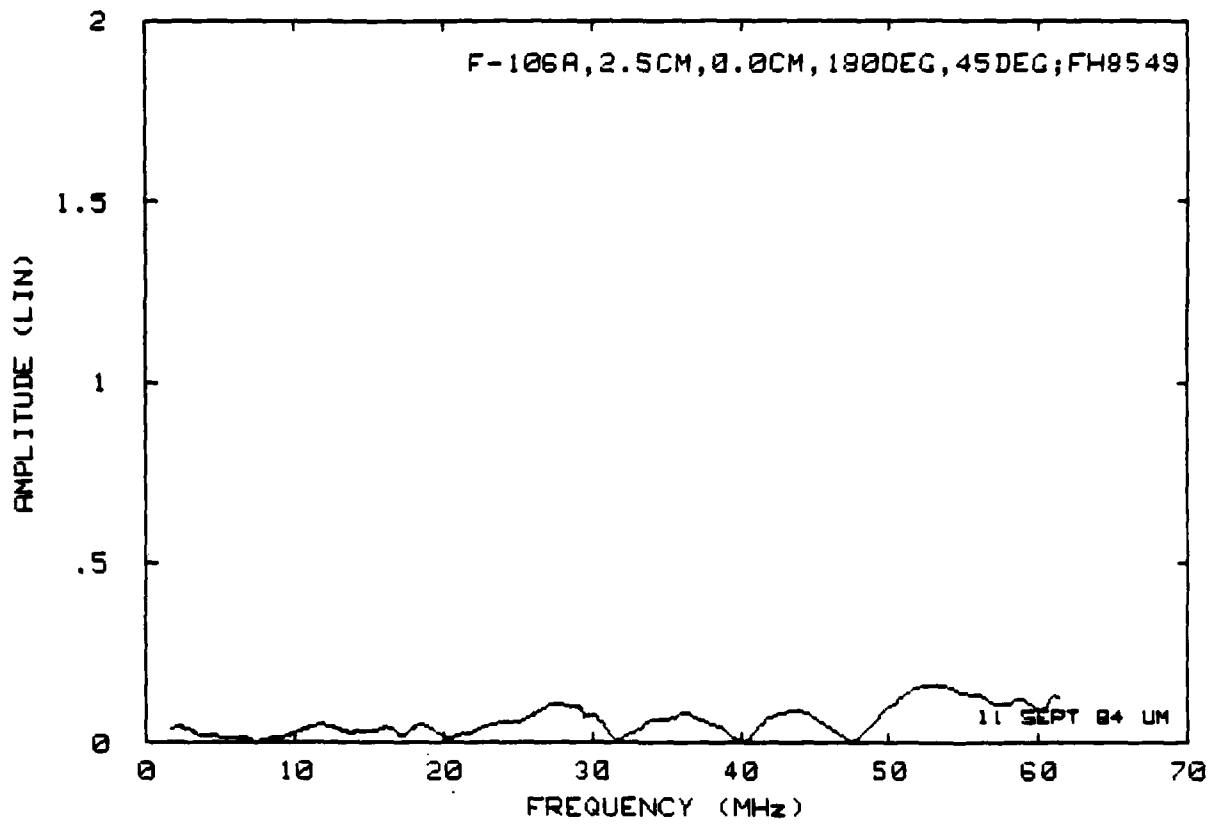


		Position		File		E_1
1 (1)	1.72	2 (1)	0.97	3 (1)	0.87	E_2
FH8509	2.10	FH8517	1.12	FH8541	1.06	
4 (1)	1.55	5 (2)	0.92	6 (2)	0.66	E_2
FH8549	1.72	FH8557	0.99	FH8565	0.77	
7 (2)	2.16	8 (2)	1.38	9 (2)	0.80	E_2
FH8573	2.49	FH8609	1.51	FH8617	0.94	

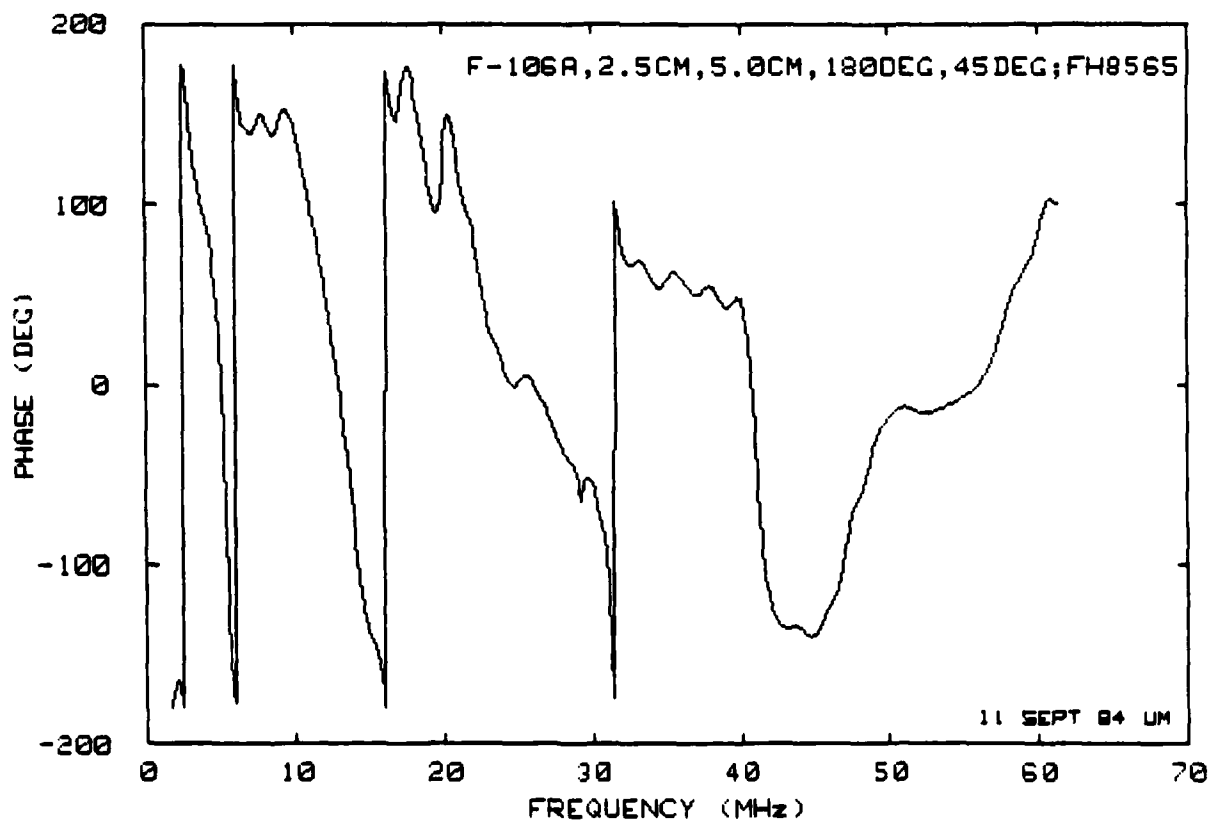
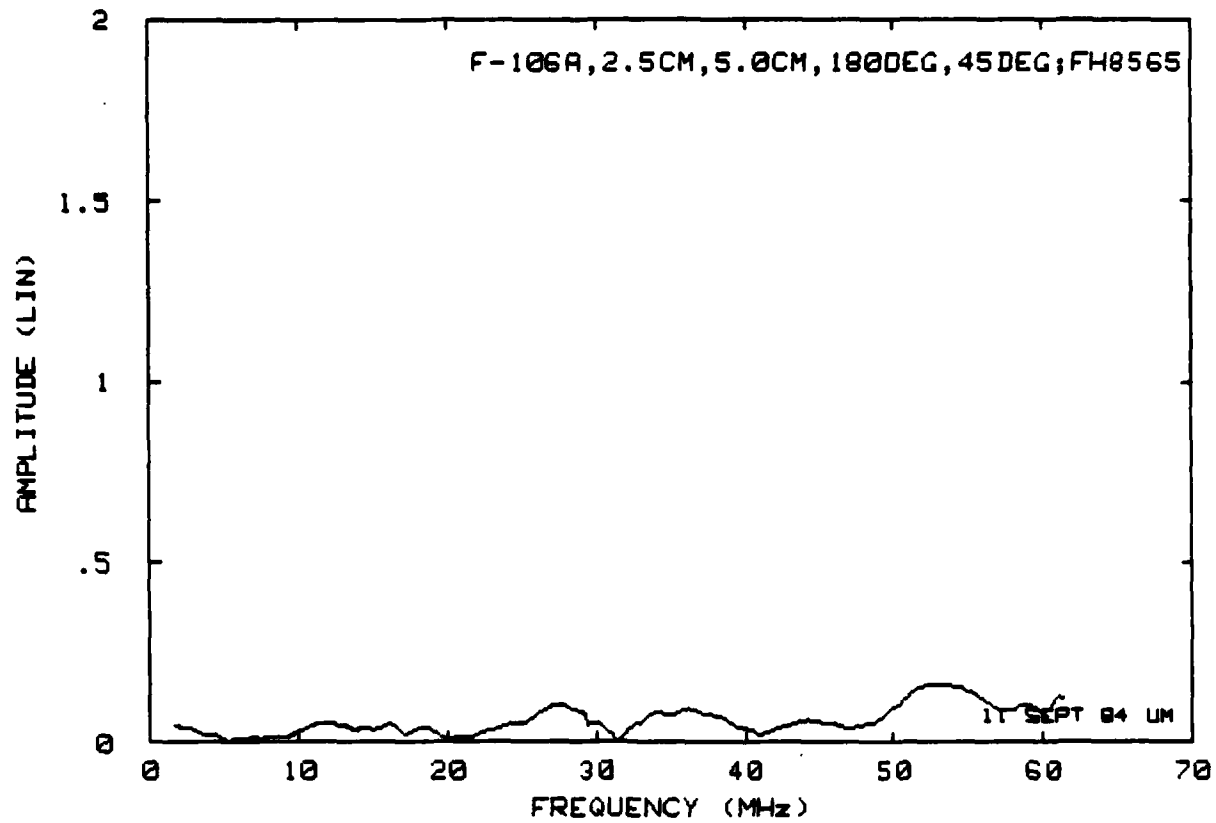
Reference files:

- (1) FH8533
- (2) FH8601

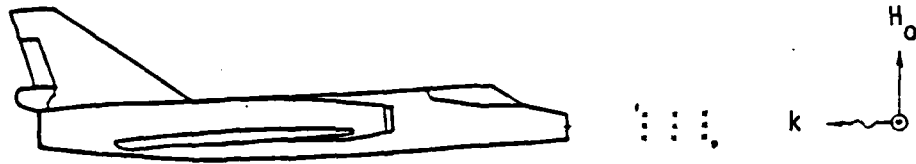
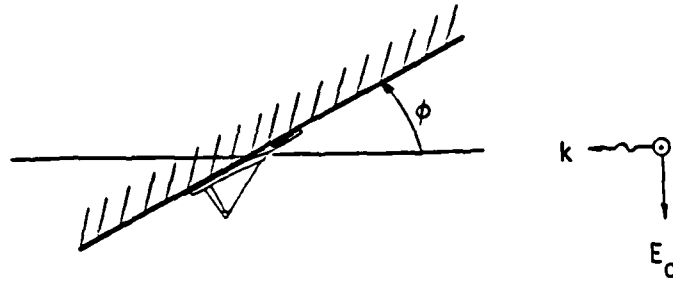
Set 3.7(a): E_1 and E_2 for nose-on incidence, H-vertical, $\phi = 45$ deg.



Set 3.7(b): Normalized field at position 4.



Set 3.7(c): Normalized field at position 6.

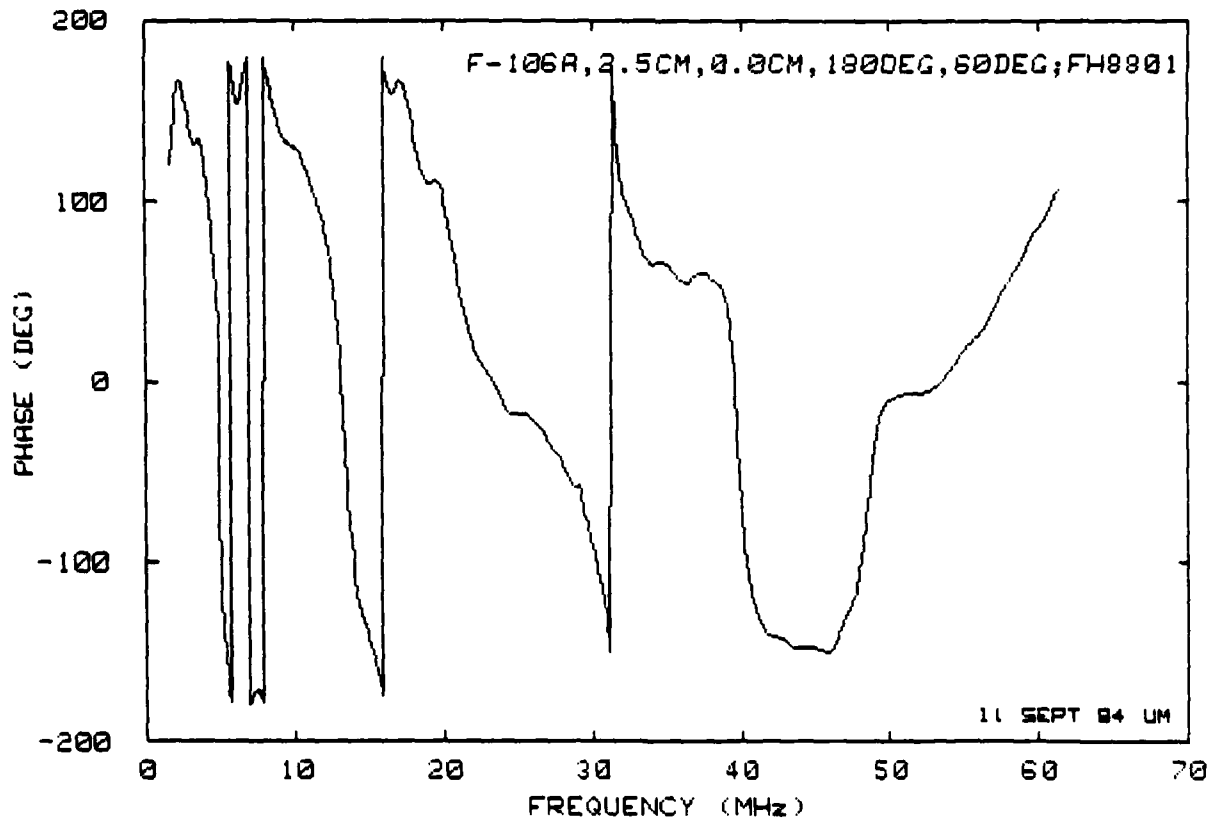
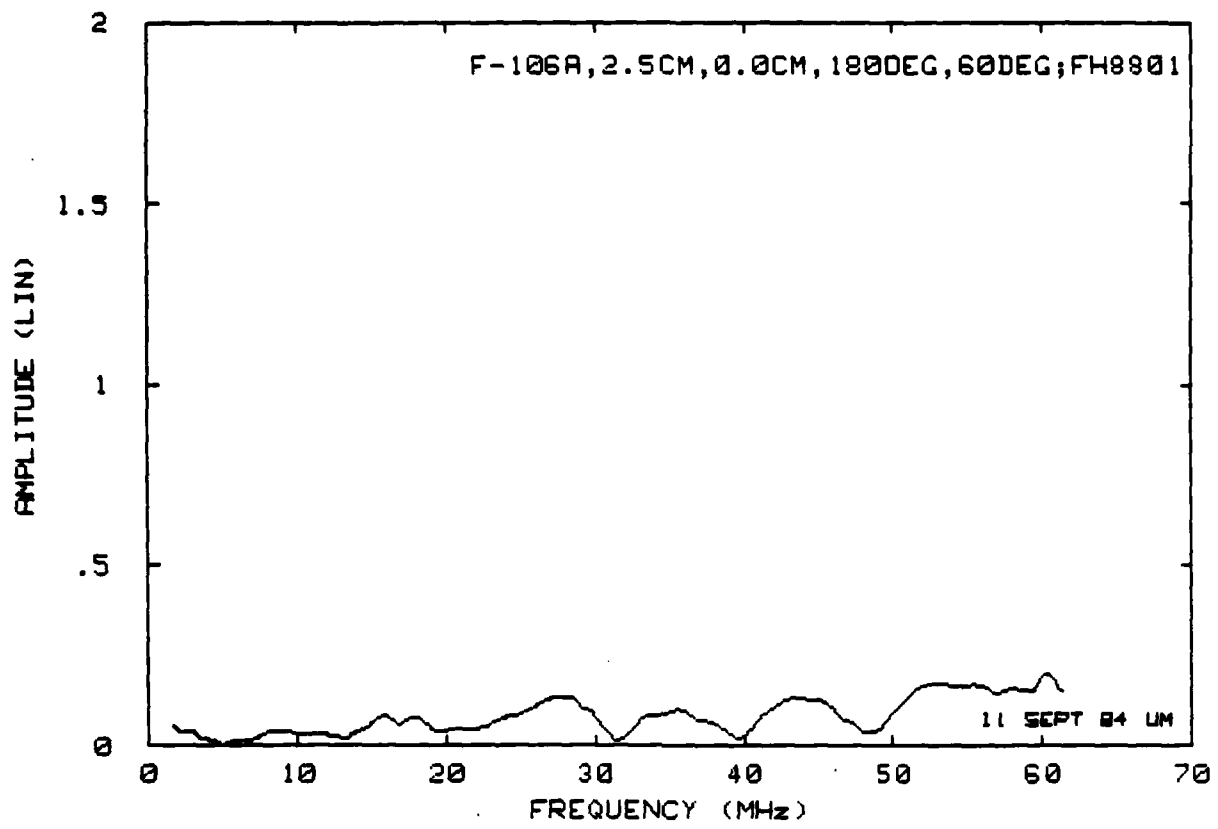


		Position		File		
1 (1) FH8749	2.13	2 (1) FH8757	0.82	3 (1) FH8773	0.64	E_1
	2.51		1.03		0.72	E_2
4 (1) FH8801	2.16	5 (2) FH8809	0.82	6 (2) FH8817	0.79	
	2.47		0.95		0.93	
7 (2) FH8825	2.09	8 (2) FH8841	1.03	9 (2) FH8849	0.86	
	2.30		1.17		0.99	

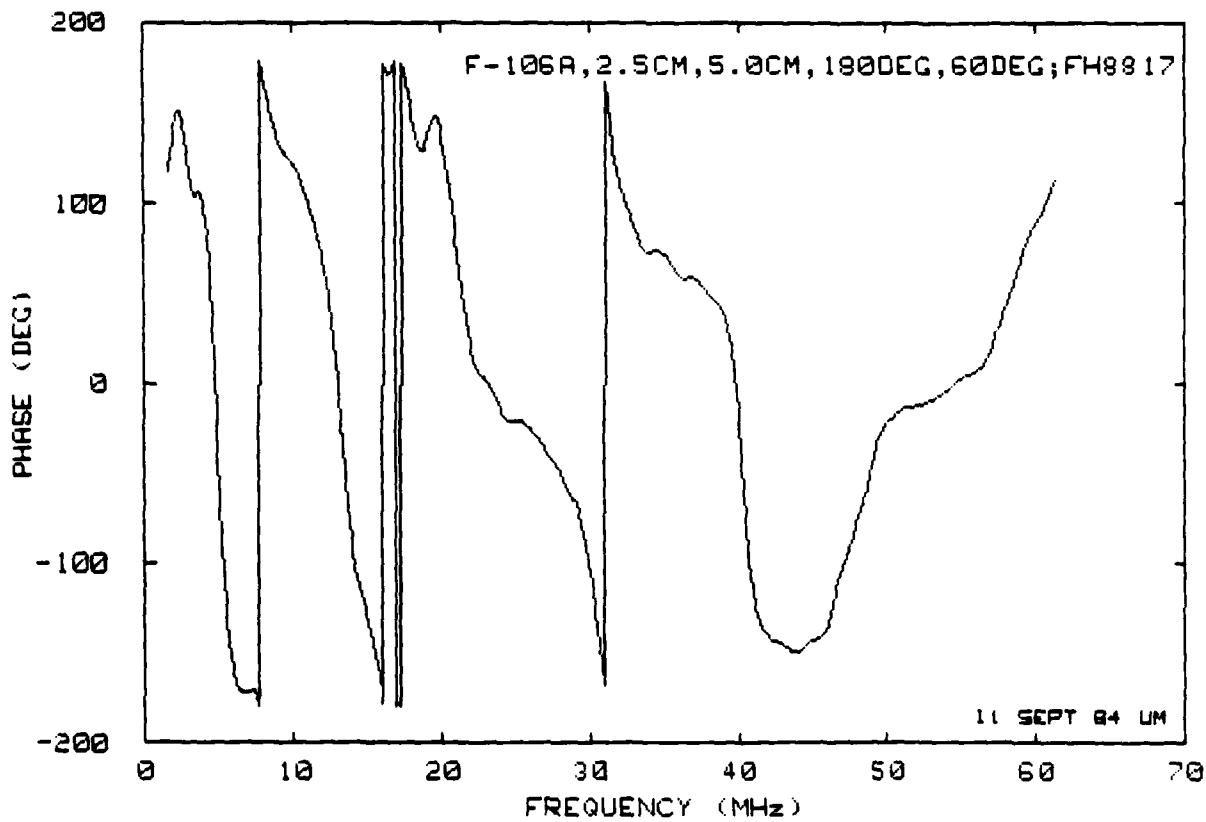
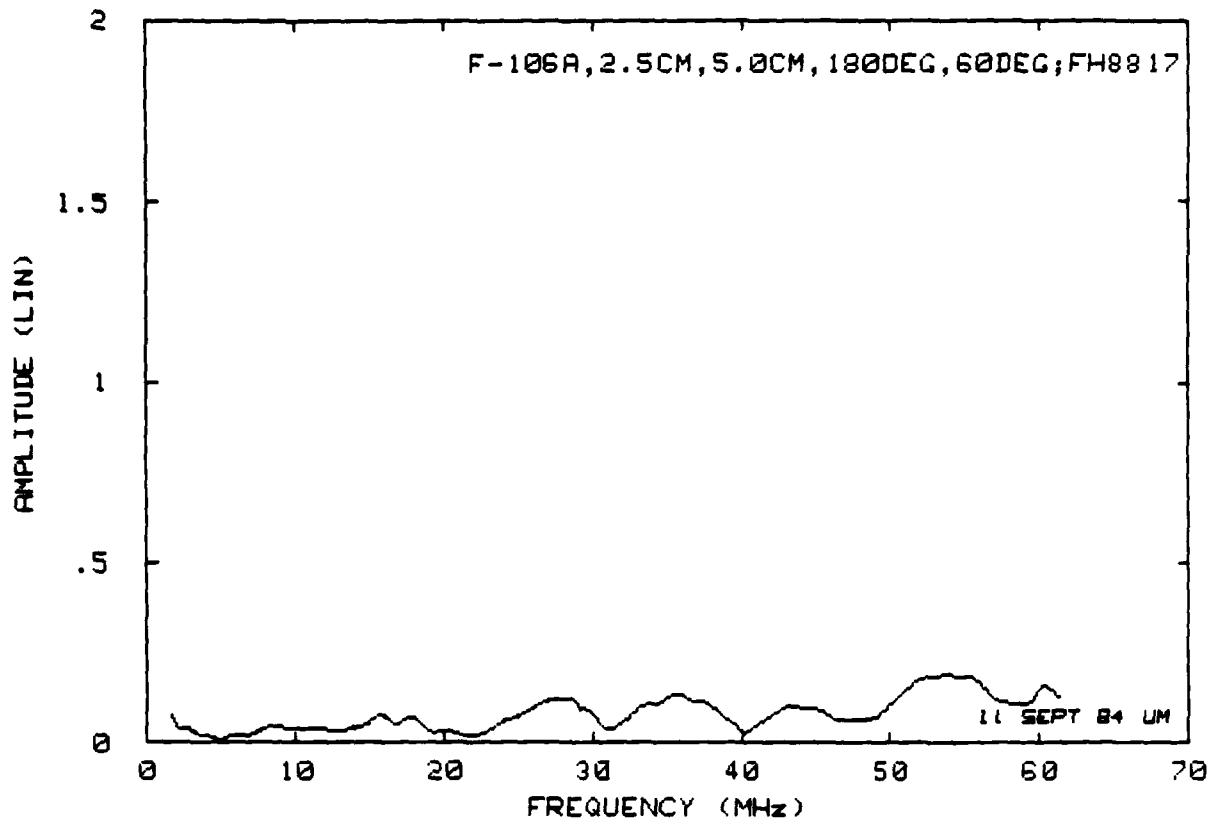
Reference files:

- (1) FH8765
- (2) FH8833

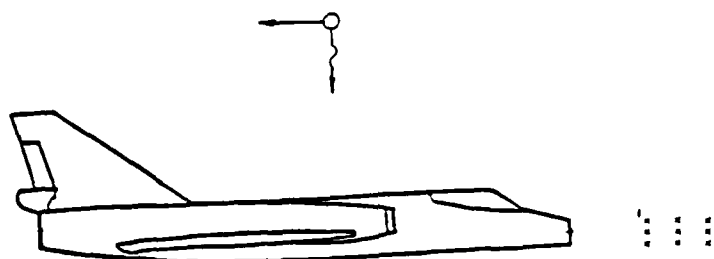
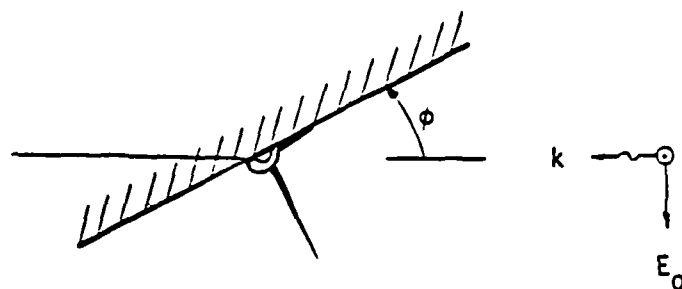
Set 3.8(a): E_1 and E_2 for nose-on incidence, H-vertical, $\phi = 60$ deg.



Set 3.8(b): Normalized field at position 4.



Set 3.8(c): Normalized field at position 6.

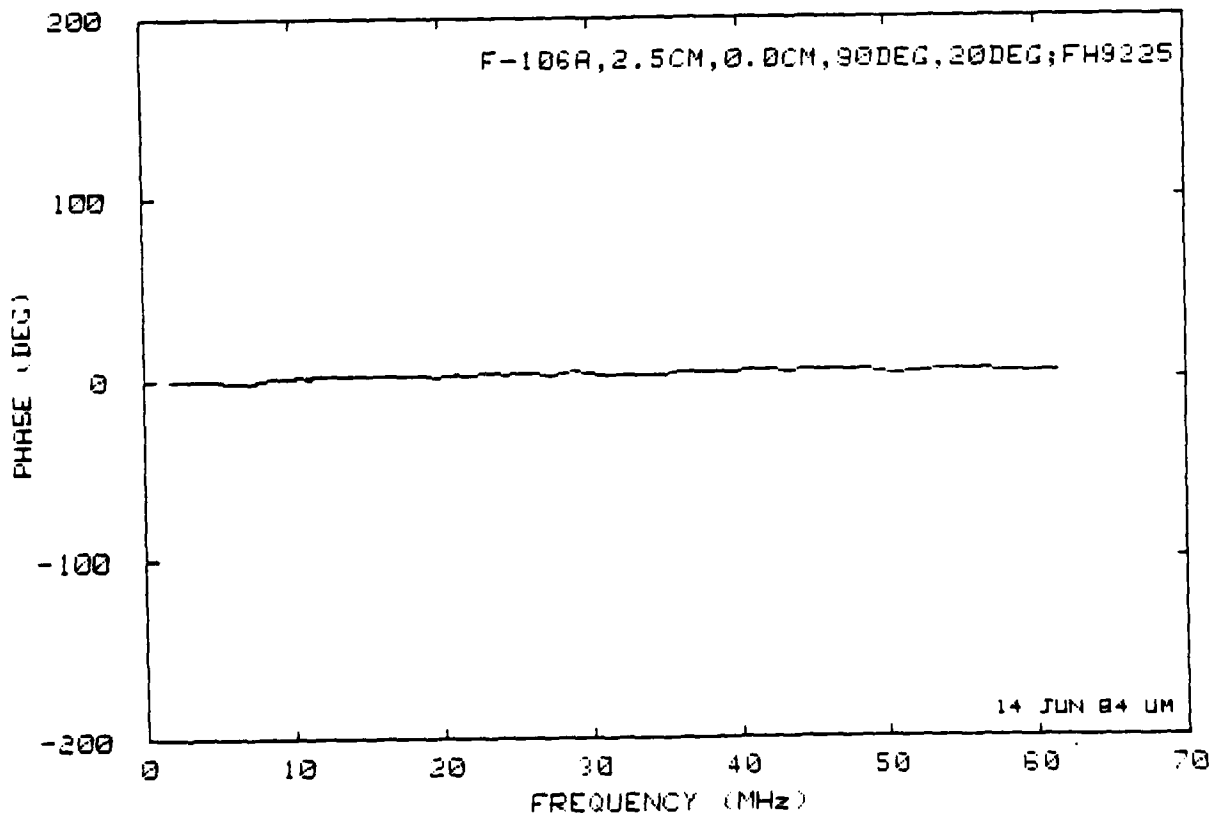
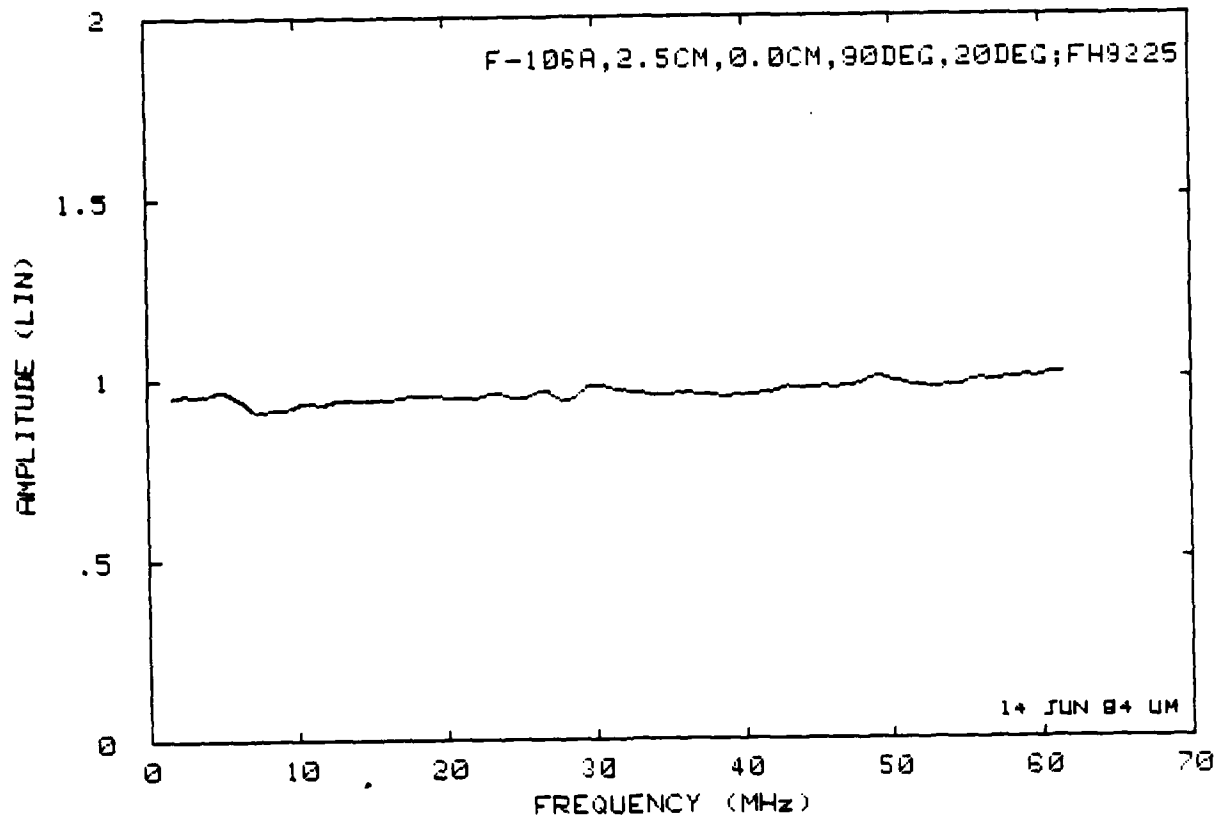


Position		File		E_1	E_2
1	4.34	2	1.98	3	1.62
FH9201	5.14	FH9209	2.17	FH9217	1.79
4	4.29	5	1.68	6	1.40
FH9225	4.73	FH9241	1.94	FH9249	1.56
7	4.10	8	2.38	9	1.70
FH9257	4.50	FH9265	2.72	FH9273	2.06

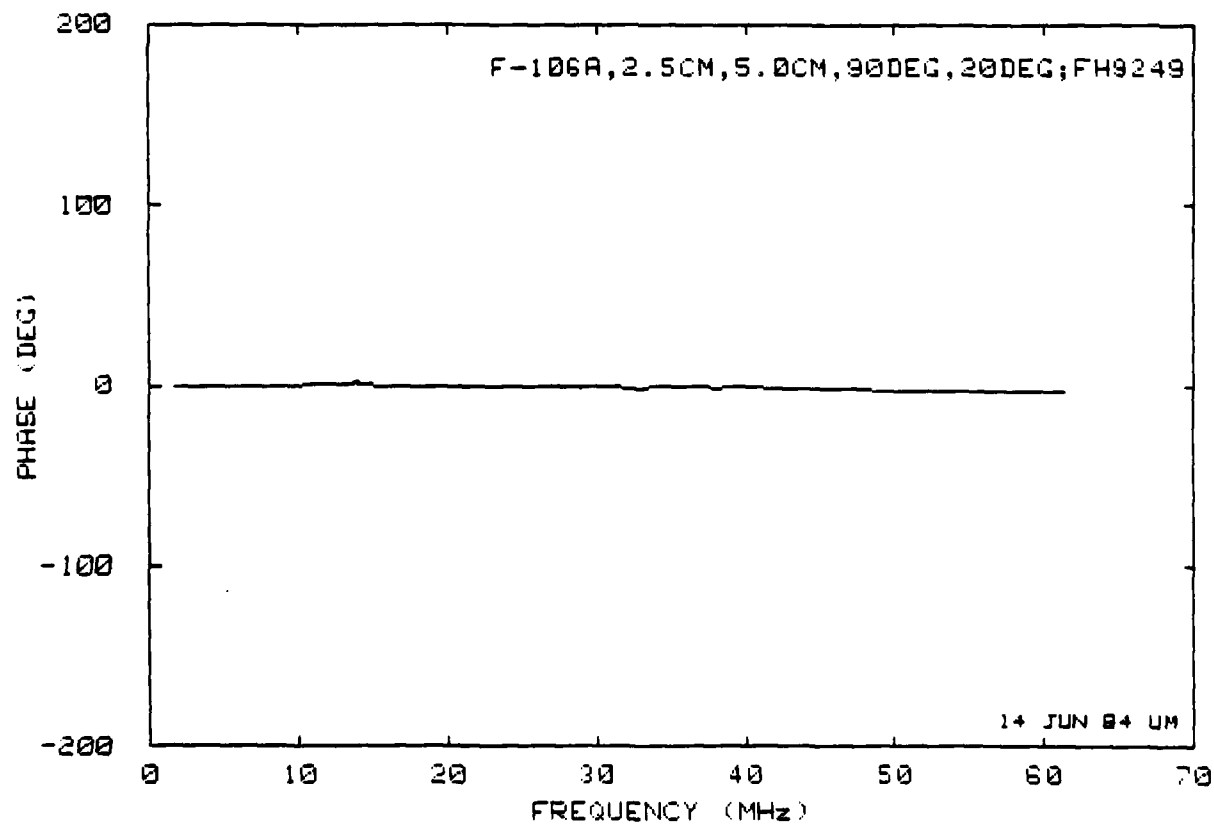
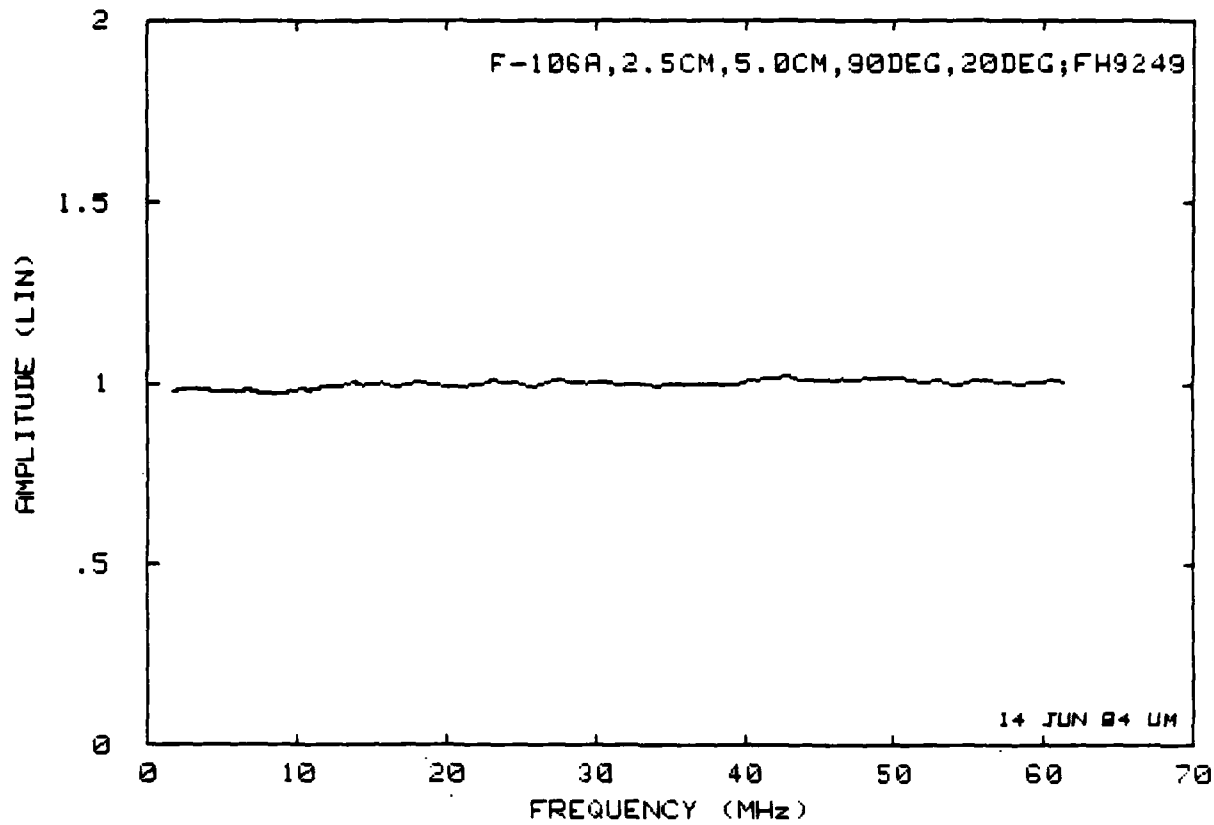
Reference file:

U-F106 (unity)

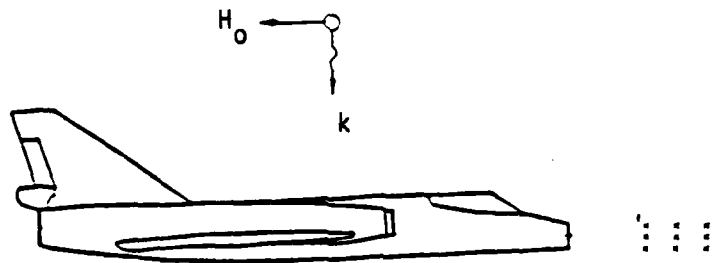
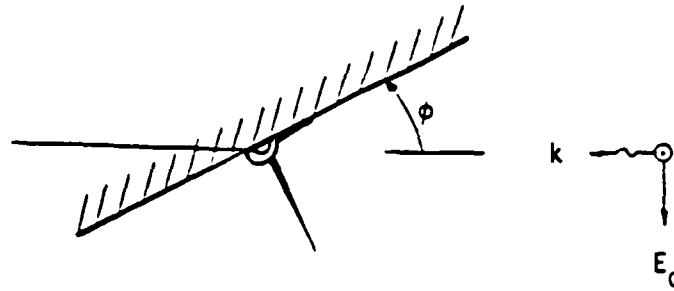
Set 3.9(a): E_1 and E_2 for top incidence, H-parallel to fuselage, $\phi = 0$ deg.



Set 3.9(b): Normalized field at position 4.



Set 3.9(c): Normalized field at position 6.

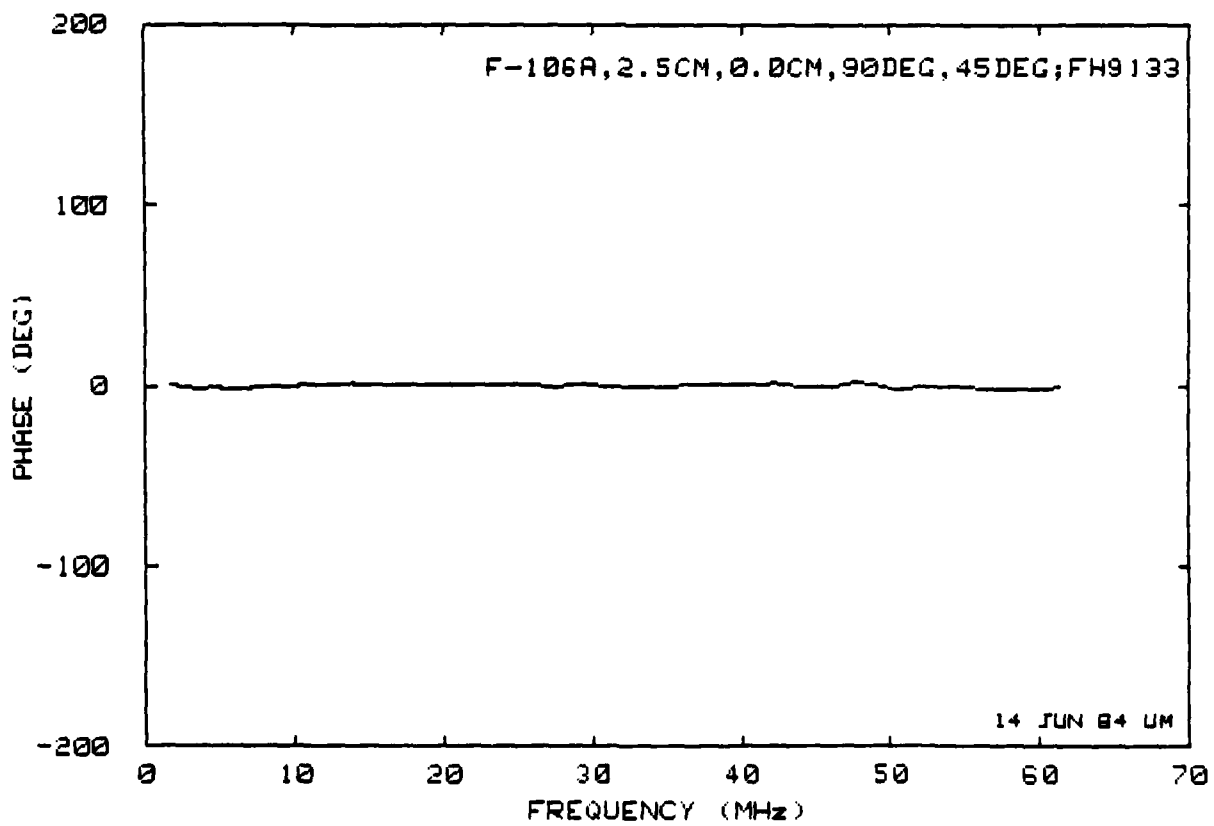
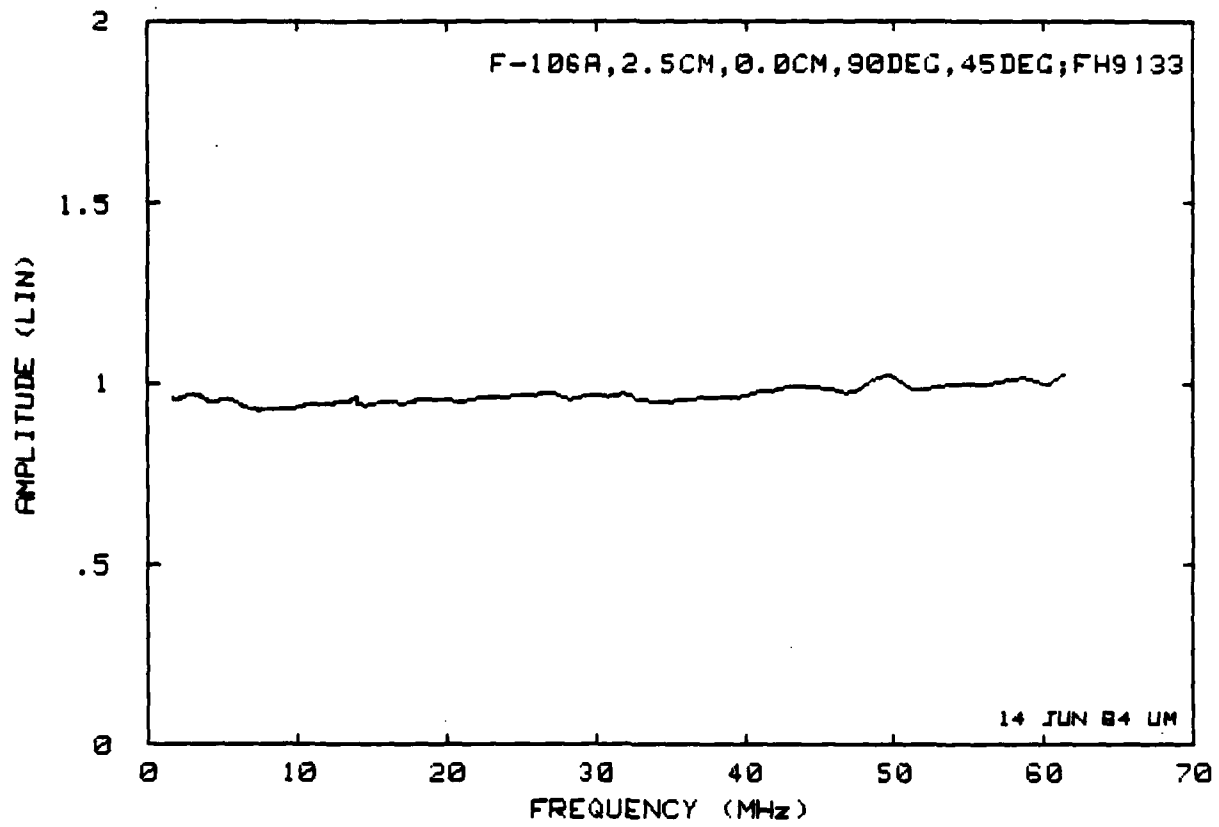


		Position		File		E_1	E_2
1	4.15	2	1.71	3	1.27		
FH9101	4.60	FH9109	1.95	FH9125	1.48		
4	3.88	5	2.86	6	2.42		
FH9133	4.28	FH9141	3.05	FH9149	2.92		
7	5.23	8	2.65	9	1.90		
FH9157	5.58	FH9165	2.85	FH9173	2.10		

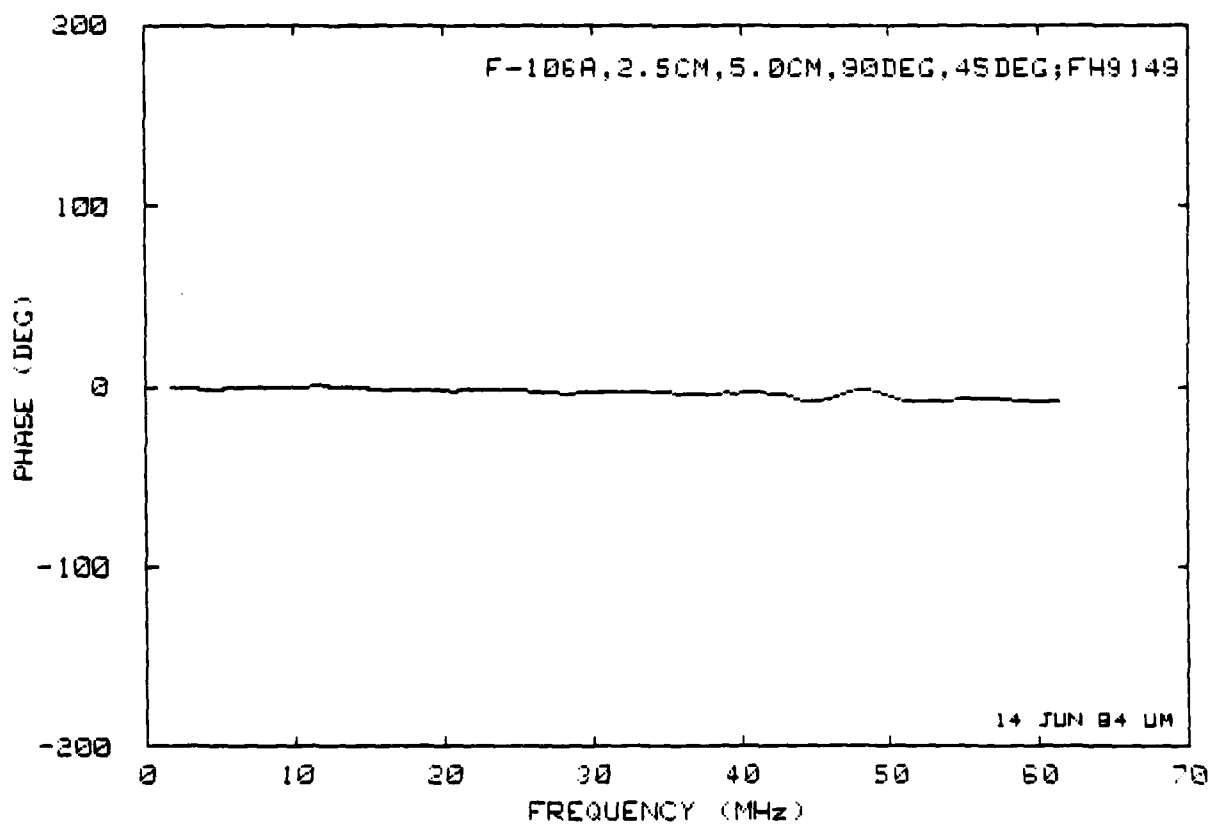
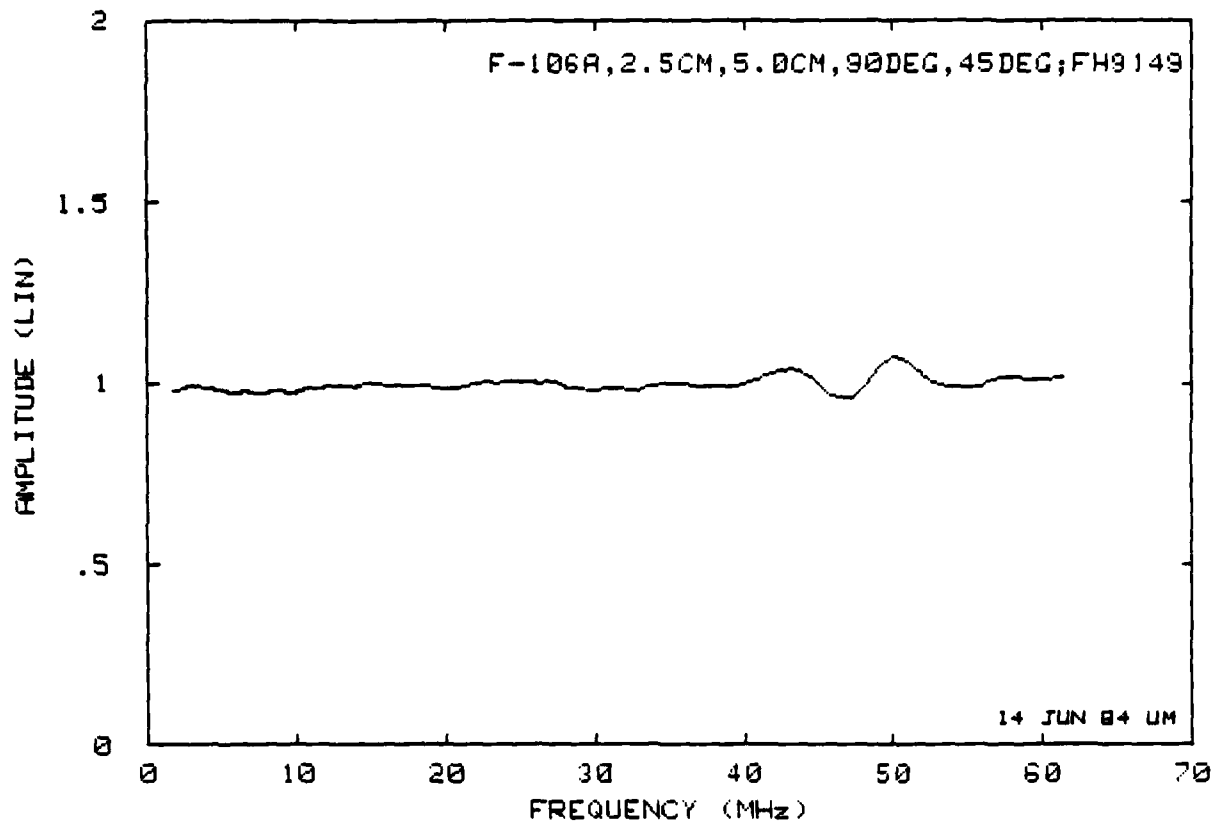
Reference file:

U-F106 (unity)

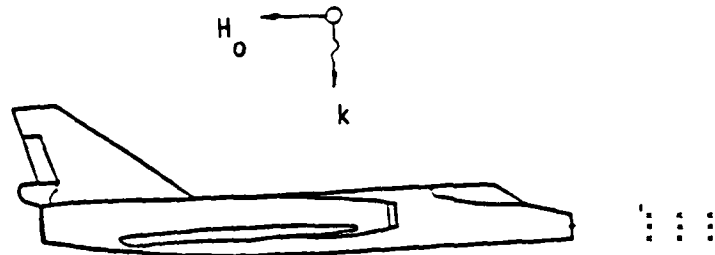
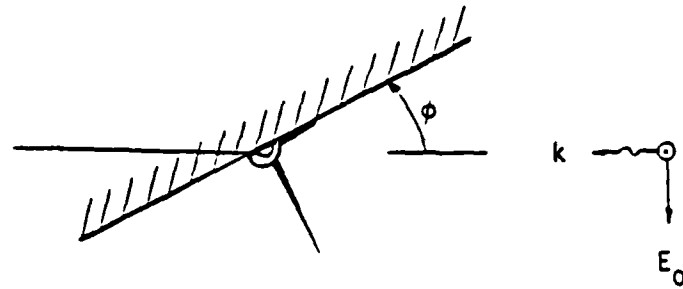
Set 3.10(a): E_1 and E_2 for top incidence, H-parallel to fuselage, $\phi = 45$ deg.



Set 3.10(b): Normalized field at position 4.



Set 3.10(c): Normalized field at position 6.

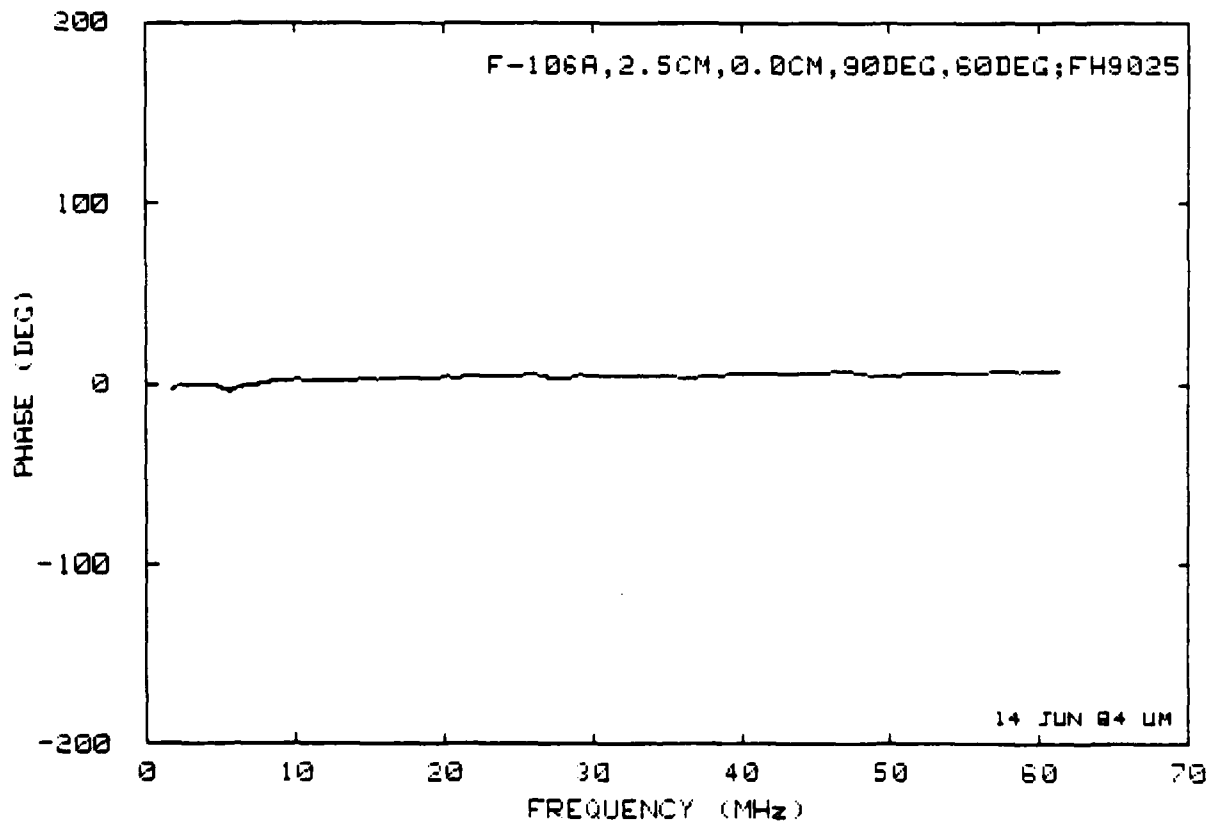
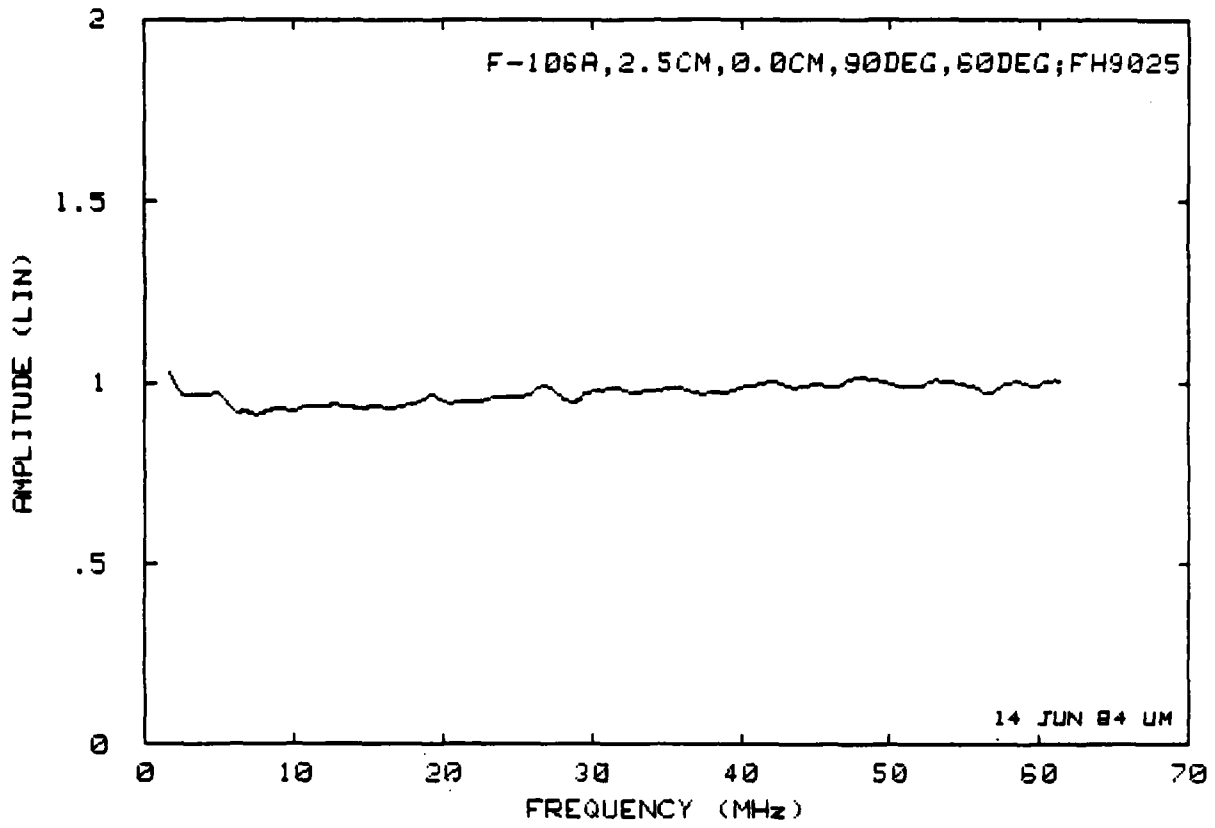


Position		File		E_1	E_2
1	4.31	2	2.60	3	2.30
FH9001	5.23	FH9009	2.89	FH9017	2.54
4	3.77	5	2.55	6	2.27
FH9025	4.48	FH9033	2.75	FH9049	2.36
7	5.21	8	2.96	9	2.25
FH9057	5.72	FH9065	3.25	FH9073	2.56

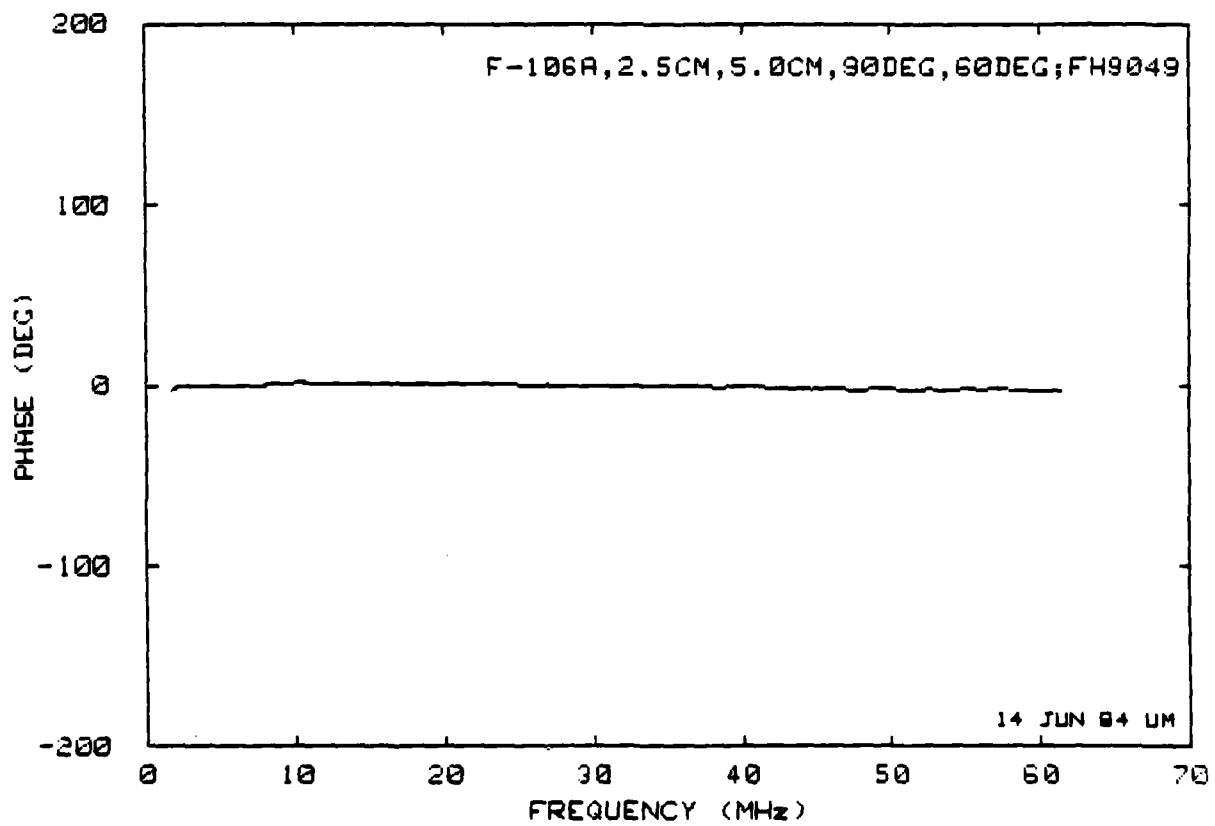
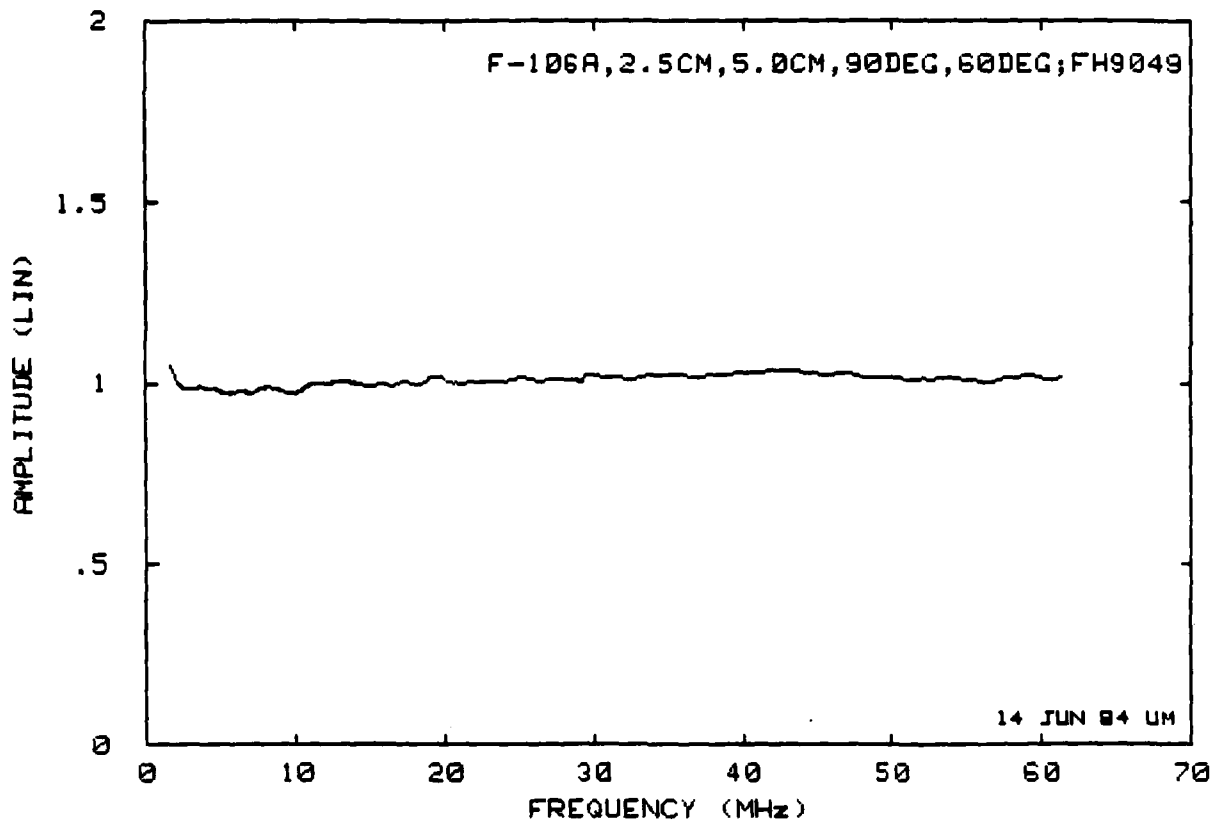
Reference file:

U-F106 (Unity)

Set 3.11(a): E_1 and E_2 for top incidence, H-parallel to fuselage, $\phi = 60$ deg.



Set 3.11(b): Normalized field at position 4.



Set 3.11(c): Normalized field at position 6.

IV. FREE SPACE MEASUREMENTS

Not all of the incident field excitations that are of interest can be simulated in the ground plane configuration, which basically limits the measurements to the case of E-perpendicular to the fuselage or antisymmetric excitations. With free space measurements the limitations are not as severe, but there is a possibility that an external sensor and its metallic leads may cause undue interference with the incident field and the model. By careful alignment of the lead normal to the incident electric field and keeping this lead extending away from the model, the interaction can be kept down to a negligible level.

1. MODEL, SENSORS, AND MEASUREMENTS

To perform the free space measurements the ground plane was removed from the chamber and the Styrofoam support pedestal which is used to support the free space models was reinserted. The instrumentation and data acquisition procedures remained essentially the same.

The same size (1:72 scale) and make (Hasegawa, No. 1054) plastic model was built and prepared as discussed in Section 3.2, except it was not cut in half. Intentionally, the fuselage length and the wingspan were adjusted to dimensions of 1/71.8 scale the same as for the ground plane case. The model is that of the F-106A and there was no attempt to modify it into an F-106B version, since the difference in the two versions is in the canopies and has little effect on scattering by the forward region where the fields are being studied.

Two free-space probes or sensors were used for these measurements: (a) one MGL-9(R) and (b) our own make--a 3 mm dia shielded loop probe made of 0.020-in-dia coaxial. For measurements either probe was suspended down from the center into the chamber such that the coaxial lead was perpendicular to the incident electric field. The MGL-9(R) sensor has dual coaxial leads extending radially, and to adapt it to a situation that would measure the incident H-field and at the same time have the lead perpendicular to the E-field required bending the leads as shown in Figure 12. (An axial lead version of the sensor MGL-9(A) would be directly applicable but such was not

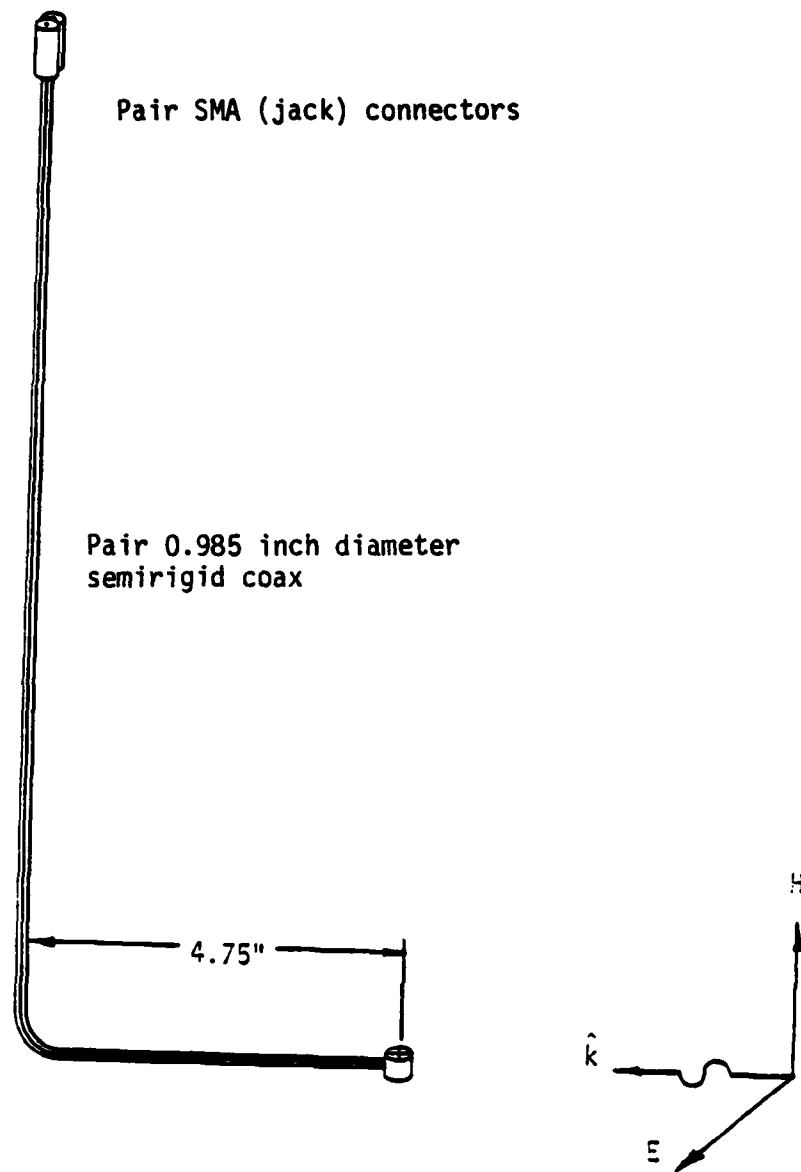


Figure 12. Modified MGL-9(R). The coaxial cables were bent 4.75 in from the loop to adapt for H-vertical polarization. In the original design, the coax was straight.

available.) The balanced two-wire output from the sensor was measured using a digital ballun whereby each side of the voltage was sequentially recorded with the other terminated in 50Ω and the resultant obtained by vector subtraction.

The MGL-9(R) probe was applicable to measure the vertical H-field but could not be used for the horizontal field component measurements. There we used our own make which, due to its 0.020 inch semirigid cable, could be bent to measure the horizontal component or the vertical component needed for the calibration.

2. MEASUREMENTS AND DATA

For all the orientations of the model that we measured, the axis of the sensor loop was always parallel to the fuselage, thus the (fuselage) axial magnetic field component was measured. For each excitation, measurements were made for nine probe positions relative to the aircraft as specified in Figure 2. The measurement procedures and data analyses follow and are similar to those used in the ground plane tests (Sec. 3.3). A total of six cases were studied, four for the case of H-parallel to the fuselage and two for the E-parallel to the fuselage.

Recall (Fig. 1) that in the chamber H_0 is vertical and E_1 is horizontal and the probe is suspended from the ceiling. For the case of H-parallel to the fuselage the model was supported vertically on its tail on the pedestal and moved through its nine measurement positions. The photograph in Figure 13 shows the measurement at position 9, top incidence parallel to the fuselage. The calibration measurement $v_0(f_n)$ is also the reference measurement $v_1(f_n)$ in this case, and is made with the model removed. Extreme care was taken not to touch or disturb the model in the process.

For the case of E-parallel to the fuselage the model was placed with the fuselage horizontal on the Styrofoam column and again repositioned through the nine measurement positions. For the reference measurement $v_1(f_n)$ the model was taken away, but for the calibration of the incident field the probe had to be bent to the shape shown in Figure 12 to measure the incident field $v_0(f_n)$. Actually, the current on a 3-in-dia sphere was measured and then

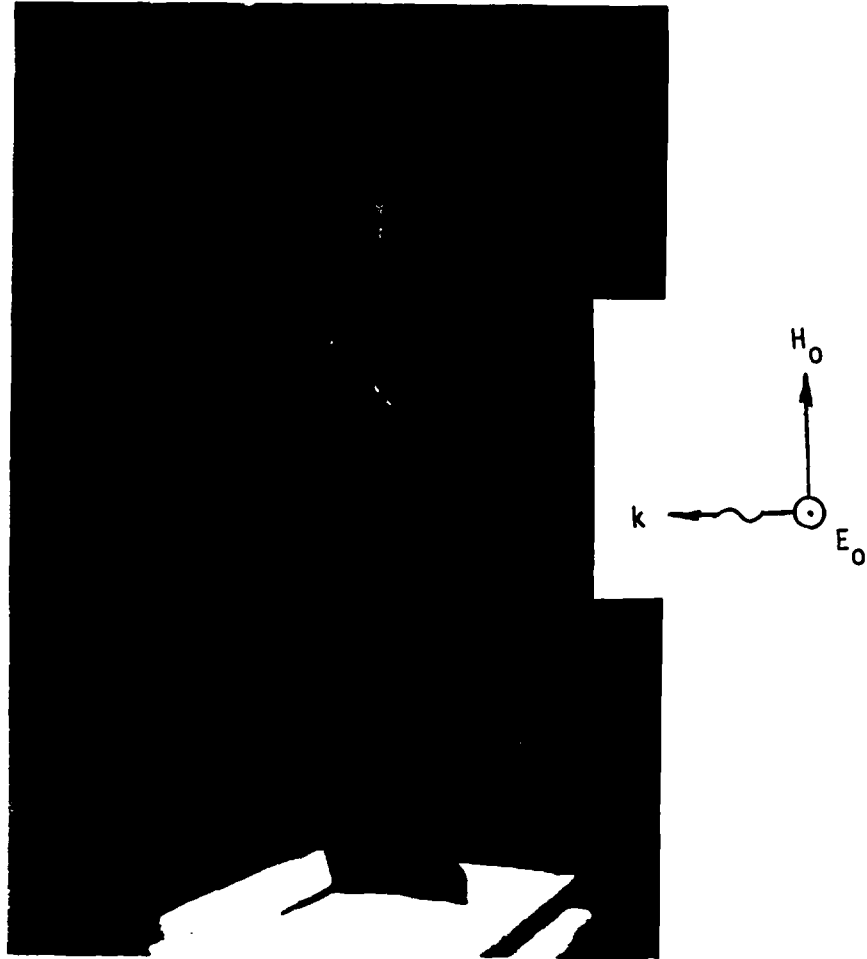


Figure 13. Photograph of the model set up in the chamber to measure the field at Pos. 9. A paper scale is attached to the model to locate the measurement positions. The probe is MGL-9(R); illumination Top, H-parallel to fuselage.

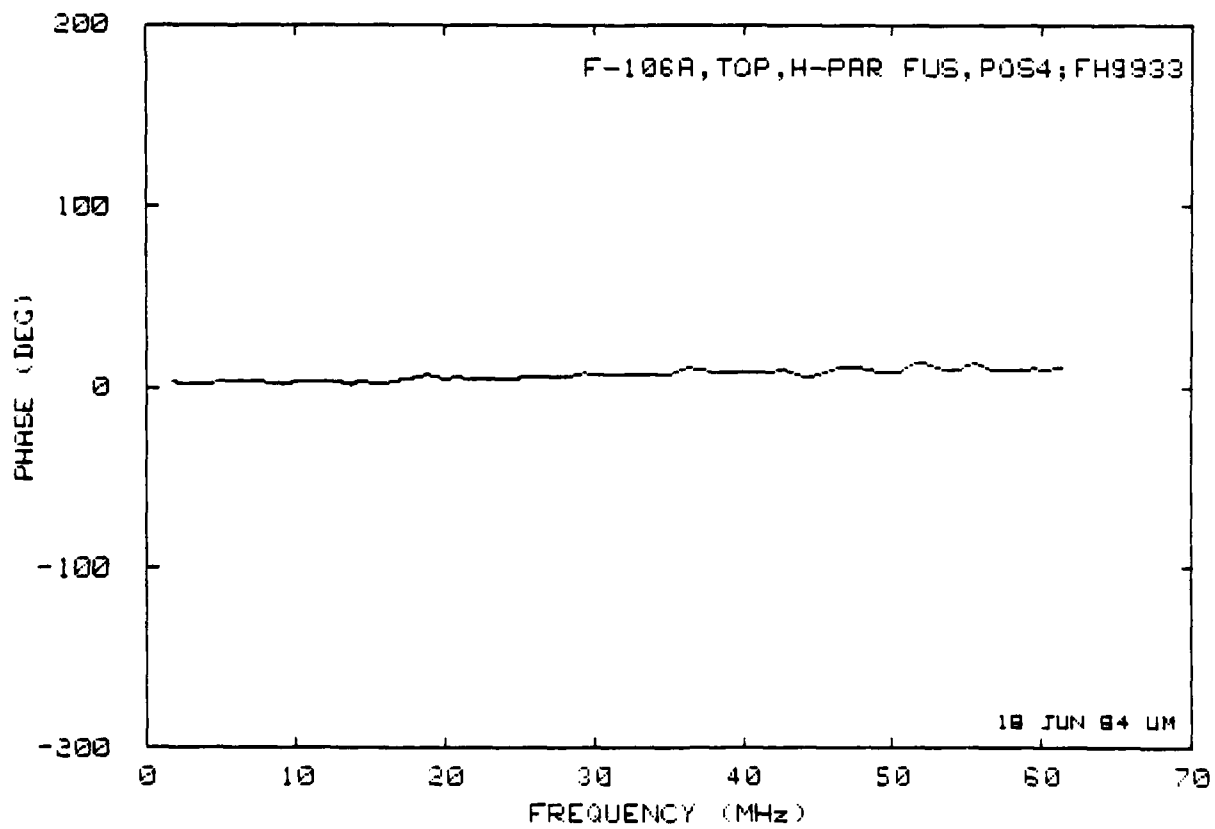
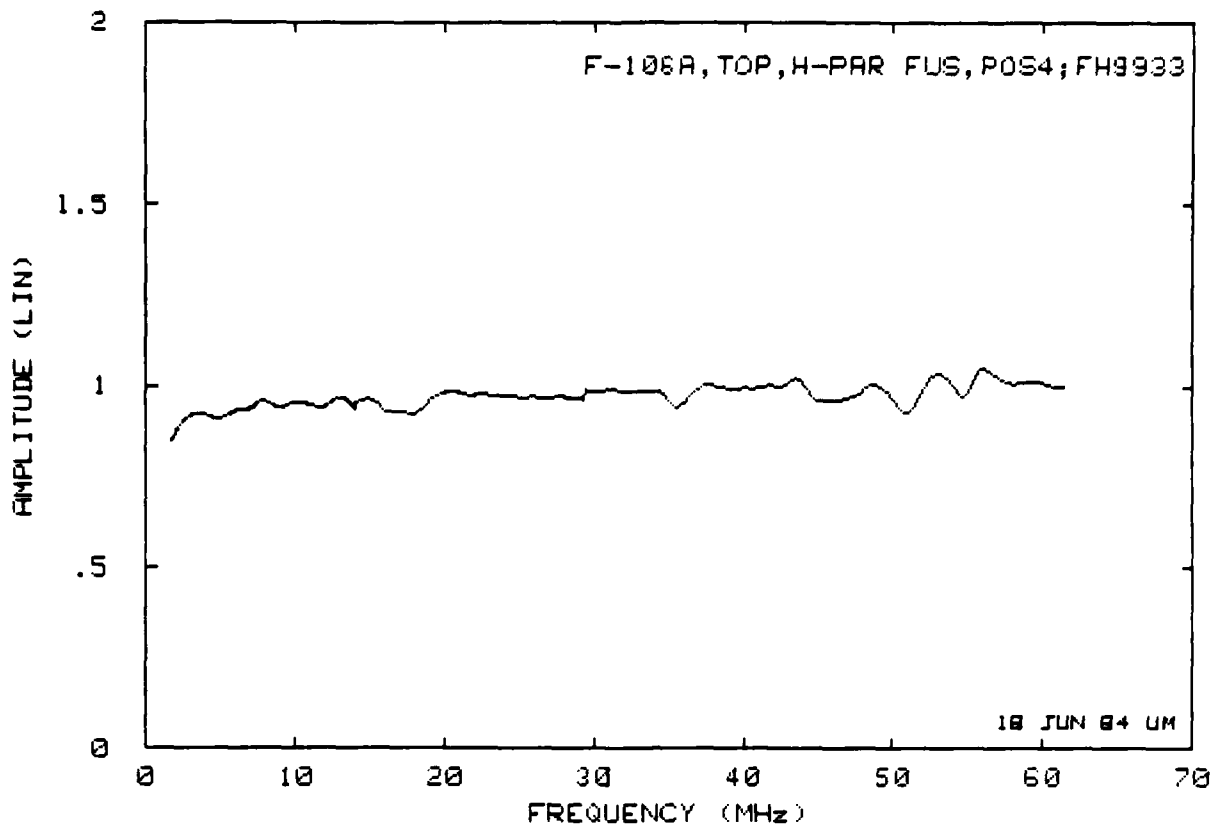
corrected for the sphere response to obtain the incident field H_0 , a technique developed and used in free space surface field measurements (Ref. 6).

Table 2 below shows the illumination situations measured and the data presented. The six data sets follow. Each data set contains information on the excitation, data files used, errors E_1 and E_2 , and the response curves for sensor positions 4 and 6. Again, in processing the data the phase K was adjusted for $\min E_1$ (Sec. 3.3) to compensate for the phase drift in the instrumentation.

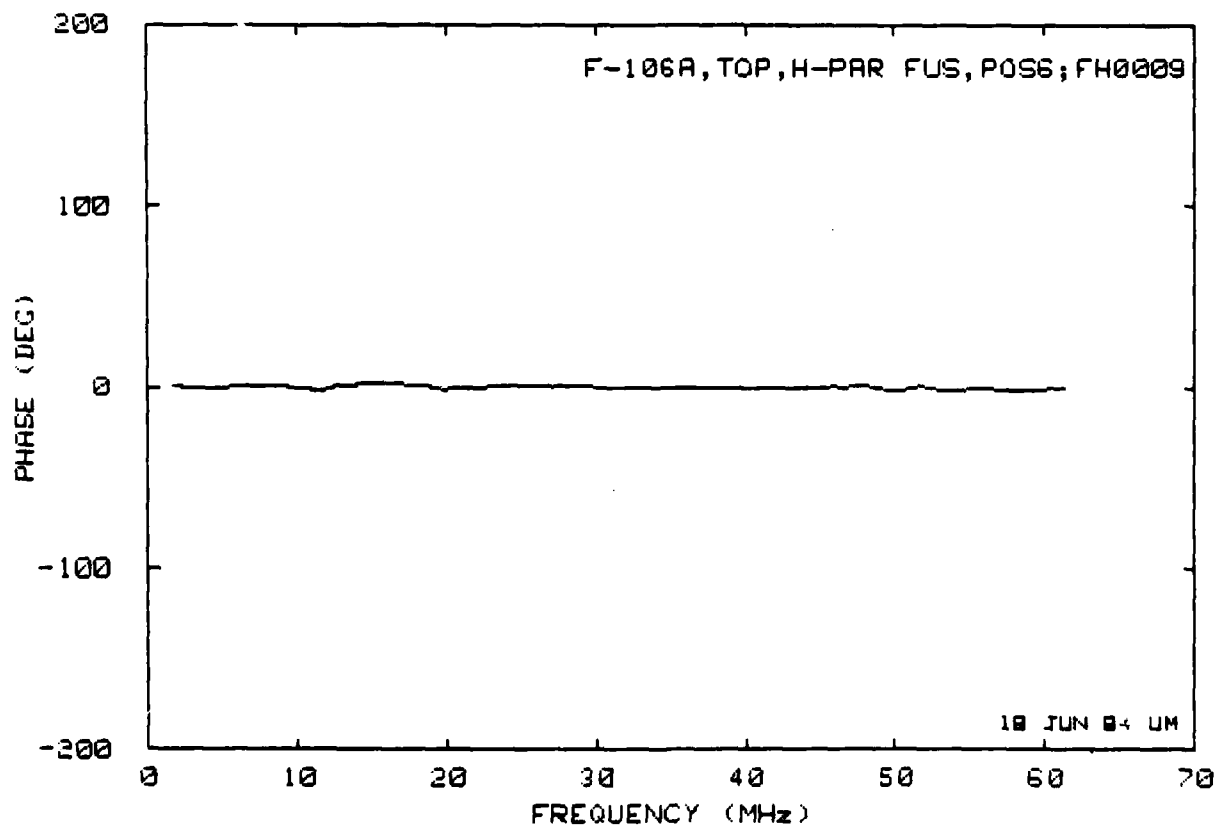
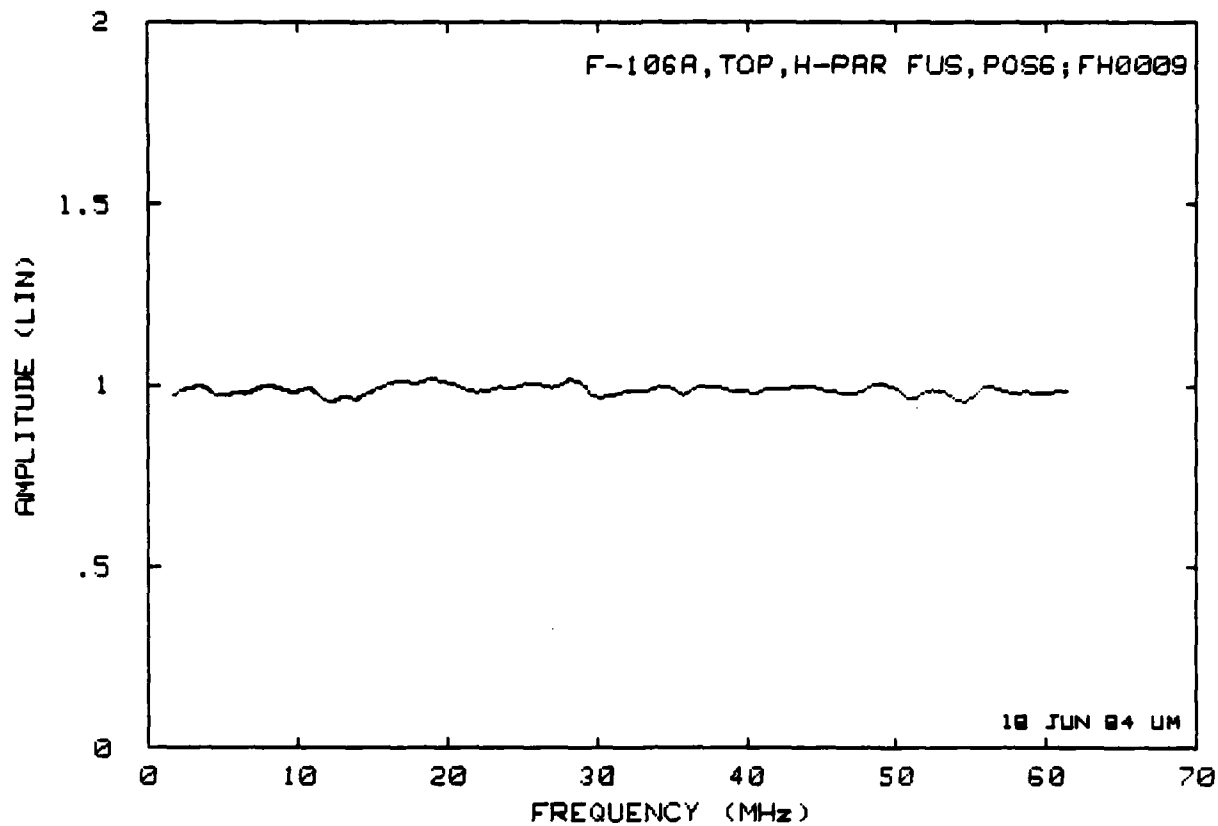
TABLE 2. SUMMARY OF FREE SPACE MEASUREMENTS

Incidence Polarization	Top	Bottom	Side	Side (-30)
H-parallel to fuselage	Set 4.1	Set 4.2	Set 4.3	Set 4.4
E-parallel to fuselage		Set 4.5	Set 4.6	

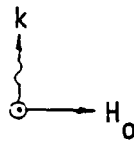
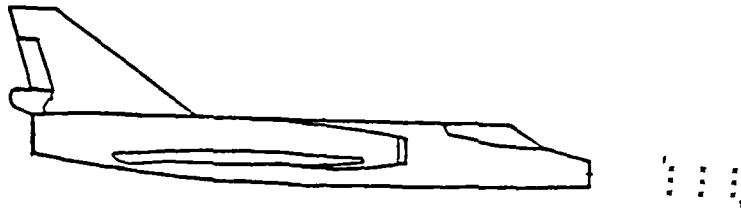
6. Liepa, V.V., and T.B.A. Senior, Measured Characteristics of Multi-gap Loop and Asymptotic Conical Dipole Electromagnetic Field Sensors, AFWL-TR-82-82, March 1983.



Set 4.1(b): Normalized field at Position 4.



Set 4.1(c): Normalized field at Position 6.

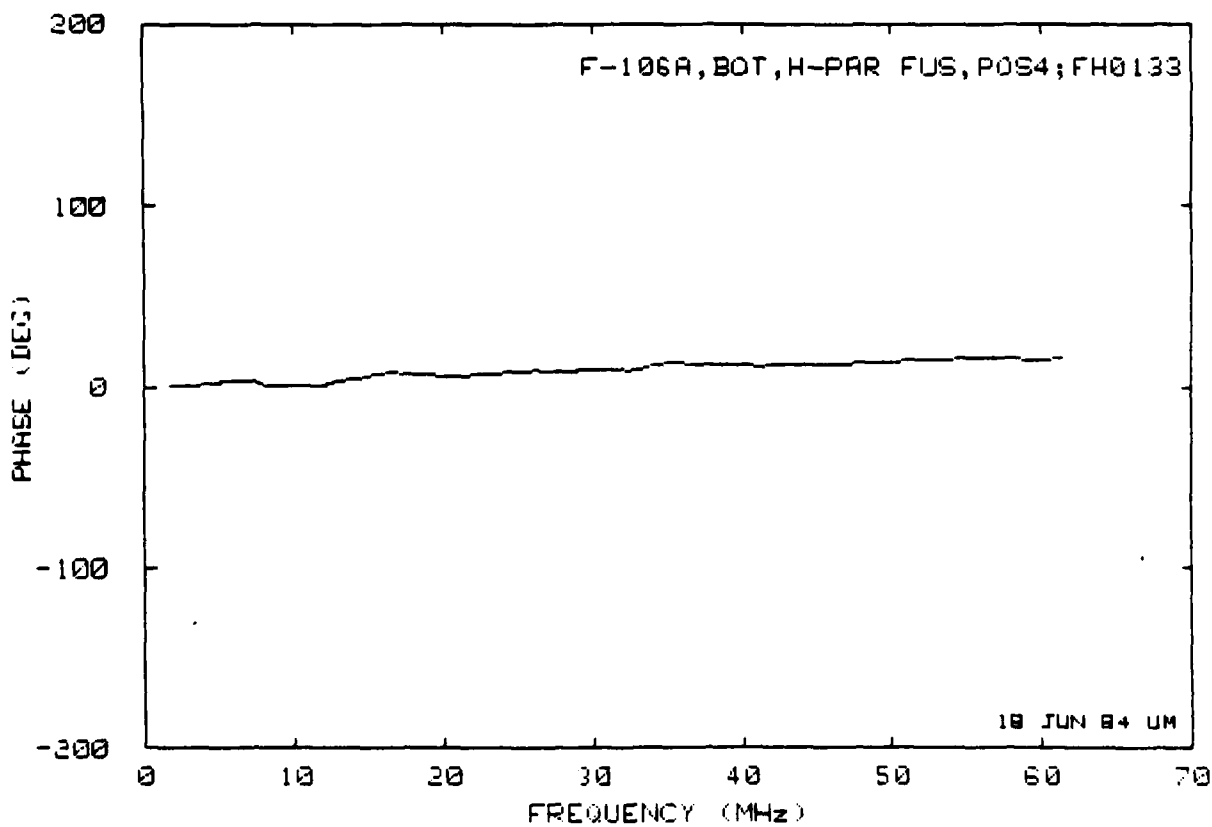
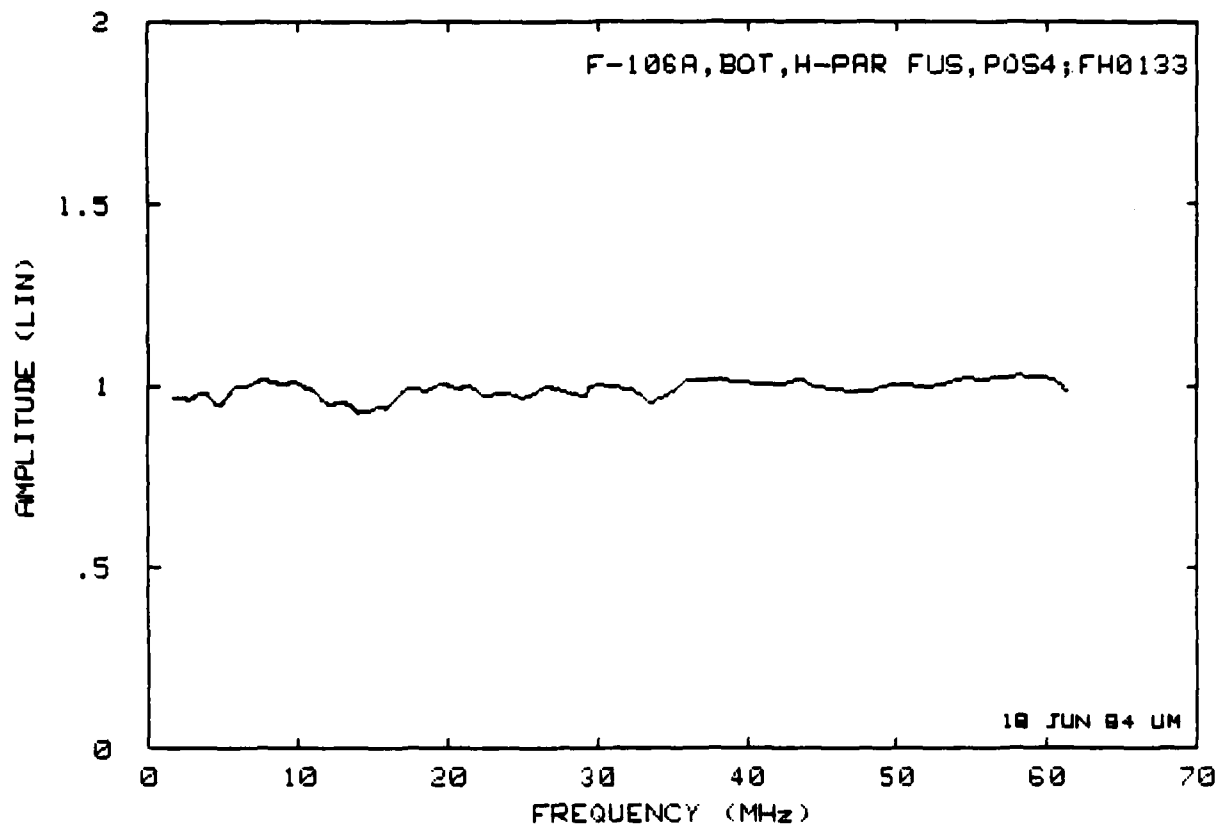


		Position	File		E_1	E_2
1	3.37	2	1.97	3	1.78	
FH0141	3.86	FH0165	2.44	FH0217	2.06	
4	2.78	5	1.92	6	1.70	
FH0133	3.33	FH0157	2.42	FH0209	2.02	
7	3.29	8	2.24	9	1.85	
FH0149	3.90	FH0173	2.62	FH0225	2.15	

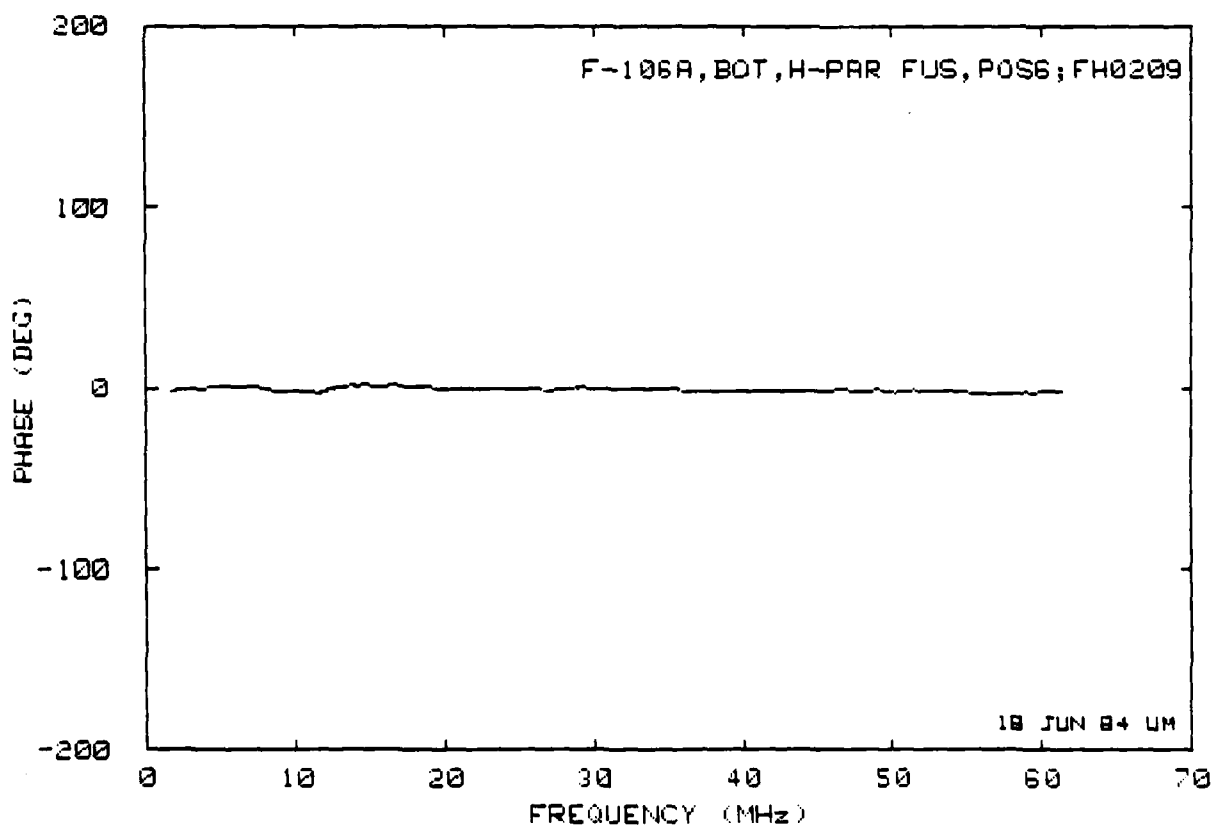
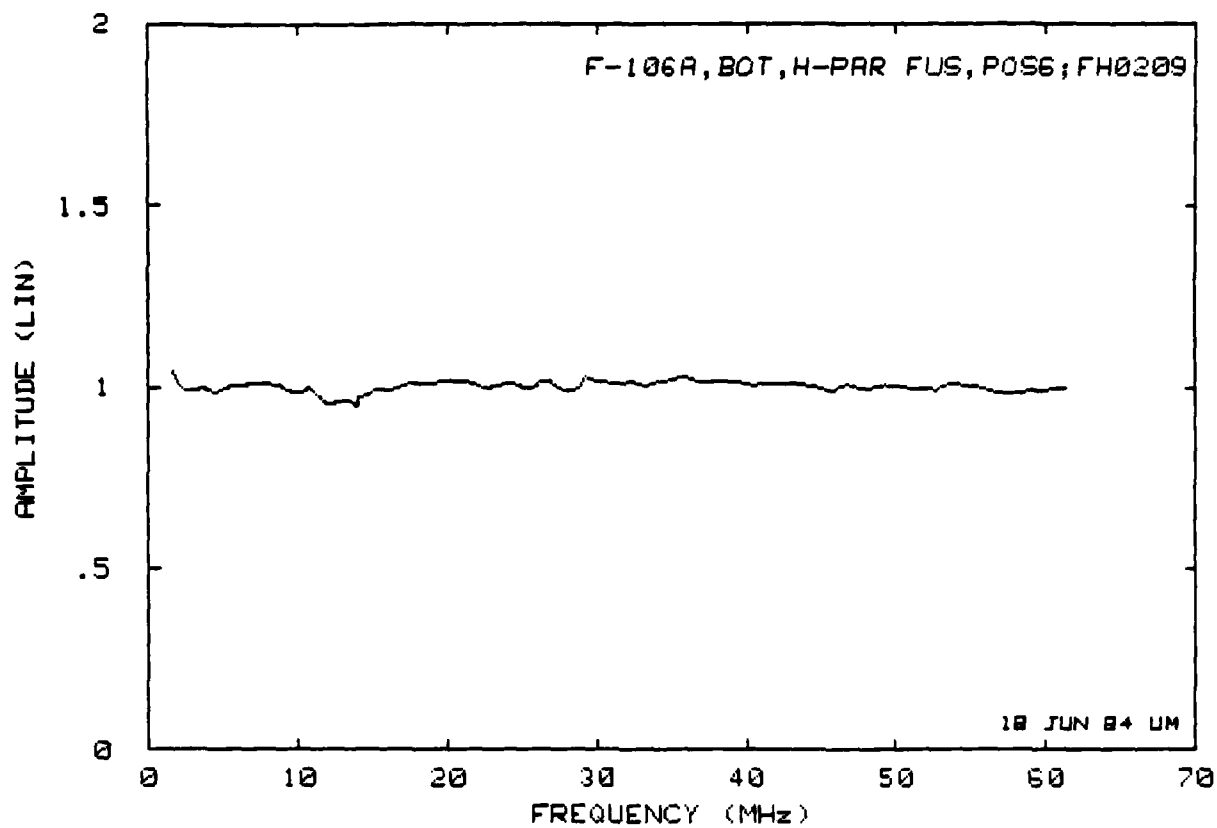
Reference file

U-F106 (unity)

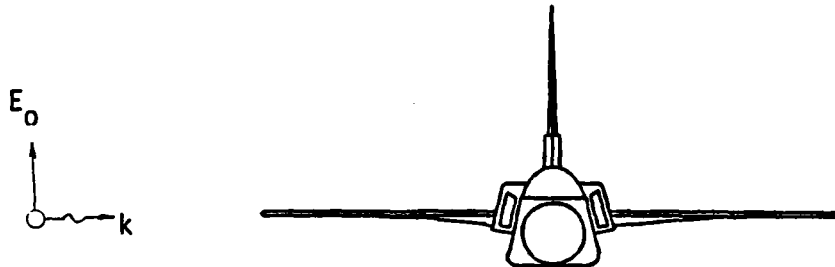
Set 4.2(a): E_1 and E_2 for bottom incidence, H-parallel to fuselage.



Set 4.2(b): Normalized field at Position 4.



Set 4.2(c): Normalized field at Position 6.



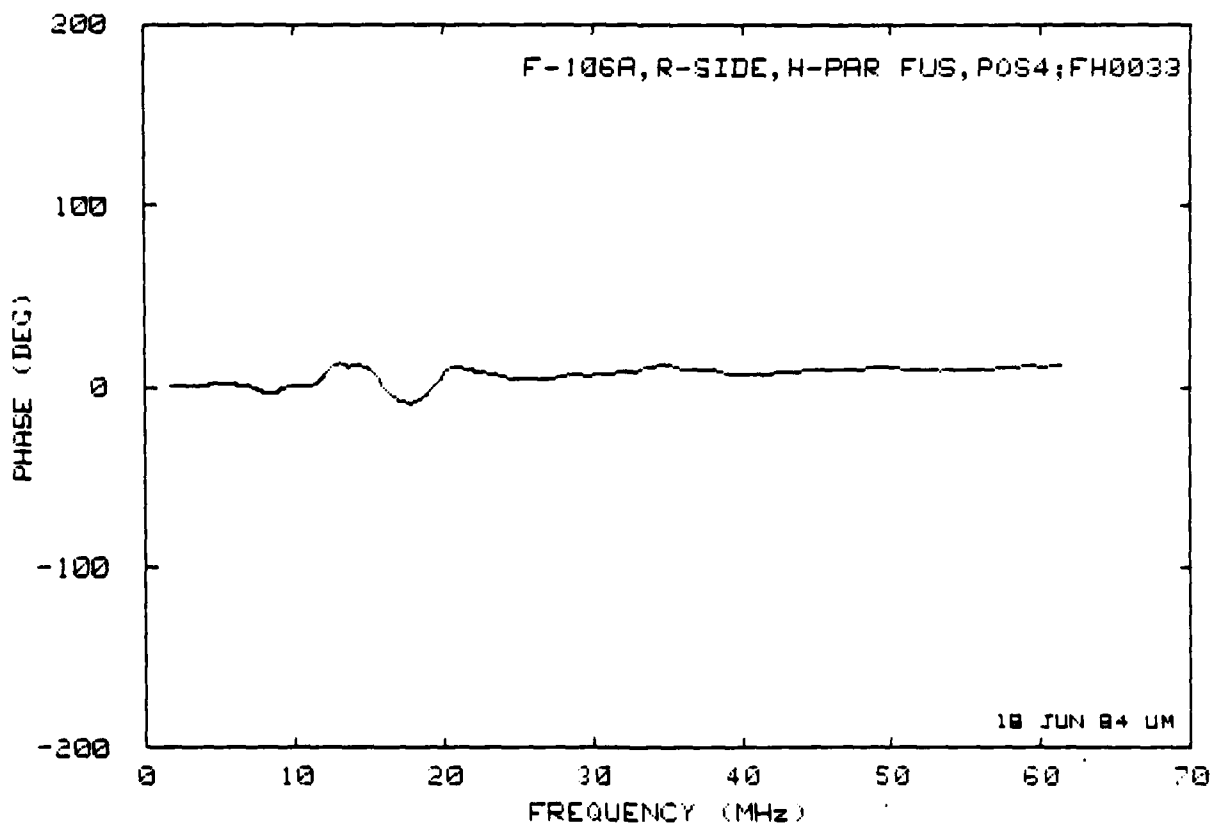
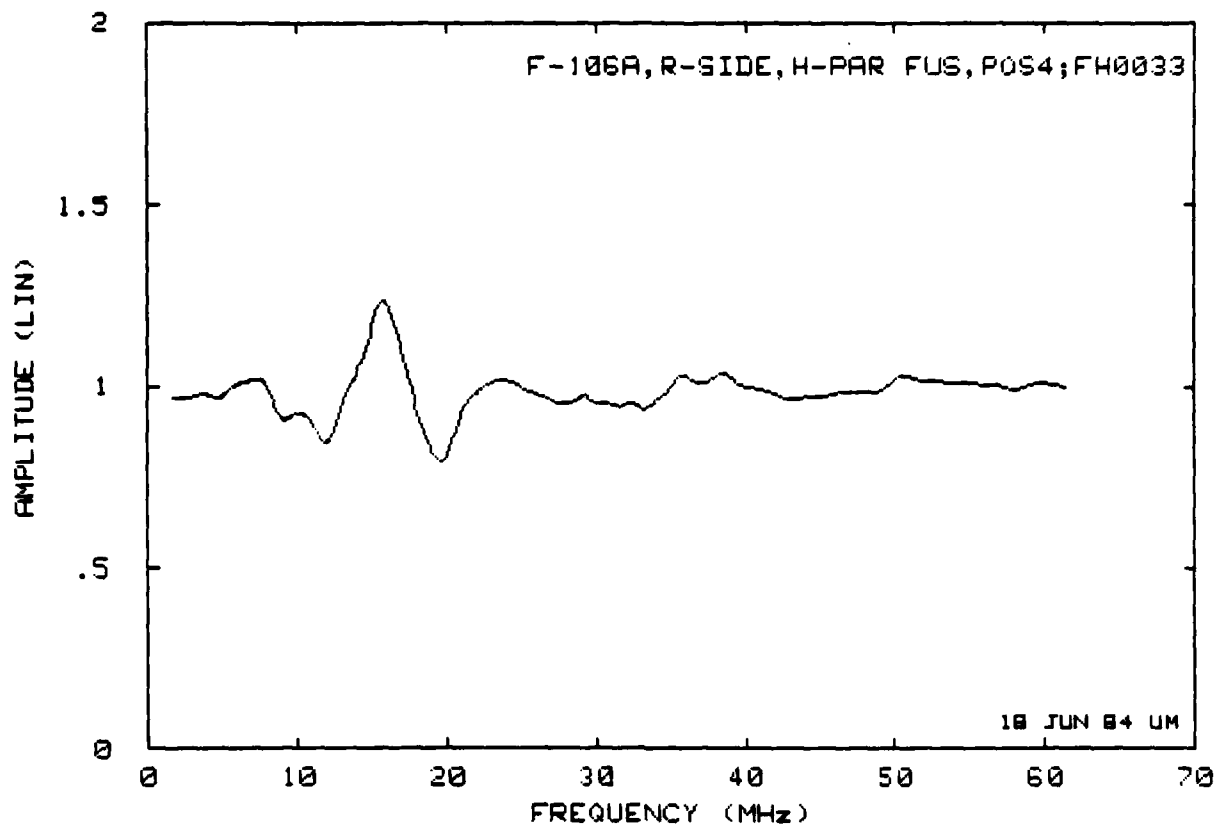
		Position		File	
1	6.37	2	4.43	3	3.84
FH0041	9.01	FH0065	6.54	FH0117	5.53
4	6.36	5	4.38	6	3.86
FH0033	9.07	FH0057	6.53	FH0109	5.62
7	6.06	8	4.31	9	3.81
FH0049	8.80	FH0073	6.50	FH0125	5.65

Labels E_1 and E_2 are positioned to the right of the table, with lines pointing to the rightmost column of data.

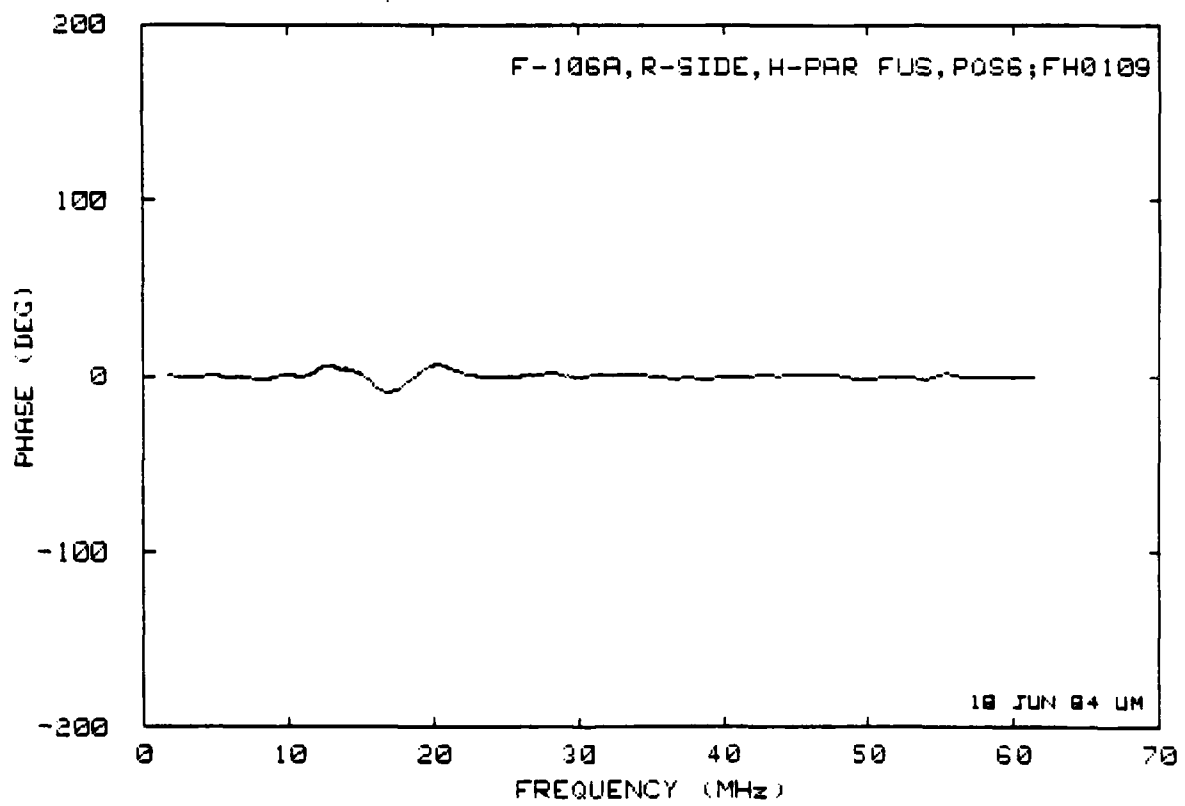
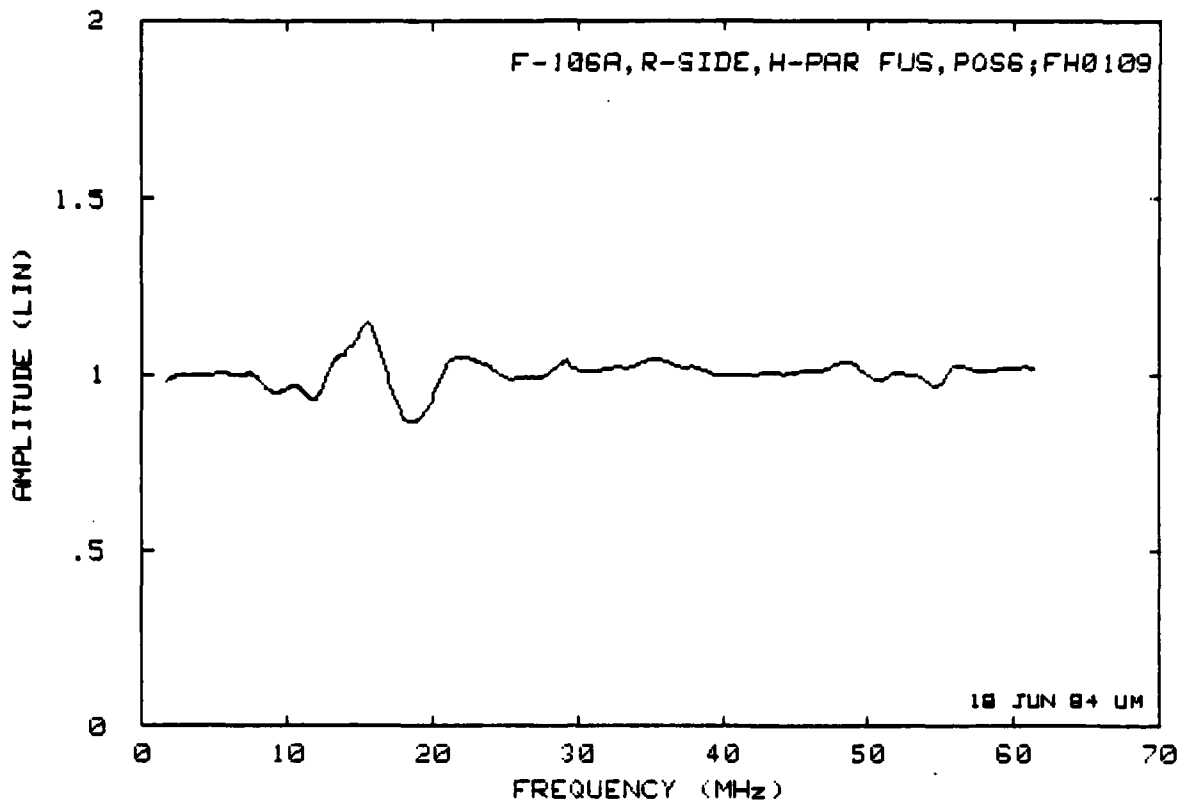
Reference File:

U-F106 (unity)

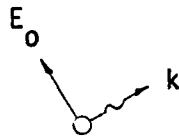
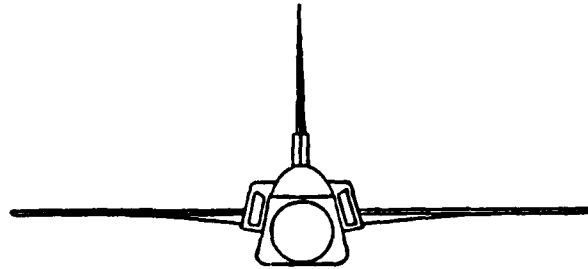
Set 4.3(a): E_1 and E_2 for right-side incidence, H-parallel to fuselage.



Set 4.3(b): Normalized field at Position 4.



Set 4.3(c): Normalized field at Position 6.

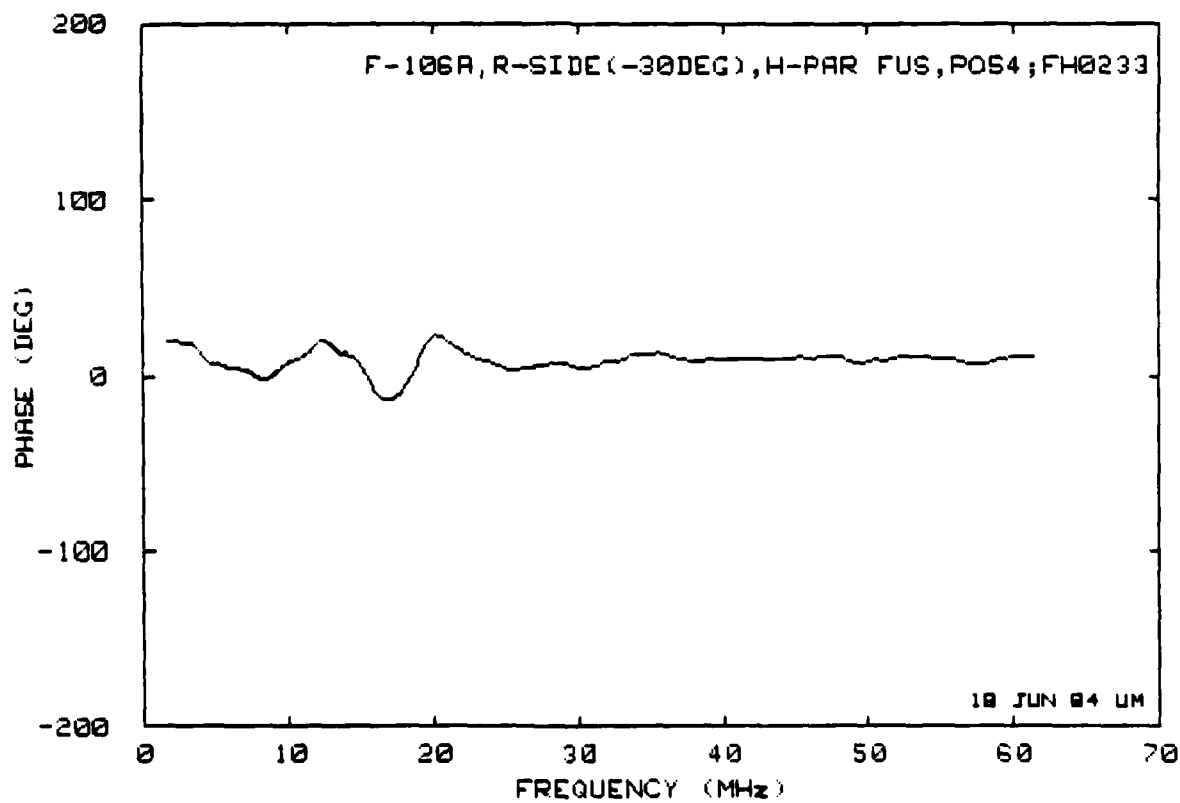
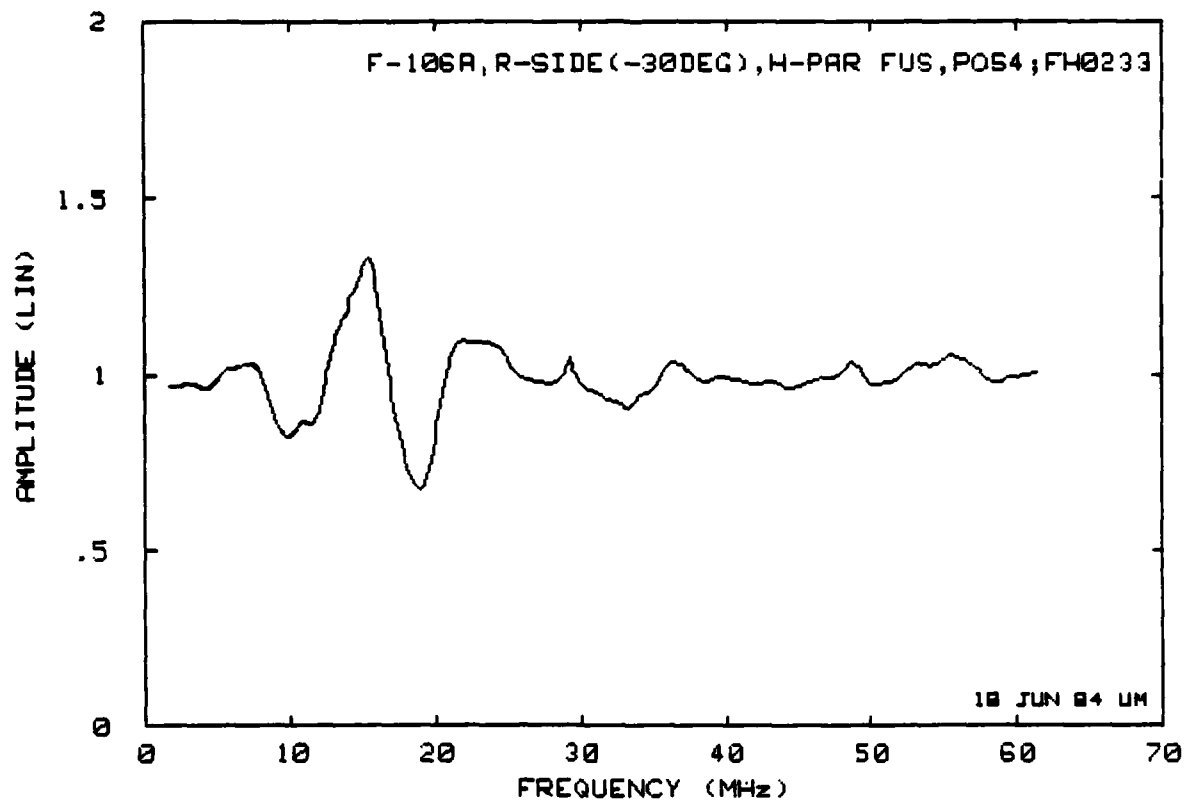


		Position		File		E_1	E_2
1	9.89	2	11.4	3	7.12		
FH0241	14.0	FH0265	14.3	FH0309	10.4		
4	11.1	5	7.77	6	8.39		
FH0233	15.4	FH0257	11.5	FH0301	11.9		
7	9.51	8	8.47	9	6.87		
FH0249	14.0	FH0273	12.3	FH0317	9.95		

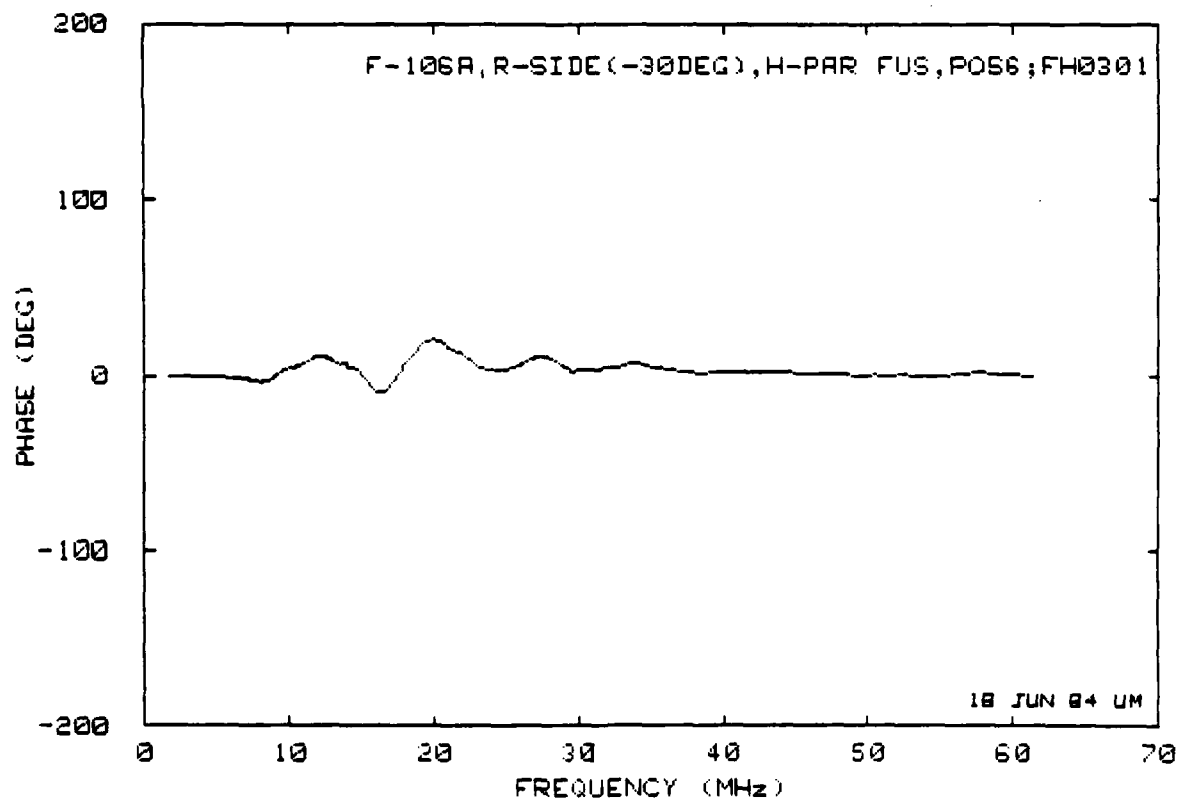
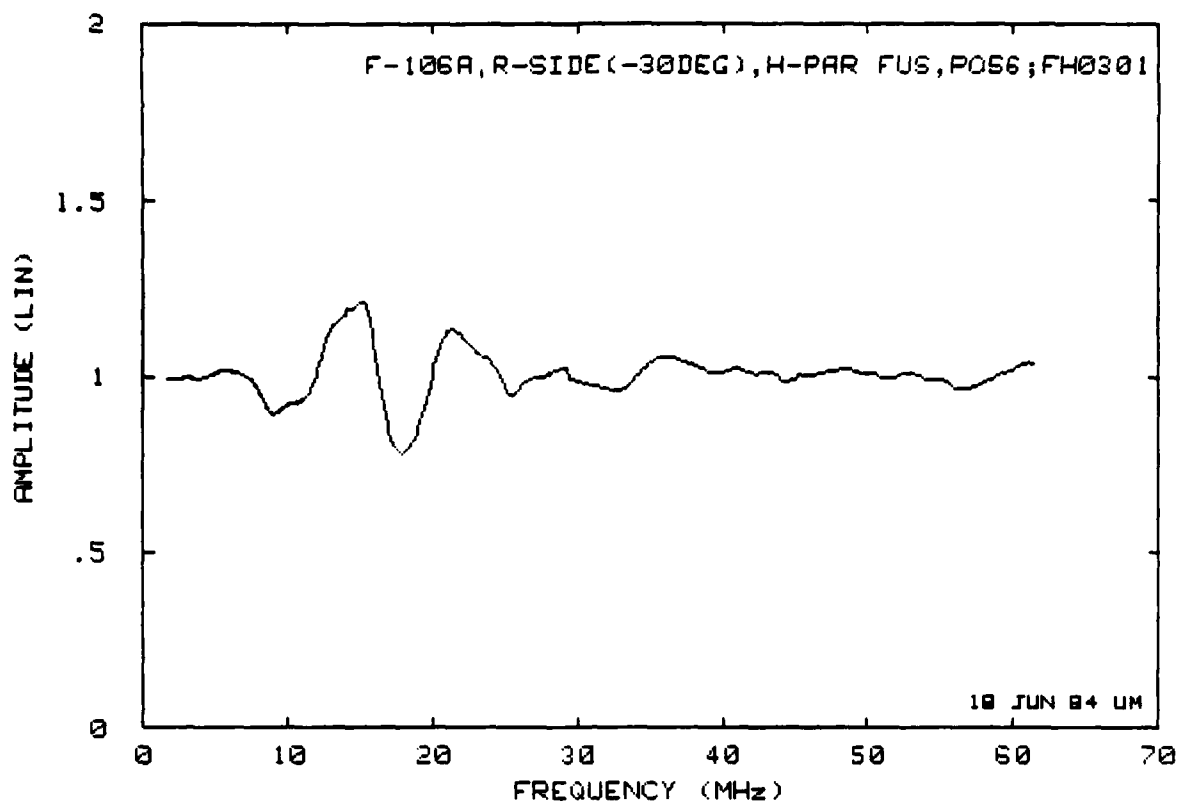
Reference file

U-F106 (unity)

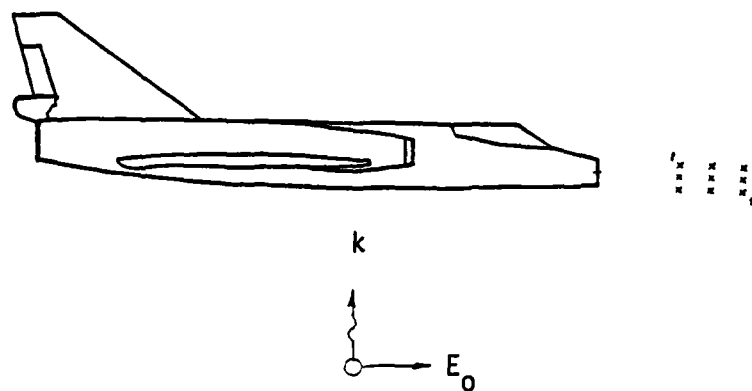
Set 4.4(a): E_1 and E_2 for right side incidence (-30 degrees),
H-parallel to fuselage.



Set 4.4(b): Normalized field at Position 4.



Set 4.4(c): Normalized field at Position 6.

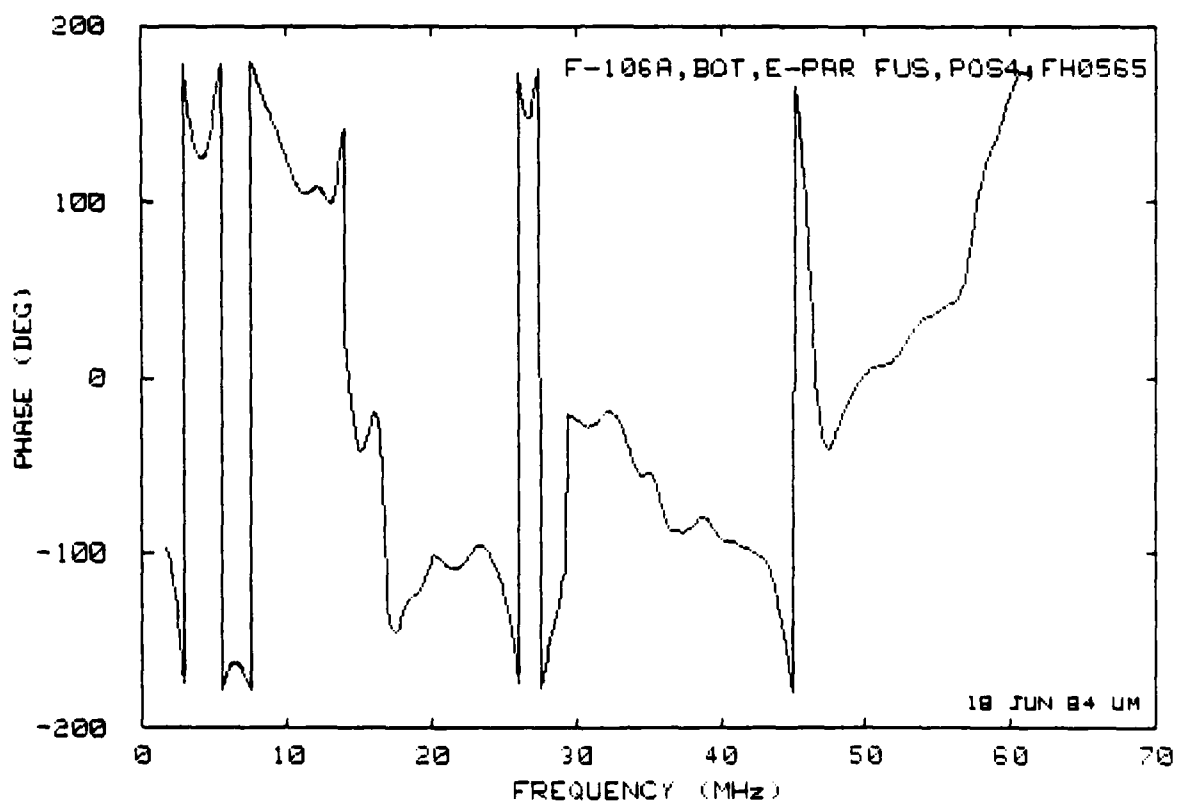
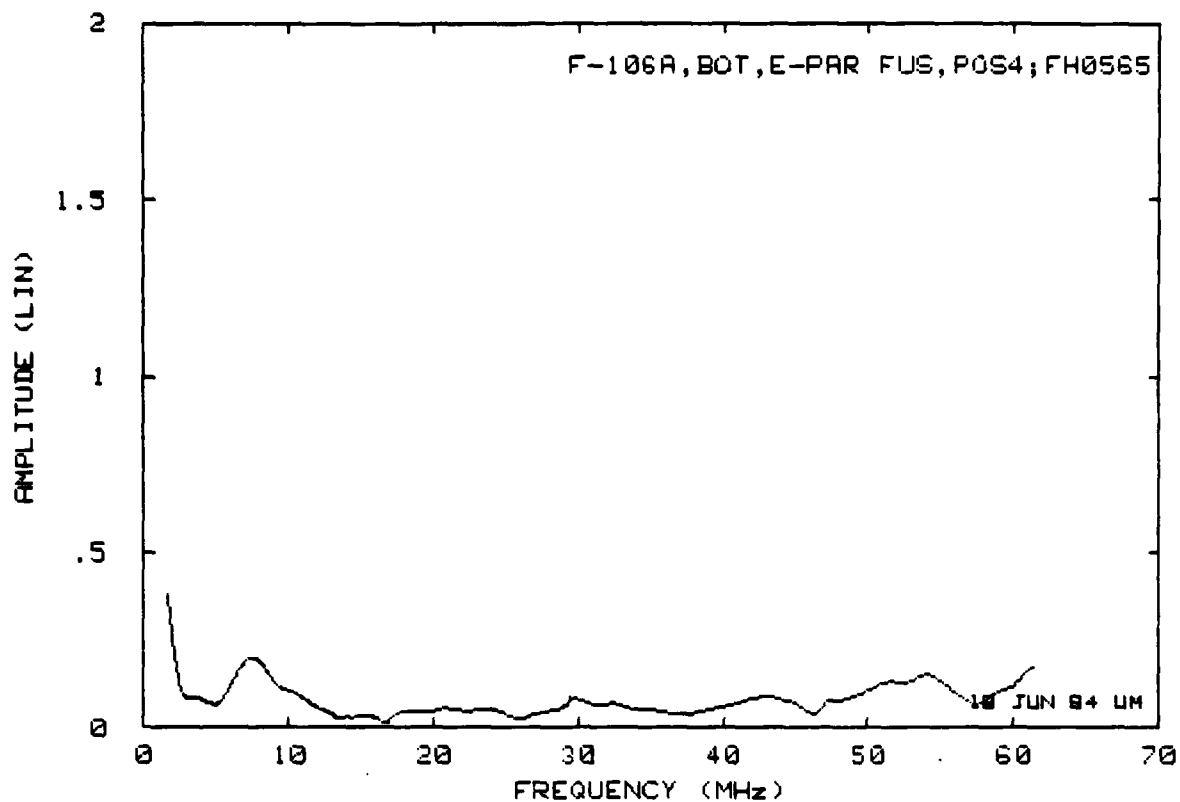


		Position	File		E_1	E_2
1	4.35	2	4.22	3	3.56	
FH0473	6.08	FH0501	6.29	FH0509	5.26	
4	6.05	5	5.16	6	2.45	
FH0565	8.02	FH0517	7.12	FH0525	3.15	
7	6.19	8	3.63	9	2.80	
FH0557	8.14	FH0541	5.32	FH0549	3.76	

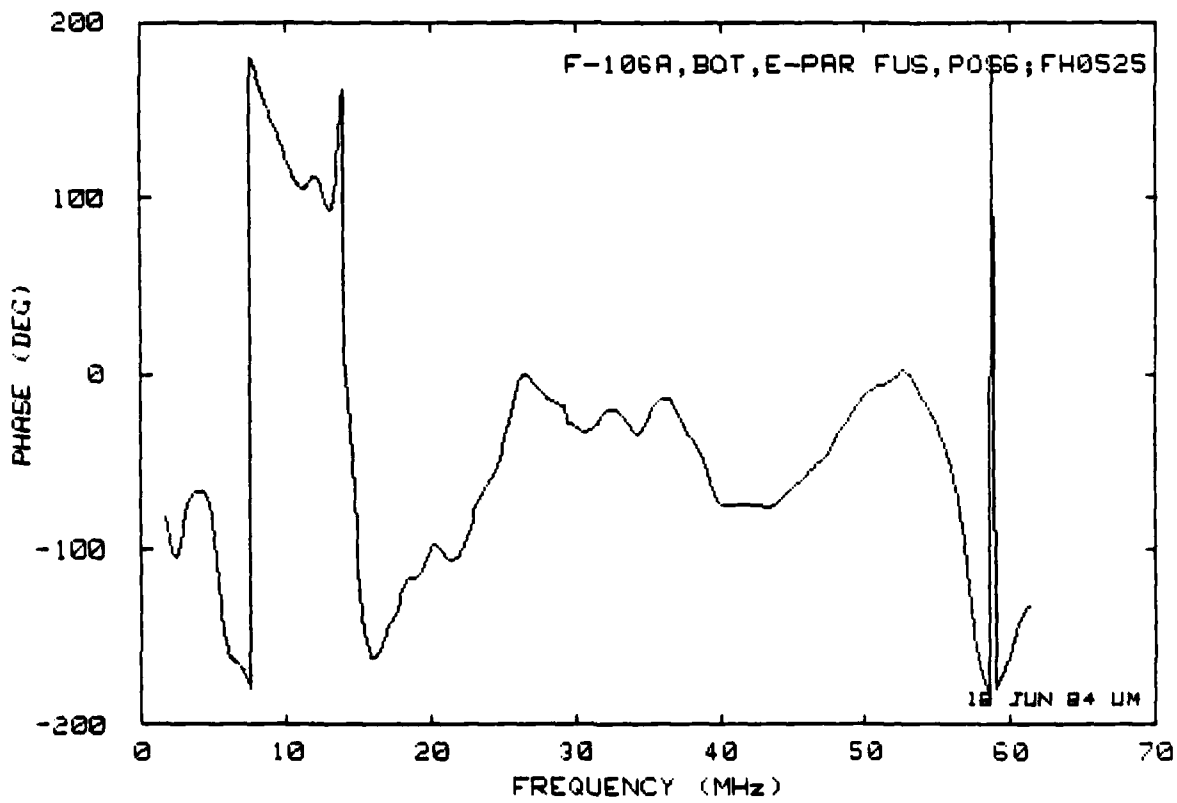
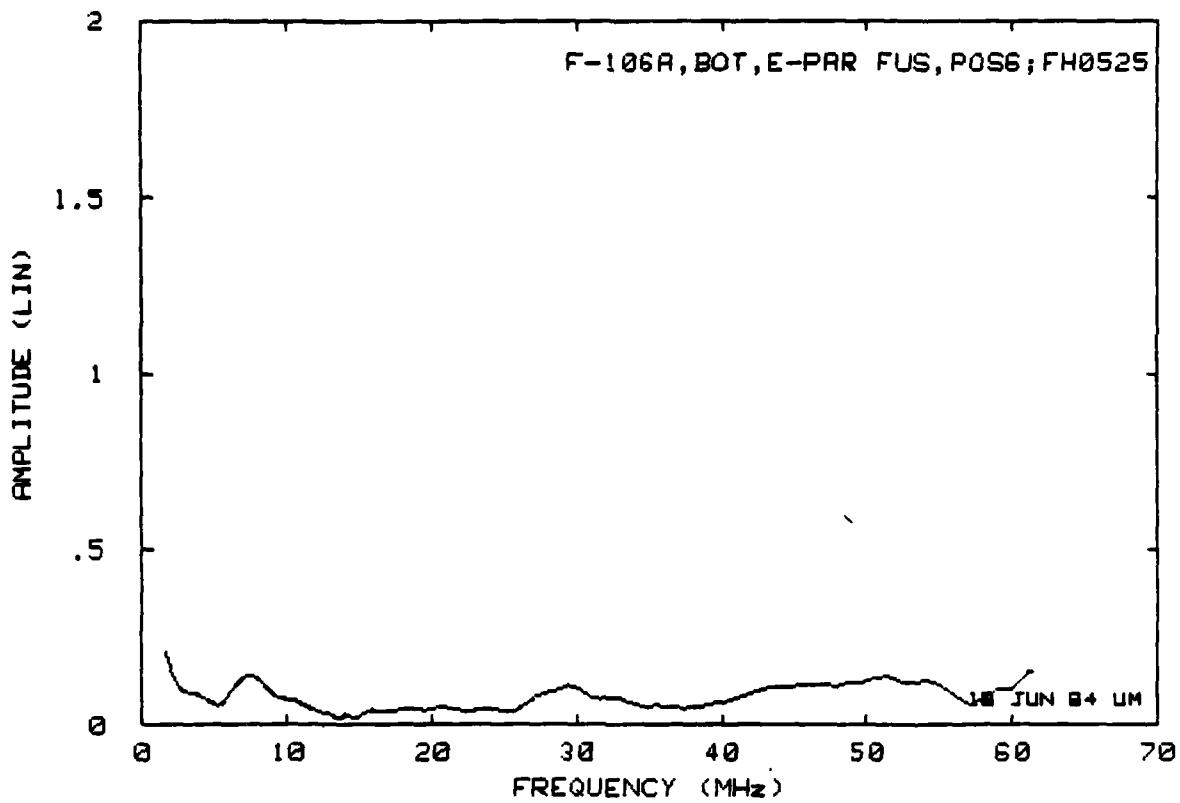
Reference file:

FH0533

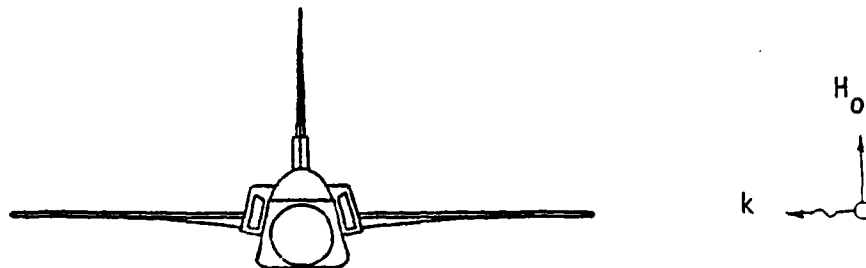
Set 4.5(a): E_1 and E_2 for bottom incidence, E-parallel to fuselage.



Set 4.5(b): Normalized field at Position 4.



Set 4.5(c): Normalized field at Position 6.

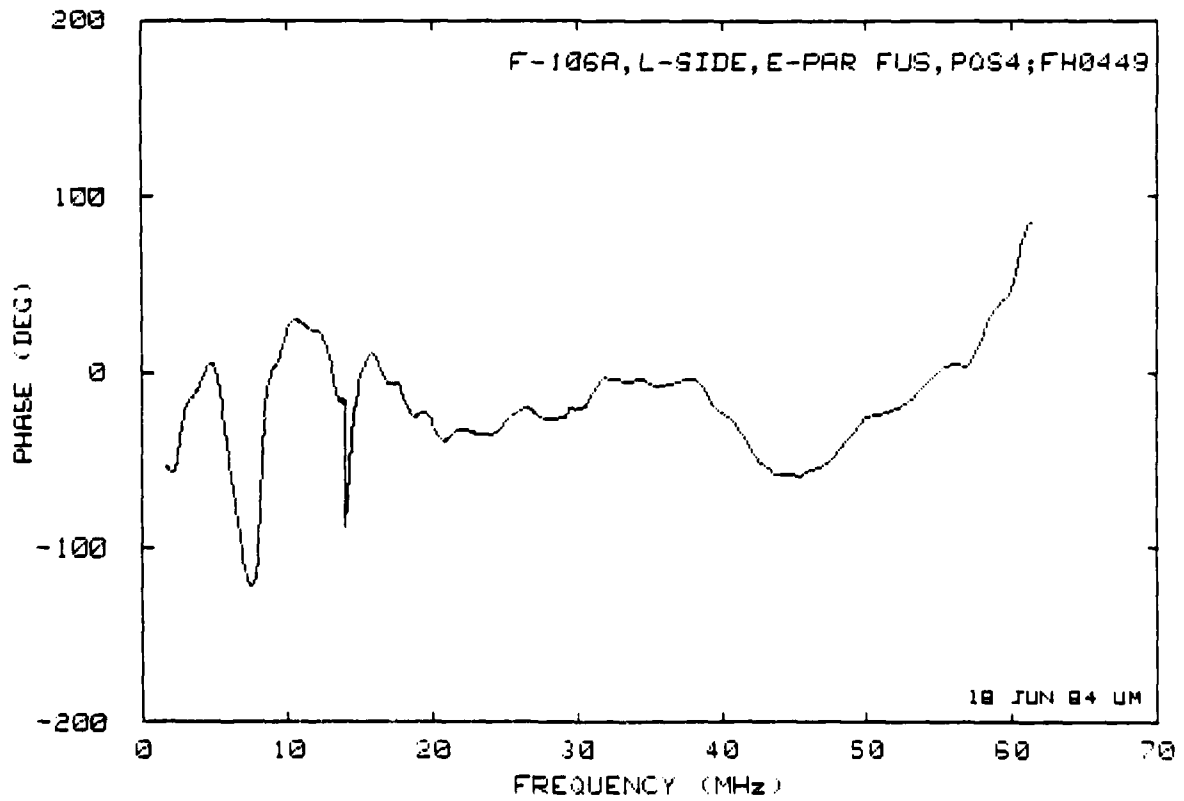
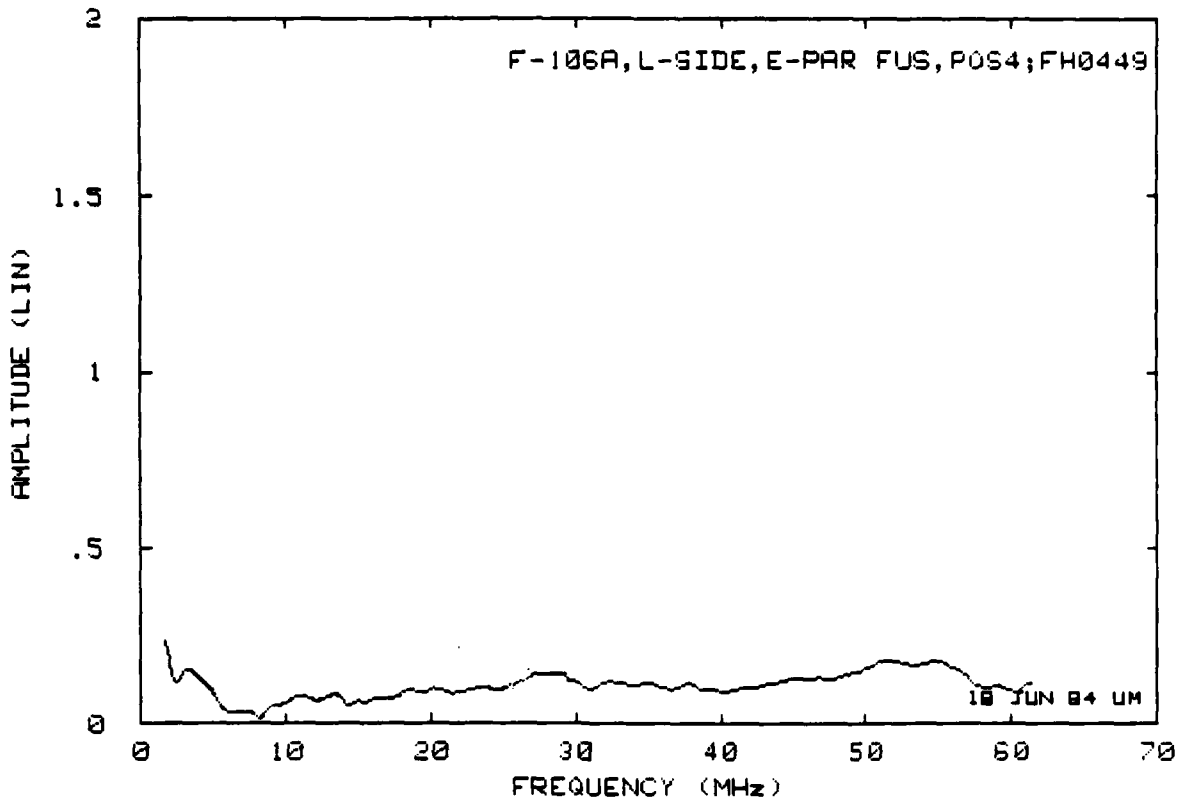


		Position		File		
1	3.46	2	2.72	3	2.23	E_1
FH0357	4.20	FH0365	3.63	FH0373	2.92	E_2
4	2.62	5	2.49	6	2.39	
FH0449	3.65	FH0401	3.43	FH0409	3.72	
7	2.96	8	2.11	9	1.95	
FH0441	3.78	FH0425	2.74	FH0433	2.54	

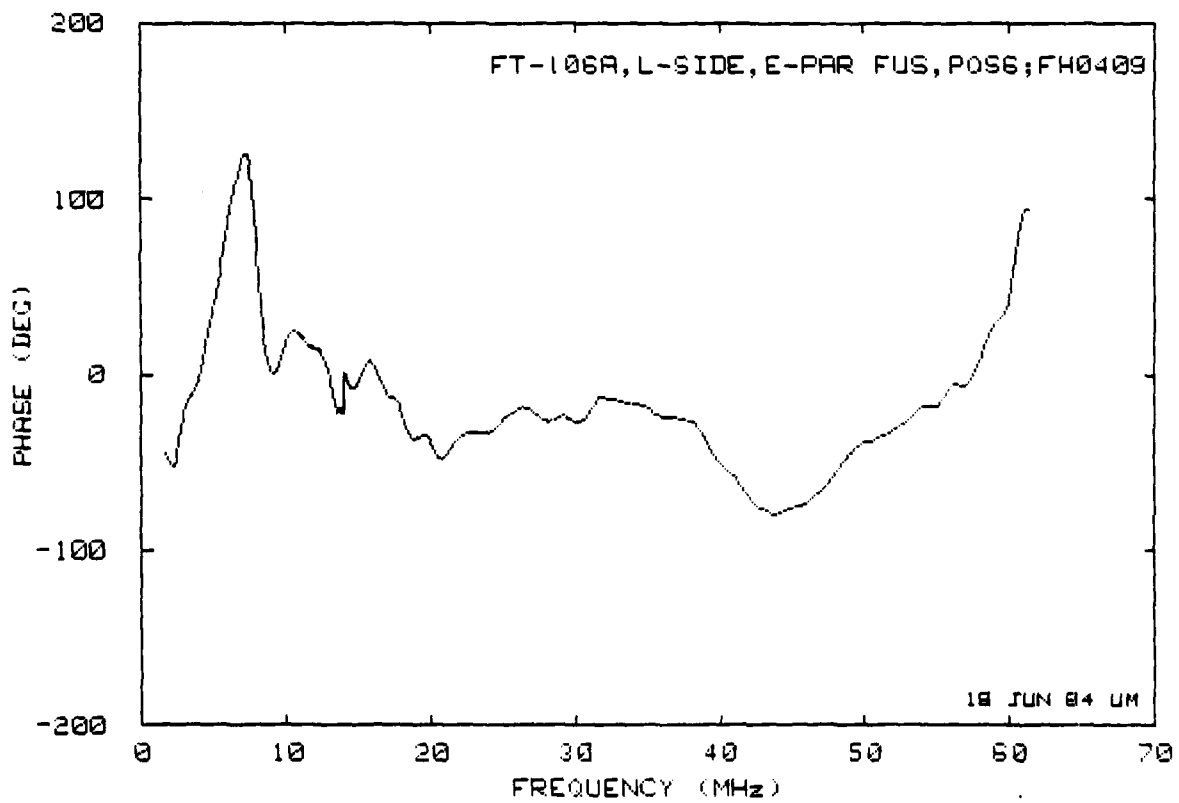
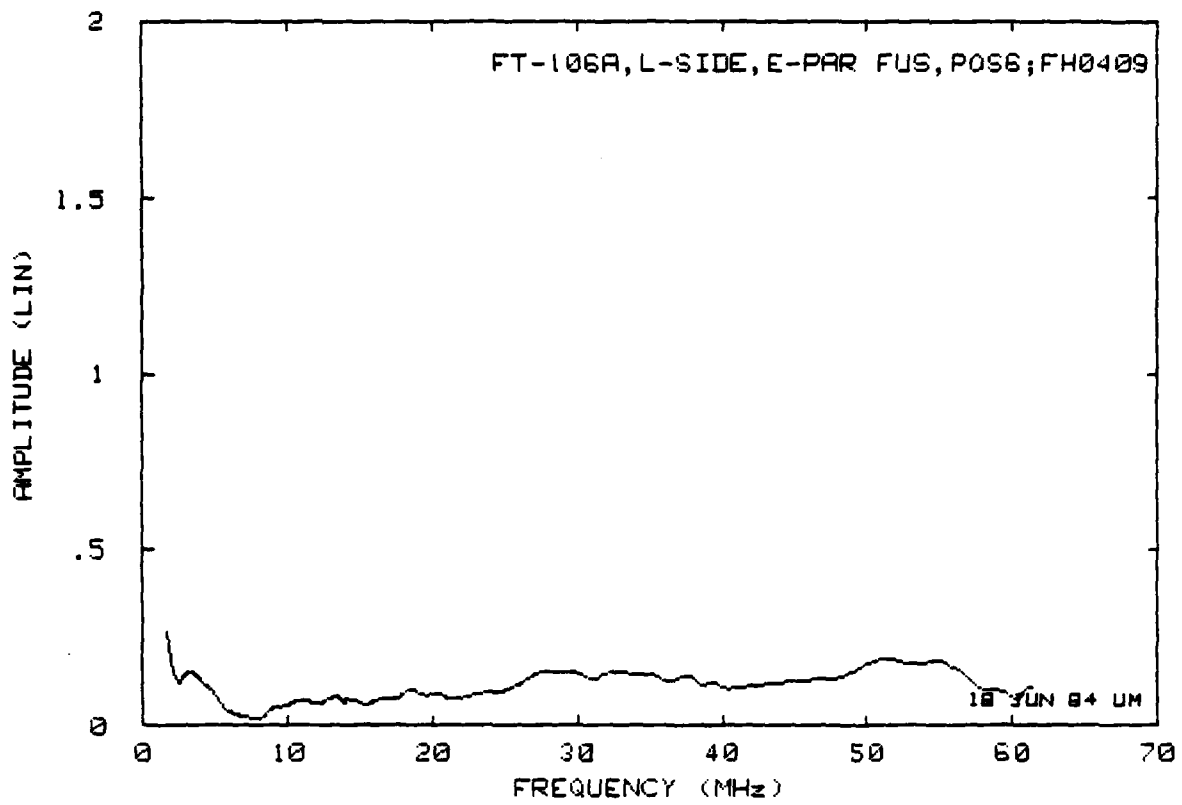
Reference File:

FH0417

Set 4.6 (a): E_1 and E_2 for left-side incidence, E-parallel to fuselage.



Set 4.6(b): Normalized field at Position 4.



Set 4.6(c): Normalized field at Position 6.

V. INTERPRETATION OF RESULTS

In Sections 3 and 4 the errors caused by the field scattered from the aircraft were deduced for each of the nine points measured in the frontal area of the aircraft for 17 different excitations that are described by direction of incidence and polarization with respect to the aircraft. Of these, 11 excitation cases came from the ground plane measurement study (Sec. 3) and six from the free space measurement study (Sec. 4). In the case of the ground plane measurements the situations simulated were Nose-on ($\theta = 180$ deg, Fig. 11), Top ($\theta = 90$ deg), Tail-n ($\theta = 0$ deg), below Tail-on ($\theta = -10$ deg), and above Tail-on ($\theta = +10$ deg). The polarization was always E-perpendicular to the fuselage. In addition, for the nose-on and top incidences, the measurements were made with the ground plane rotated to 20, 45, and 60 deg. Such rotation simulates a situation that is equivalent to two plane-waves impinging symmetrically on the opposite sides of the aircraft.

In the free space measurement study, the measurements were made for top, bottom, side, and below side incidence with E-parallel and E-perpendicular to the fuselage.

The errors caused by the scattering of the electromagnetic field from the aircraft were determined by computing the average (Eq. 1) and the RMS (Eq. 2) deviations between two signals: one measured using a loop probe with the model present (test measurement) and the other with the model removed (reference measurement).

Scanning through the computed error tables as well as the data curves themselves, one can see that the F-106 aircraft produces little scattering in the forward region. The errors follow a pattern one might expect, the largest ones being observed near the bulkhead and decreasing as one goes away, or further forward of the bulkhead. The errors also depend on the direction of arrival and the polarization of the incident signal relative to the model. They are lowest for nose-on and tail-on incidences ($E_1 \cong 1$ percent) and largest for side incidences ($E_1 \cong 3 - 7$ percent). The largest errors were observed for the case E-vertical Side-on incidence at -30 deg below horizontal. This is one of the cases that simulates situations of the VPD II/F-106 fly-by tests performed at Kirtland Air Force Base in February of 1984.

Since the errors measured were small and approach the system noise in many cases, we have found it difficult to deduce the optimum location for the sensor. The system noise can be attributed, in part, to physical changes in the chamber dimensions, possible bumping of the probe by the operator when repositioning the model, or changes in gain, frequency, etc., in the electronics during the measurement sequence. An actual study to determine these errors was not performed, but we estimate that they could affect the results by as much as ± 0.25 percent.

To determine which of the nine positions measured have the least errors we used two approaches. In the first one we simply counted the number of times the lowest three errors appeared at a given position for all the 17 measurements performed. Such a count is shown in Table 3. As can be seen, the lowest error appears seven times at position 9, four times at position 6, and three times at position 3, but because of the (estimated) 0.25 percent effect of the system noise, the ranking given in Table 3 is not necessarily meaningful.

In the next approach we looked for the minimum error sensor position by determining at each position an average error obtained by averaging over all 17 measurement situations. Positions 1, 4, and 7 which are closest to the bulkhead were not included because (1) a sensor would not normally be located there, and (2) the errors measured there are normally much higher and may erroneously bias the results. Table 4 gives a matrix of E_1 errors obtained from the data sets of Sections 3 and 4. The columns give errors at a given position for each of the 17 situations. At the bottom of each column are the average errors, and here we see that the lowest error (2.34 percent) is at position 9, second lowest (2.35 percent) at position 3, and the third lowest (2.4 percent) at position 6.

Because the error levels strongly depend on the direction and polarization of illuminating signals (see the right-hand column in Table 4 that gives the errors obtained by averaging over the six measurement positions), we then proceeded to normalize the errors such that the average for each set is 2.61, the same as the cumulative average for all positions and illumination given in Table 4. Table 5 gives the normalized data, with new averages computed for each measurement position. Now positions 3 and 6 show the minimum error (2.36

TABLE 3. MINIMUM ERROR RANKING FROM THE RAW DATA

<u>Location</u>		<u>Min Error Ranking</u>		<u>No. of Occurrences</u>	
Aircraft Bulkhead	1	2	1 - 2	3	1 - 2
			2 - 1		2 - 6
			3 - 1		3 - 6
	4	5	1 - 0	6	1 - 4
			2 - 1		2 - 5
			3 - 1		3 - 6
	7	8	1 - 1	9	1 - 7
			2 - 2		2 - 2
			3 - 0		3 - 3

TABLE 4. AVERAGES FOR ACTUAL DATA

SET	E2	E3	E5	E6	E8	E9	EAVG
3.1	1.28	1.44	1.03	1.00	1.00	1.09	1.14
3.2	2.81	2.10	2.88	1.61	3.23	1.61	2.37
3.3	0.94	1.03	0.96	1.00	1.22	1.25	1.07
3.4	4.34	3.82	4.02	3.79	3.61	3.58	3.86
3.5	3.51	3.67	4.05	4.00	4.47	4.22	3.99
3.6	1.42	1.14	1.91	1.25	1.35	1.11	1.36
3.7	0.97	0.87	0.92	0.66	1.38	0.80	0.93
3.8	0.82	0.64	0.82	0.79	1.03	0.86	0.83
3.9	1.98	1.62	1.68	1.40	2.38	1.70	1.79
3.10	1.71	1.27	2.86	2.42	2.65	1.90	2.13
3.11	2.60	2.30	2.55	2.27	2.96	2.25	2.49
4.1	1.96	1.57	2.10	1.96	2.45	2.05	2.02
4.2	1.97	1.78	1.92	1.70	2.24	1.85	1.91
4.3	4.43	3.84	4.38	3.86	4.31	3.81	4.11
4.4	11.40	7.12	7.77	8.39	8.47	6.87	8.34
4.5	4.22	3.56	5.16	2.45	3.63	2.80	3.64
4.6	2.72	2.23	2.49	2.39	2.11	1.95	2.31
AVG	2.89	2.35	2.79	2.41	2.85	2.34	2.61

TABLE 5. AVERAGES FOR NORMALIZED DATA

SET	F2	F3	F5	F6	F8	F9	FAVG
3.1	2.92	3.29	2.35	2.29	2.29	2.49	2.61
3.2	3.08	2.30	3.16	1.77	3.55	1.77	2.61
3.3	2.30	2.52	2.34	2.44	2.98	3.05	2.61
3.4	2.93	2.58	2.71	2.56	2.44	2.42	2.61
3.5	2.29	2.40	2.65	2.61	2.92	2.76	2.61
3.6	2.71	2.18	3.65	2.39	2.58	2.12	2.61
3.7	2.71	2.43	2.57	1.84	3.85	2.23	2.61
3.8	2.58	2.02	2.58	2.49	3.25	2.71	2.61
3.9	2.88	2.35	2.44	2.03	3.46	2.47	2.61
3.10	2.09	1.55	3.49	2.95	3.23	2.32	2.61
3.11	2.72	2.41	2.67	2.38	3.10	2.36	2.61
4.1	2.53	2.03	2.71	2.53	3.17	2.65	2.61
4.2	2.69	2.43	2.62	2.32	3.06	2.52	2.61
4.3	2.81	2.44	2.78	2.45	2.74	2.42	2.61
4.4	3.56	2.22	2.43	2.62	2.65	2.15	2.61
4.5	3.02	2.55	3.70	1.75	2.60	2.01	2.61
4.6	3.06	2.51	2.80	2.69	2.37	2.19	2.61
AVG	2.76	2.36	2.80	2.36	2.96	2.39	2.61

percent) and the positions 9 is the third lowest (2.39 percent). Results of this analysis support the theoretical expectation by Giri and Baum (Ref.4) which says that the minimum errors should be expected at position 3.

VI. CONCLUSIONS AND RECOMMENDATIONS

The study has shown that the errors caused by the scattering from the F-106 aircraft are for all practical purposes negligible when the B-dot sensor is placed 2.7 m or further ahead of the bulkhead. Because of smallness of the aircraft scattering, the presence of measurement noise caused by reflections from the chamber, equipment drifts, etc., made it difficult to clearly predict the optimum location of the sensor. More analyses on the data taken could be carried out using, for example, only the excitations (polarizations and directions of incidence) appropriate for specific lightning situations.

The errors should also be assessed in the time domain for a specified class of pulse shapes. Since the measured frequency domain data are already in digital form, such analyses would not be difficult and could be carried out by first multiplying the (measured) transfer functions by the provided pulse (lightning) spectrum and then transforming to the time domain. A more realistic error value, such as an error in the peak value of the field measured by the sensor, could thus be obtained.

APPENDIX A

SEM STUDIES ON THE F-106

1. INTRODUCTION

The singularity expansion method as applied to electromagnetic scattering is a method of characterizing the response of a target in terms of transfer function parameters such as poles and residues. To this end, the poles are assumed to be invariant, while the residues vary with the particular measurement performed and the type (including direction and polarization) of illumination. At least in theory, the accurate location of a few poles could assist in determining the identity of the target, but in practice the supposedly invariant poles tend to move about with changes in the target's orientation and illumination. If the noise and clutter are nondeterministic, and if it is feasible to repeat the measurement, both the noise and clutter can be reduced by repeating the measurement several times and averaging the associated signals. If the usual assumptions about the noise and clutter (such as distributions which have zero mean and are independently and identically distributed) are satisfied, combining K measurements will result in an increase in the signal-to-noise ratio by a factor of K . By taking K sufficiently large, the data may be quieted enough to guarantee accurate pole and residue extraction. Of course, in practice, obtaining a large number, K , of measurements, may be somewhat expensive, or in some situations, impossible. For example, if measurements are made of a moving target such as an airplane, the requirement that the measurement be repeatable can be satisfied approximately at best, and then only for a limited amount of time. Conversely, if the measurement of a stationary object is repeated, any stray reflections from other stationary objects (or, in the case of near-field measurements, probe-target interaction) will be repeated exactly. Under these circumstances, the clutter is deterministic and the energy associated with the clutter cannot be reduced by repeating and averaging the measurements. On the other hand, if the noise and clutter are nondeterministic, the signal-to-noise ratio will increase as additional data sets are incorporated into the composite data set. It is therefore desirable to include not only similar measurements, which may be combined using strict waveform averaging, but also those associated with different illuminations of the target.

This Appendix presents an extension of measurement averaging that eliminates the requirement of identical measurements and thus permits further increases in signal-to-noise ratio by increasing the number of data sets which may be properly combined. A discussion of the accuracy of this method is given in Ksienski (Ref. A1)

2. FORMULATION

Using the standard pole residue expansion, the data as a function of the circular frequency ω may be represented as

$$F_k(j\omega) = \sum_{m=1}^M \frac{a_{km}}{j\omega - s_m} + N_k(j\omega) \quad (A1)$$

where k is an index to the various measurements and $N_k(j\omega)$ represents noise and clutter. We wish to combine K such data sets in a manner so as to have a maximum signal-to-noise ratio in the composite data set. Assuming a linear combination with arbitrary complex weighting coefficients, the composite data set is

$$E_{\text{comp}}(j\omega) = \sum_{k=1}^K w_k F_k = \sum_{k=1}^K w_k \left(\sum_{m=1}^M \frac{a_{km}}{j\omega - s_m} + N_k(j\omega) \right) \quad (A2)$$

and by interchanging the order of summation and noting the invariance of the poles s_m with measurement number k ,

$$F_{\text{comp}}(j\omega) = \sum_{m=1}^M \frac{b_m}{j\omega - s_m} + N(j\omega) \quad (A3)$$

where

$$b_m = \sum_{k=1}^K w_k a_{km} \quad (A4)$$

In general, it will only be possible to maximize one b_m at a time. This is because for different choices of m the a_{km} will not vary in unison with k . Thus, the increased signal-to-noise ratio, and hence increased accuracy, will only be obtained for the pole s_m . However, since the specification of the pole is arbitrary, several poles may be obtained through successively emphasizing different b_m . For the present, we restrict ourselves to obtaining an improved estimate of s_1 , which necessitates maximizing $|b_1|^2$. From (Eq. A4), we may write

$$|b_1|^2 = |w^T a|^2 \quad (A5)$$

where $w = [w_1, w_2, \dots, w_K]^T$ and $a = [a_{11}, a_{21}, \dots, a_{K1}]^T$. Without loss in generality, the weighting vector may be constrained to $\bar{w}^T w = 1$. Then, noting the dot product formulation of (Eq. A5) the maximum b_1 will occur for

$$w = \frac{\bar{a}}{|a|} \quad (A6)$$

and for this optimal choice of the weighting vector, $|b_1|^2 = ||a||^2$. To evaluate the energy associated with the noise $N(j\omega)$, we take the expectation of the noise squared

$$\begin{aligned} E|N(j\omega)|^2 &= E \left| \sum_{k=1}^K w_k N_k(j\omega) \right|^2 \\ &= \sum_{k=1}^K E |w_k N_k(j\omega)|^2 \end{aligned}$$

and assuming the variance of the noise is equal to σ^2 in each of the original measurements,

$$E|N(j\omega)|^2 = \sigma^2 \sum_{k=1}^K |w_k|^2 = \sigma^2$$

Thus the energy associated with the noise will not increase with w normalized as in (Eq. A6). If K data sets are combined each containing an approximately equal excitation of the mode associated with the desired pole, the signal-to-noise ratio will increase by a factor of K . For any set of residues, the resulting weighting coefficients will produce the maximum possible increase in signal-to-noise ratio.

3. IMPLEMENTATION

The formulation assumes initial estimates of residues in order to compute the weighting coefficients. The algorithm is fairly insensitive to errors in these estimates of the residues and, in fact, a single complex error factor

associated with all of the residues will not adversely affect the weighting vector. The effect of variations in the real part of the pole is minimized by normalizing the residues by the real part of the associated poles, i.e., (Eq. 6) is used with a redefined as

$$a = \left[\frac{a_{11}}{\operatorname{Re}(s_{11})}, \frac{a_{21}}{\operatorname{Re}(s_{21})}, \dots, \frac{a_{K1}}{\operatorname{Re}(s_{K1})} \right]^T \quad (A7)$$

where s_{i1} refers to the estimate of the pole s_1 obtained from the i th data set. After the composite data set is formed, it must be subjected to a pole and residue extraction procedure. The algorithm due to Levy (Ref. A2) and Sanathanan and Koerner (Ref. A3) assumes that the poles and residues exhibit conjugate symmetry. This is generally appropriate as it is equivalent to requiring the frequency data to correspond to a real function of time. The $F_{\text{comp}}(j\omega)$ does not have conjugate symmetry. Recently, Tao and Zunde (Ref. A4) extended the method of Levy (Ref. A2) to distributions of poles and zeroes which have no symmetry constraints. Although the algorithm of Tao and Zunde does accommodate the data set, it is somewhat more general than required. Specifically, it does not require the poles to occur in conjugate pairs, but as may be seen from (Eq. A2), $F_{\text{comp}}(j\omega)$ does preserve the conjugate symmetry of the pole pairs. To more closely match the known parametrization of the data, an algorithm was produced which relaxes the conjugate symmetry constraint on the residues while maintaining the conjugate symmetry constraint on the poles, and the derivation is given in Ksienski (Ref. A1).

The implementation of the algorithm requires negative frequency information which is obtained from the original data sets by employing conjugate symmetry. After the accuracy of the pole location is improved, the next step is to refer the residues to the new pole estimate. Constraining a pole to a particular location is not an easy task (Pond and Senior, Ref. A5), but the present algorithm provides a simple alternative. Since an original data set corresponds to a real function of time, it is an even function of frequency. A second set of data which is an odd function of frequency may be added to the original data and the sum expanded as a series of poles. Noting that the poles are constrained to occur in conjugate pairs, the component of the summation associated with the original data may be obtained by retaining the even part of the residues. Both the original data and the second set are

constrained to have the same poles in the expansion and, by appropriate placement of the poles associated with the second set of data, it is possible to constrain the pole locations in the expansion of the original data. The residues are then obtained relative to these new constrained pole locations without any apparent adverse side effects. An additional advantage is that the accuracy of the location of the adjacent pole is also improved.

4. RESULTS

It was desired to extract the two poles associated with the fuselage and wing resonances. Casual inspection of the data indicated that these poles would have imaginary parts of approximately 6 and 14 MHz, respectively. The algorithm described above was applied to 14 data sets (Liepa and Pennock, Ref. A6) which were selected as having relatively large components associated with the desired poles. The data sets used were FT1476, FT1517, FT1601, FT1840, FT1919, FT1809, FT1801, FT1765, FT2465, FT2433, FT2372, FT1757, FT1617, and FT1309. Figures A1 through A4 show plots of these data. The poles and residues which were extracted are listed in Table A1.

From Reference A.6 are presented here Tables A2, A3 and Figure A5 that identify each data set with measurement situations.

AD-A172 032

NOSE BOOM B-DOT SENSOR LOCATION OPTIMIZATION FOR NASA
F-106(U) DIKEMOOD ALBUQUERQUE NM V V LIEPA ET AL
JUN 85 DC-FR-1026.330-4A AFWL-TR-85-94 F29601-82-C-0027

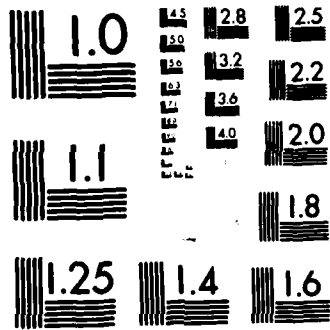
2/2

UNCLASSIFIED

F/G 1/3

NL





MICROCOPY RESOLUTION TEST CHART
NATIONAL BUREAU OF STANDARDS-1963-A

TABLE A1. POLES AND RESIDUES FOR NASA F-106 AIRCRAFT

Poles Residue	-1.272+j6.457	-1.459+j14.45	-2.609+j28.66
FT1465	-1.291-j.2784	4.153-j2.302	1.665-j5.149
FT1309	-.2562+j.07608	1.805-j.6113	-.2235+j.09827
FT1517	-.1430+j.1857	-.4043+j.5228	-.4470-j.3472
FT1601	-1.163+j4.238	.7896-j.5094	-.3829+j.2955
FT1617	-21166+j3.795	-3.656-j2.854	-2.422-j.1126
FT1757	-9.230+j18.22	1.214-j1.829	-9.374+j4.474
FT1765	-3.907-j8.879	-.2404+j.02450	-1.716-j7.743
FT1801	-6.985+j2.436	2.552+j1.544	-3.542+j9.433
FT1809	4.911-j20.30	.5698+j.8693	1.887-j4.021
FT1849	-.1381+j.2256	-.04788+j.09923	.4091+j1.193
FT1917	-2.084-j1.449	.1096+j.3168	1.280+j.4045
FT2373	-.01067+j.07738	-.03776-j.1230	1.074-j2.020
FT2433	3.453+j1.439	.8615+j.2169	2.048-j1.450
FT2465	3.126+j1.938	.6381-j.2114	2.608+j2.124

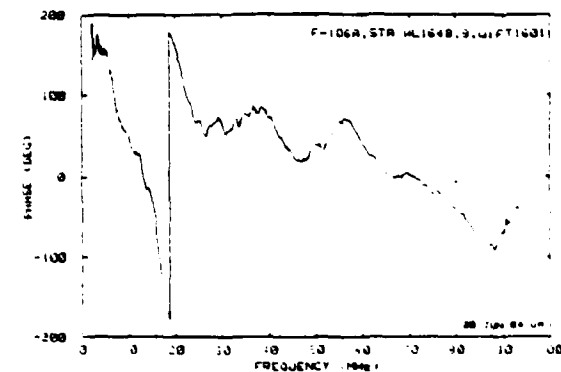
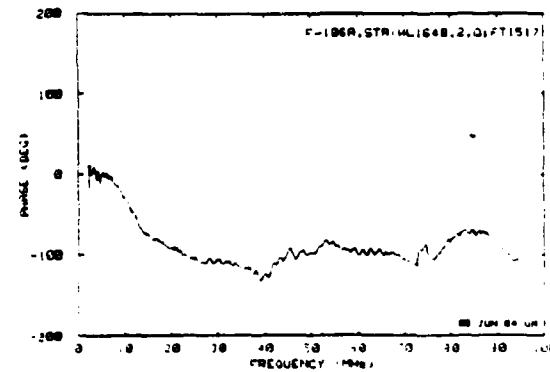
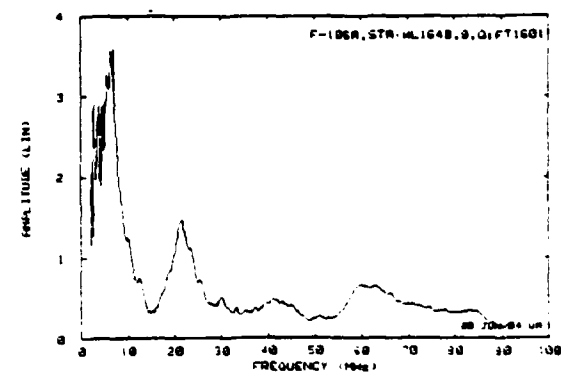
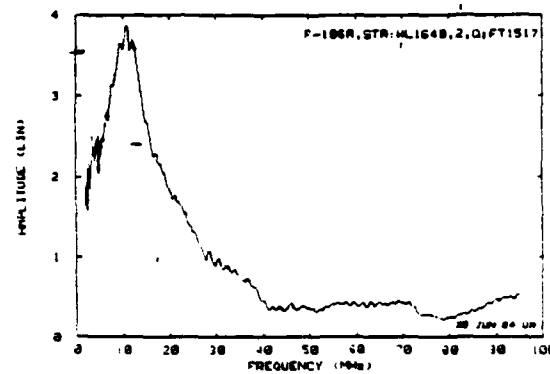
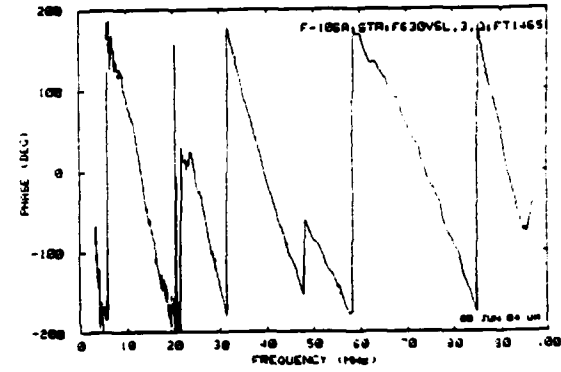
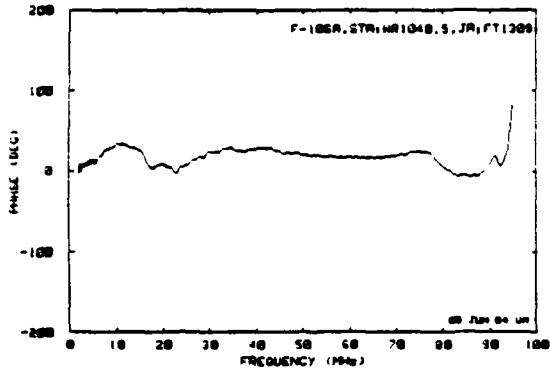
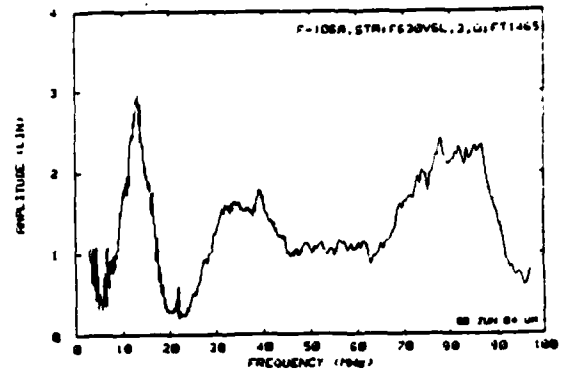
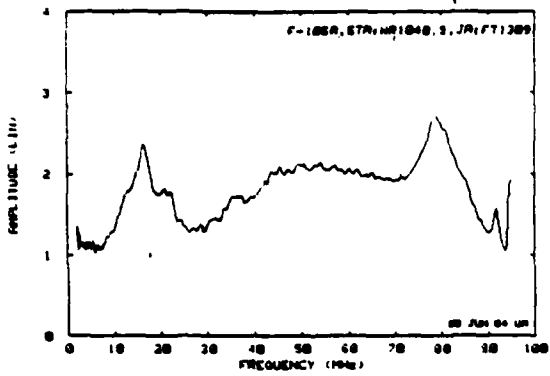


Figure A1. Data sets FT1309, FT1465, FT1517, and FT1601.

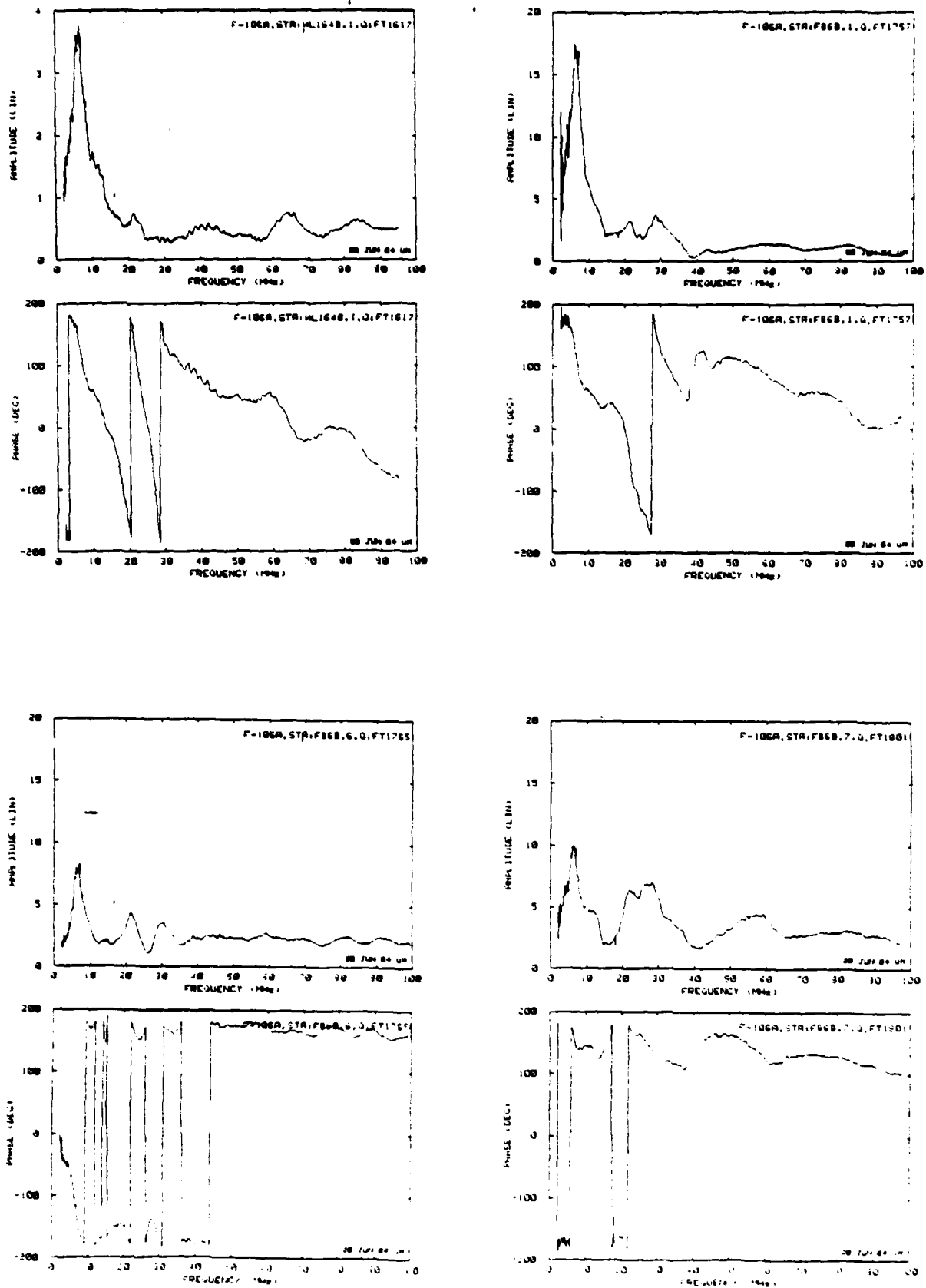


Figure A2. Data sets FT1617, FT1757, FT1765, and FT1801.

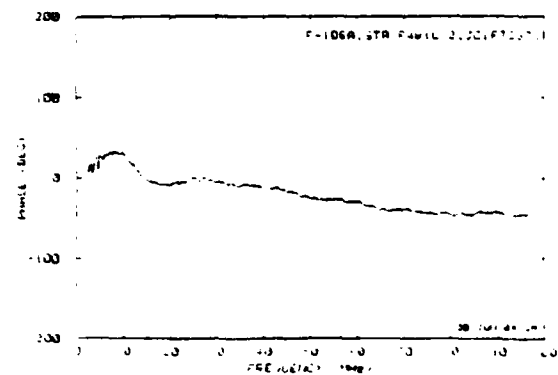
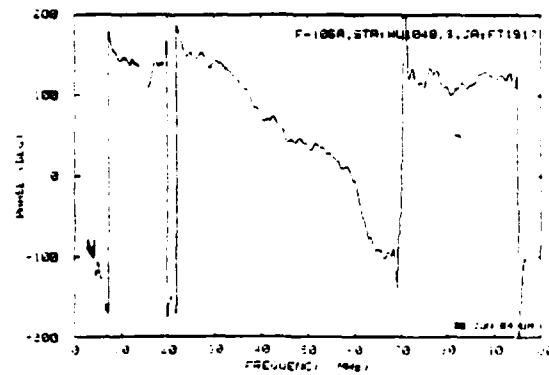
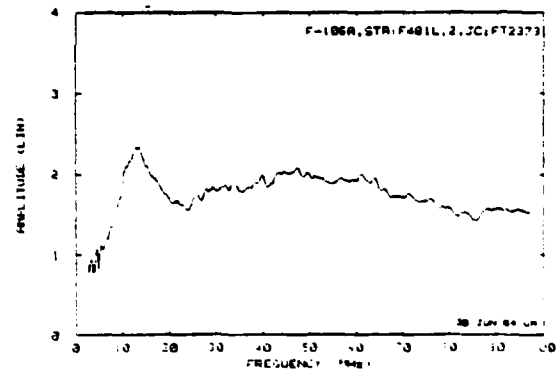
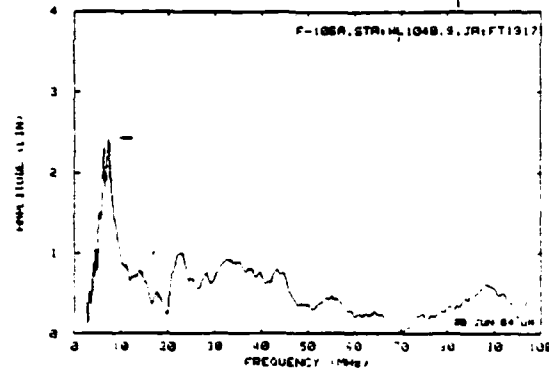
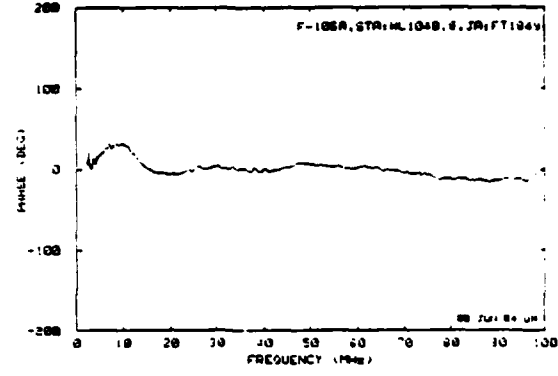
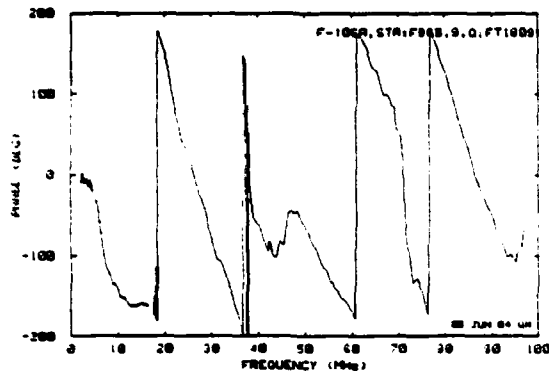
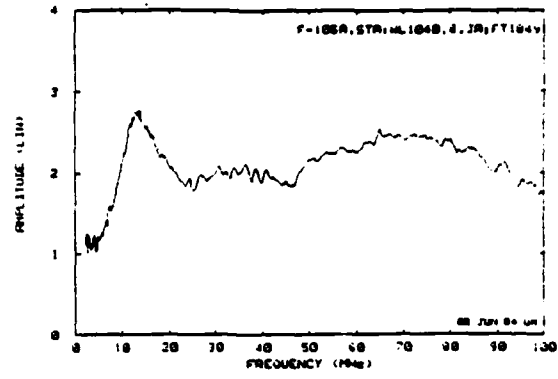
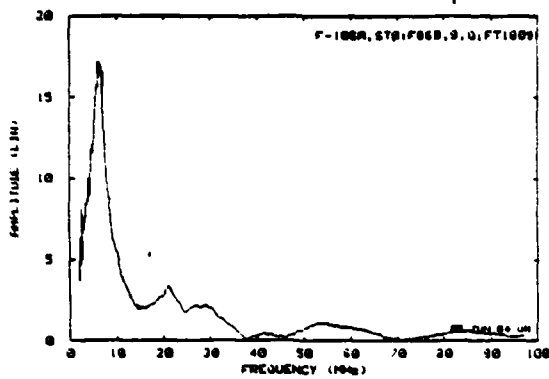


Figure A3. Data sets FT1809, FT1849, FT1917, and FT2373.

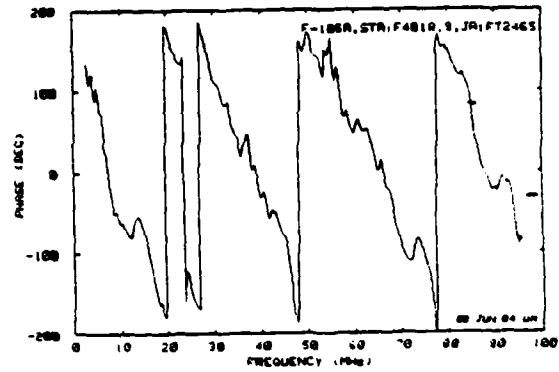
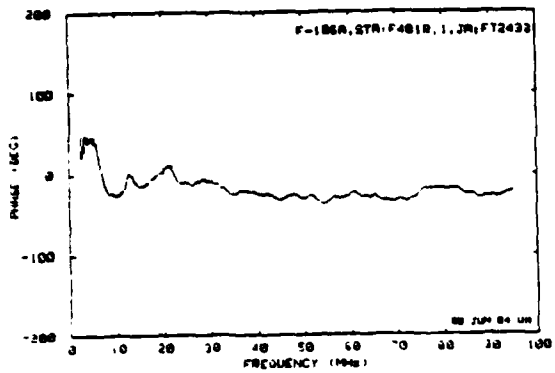
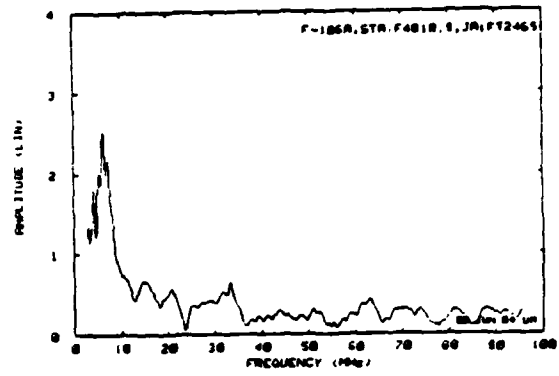
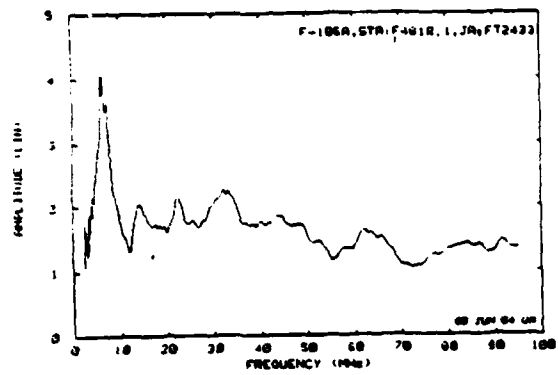


Figure A4. Data sets FT2433 and FT2465.

TABLE A2. MEASUREMENT MATRIX

Orientation Station	1	2	3	4	5	6	7	8	9
F86B Q	FX1757		FX1773	FX1817	FX1825	FX1765	FX1801		FX1809
F481L JC	FX2325	FX2373	FX2341	FX2401	FX2409	FX2333	FX2349	FX2365	FX2357
F481R JA	FX2433	FX2501	FX2449	FX2509	FX2517	FX2441	FX2457	FX2473	FX2465
VS630L Q		FX1409	FX1465	FX1417	FX1425	FX1433			
WL104B JA	FX1925	FX1857	FX1949	FX1865	FX1873	FX1933	FX1941	FX1849 ³	FX1917
WL164B Q	FX1617	FX1517	FX1609	FX1525	FX1533	FX1565	FX1573		FX160i
WR104B JA					FX1309				

- (1) Average of FT1441 and FT1465
- (2) Average of FT1549 and FT1573
- (3) Average of FT1265 and FT1849

TABLE A3. F-106 MEASUREMENT STATIONS

Station	Sensor Location	Measurement	Sensor Location Boundaries
F66B	Panel on bottom of forward fuselage	Q	On centerline, between STA:77.00 and STA:94.76
F431L	Panel on upper fuselage, port side	JC	Between STA:472.00 and STA:487.80
F481R	Panel on upper fuselage, starboard side	JA	Between STA:472.00 and STA:487.80
V5650L	Panel on port side of vertical stabilizer	Q	Between STA:614.80 and STA:645.28, above WL34.70, through WL49.50
WL104B	Panel on bottom of port wing	JA	Between STA:431.00 and STA:472.00 between BL160.44 and BL107.50
WL164B	Panel on bottom of port wing	Q	Between STA:556.75 and STA:593.46, between BL160.44 and BL167.94
WR104B	Panel on bottom of starboard wing	JA	Between STA:431.00 and STA:472.00 between BL99.94 and BL107.50
WR164B	Panel on bottom of starboard wing	Q	Between STA:445.75 and STA:593.46, between BL160.44 and BL167.94

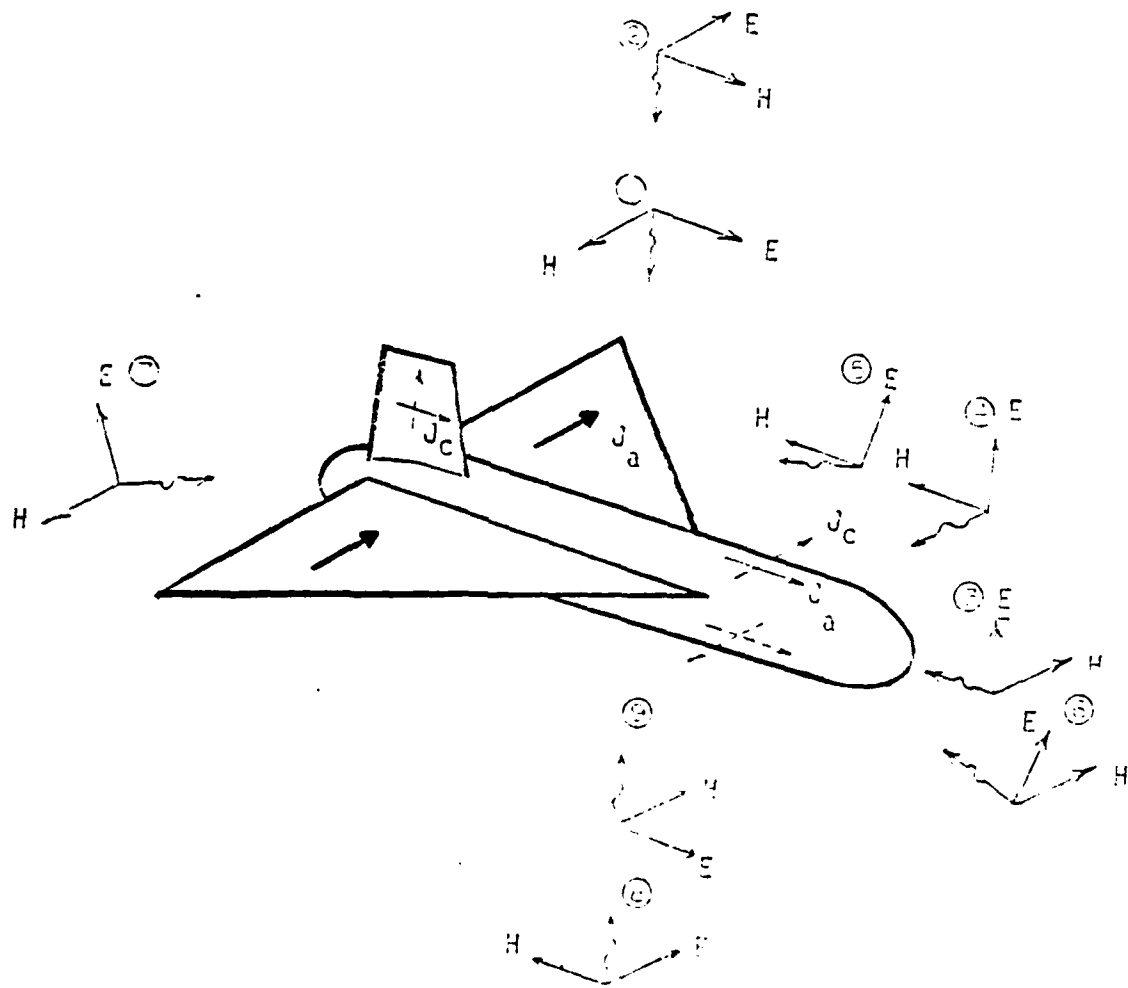


Figure A5. Excitation Field and Surface Current Directions on the Mode 1.

REFERENCES

APPENDIX A

- A1. Ksienski, D.A. (1984), Pole and Residue Extraction from Measured Data in the Frequency Domain Using Multiple Data Sets, submitted to Radio Science.
- A2. Levy, E.C. (1959), "Complex Curve Fitting, IRE Trans. on Automatic Control," IEEE Trans., Vol. AC-4, pp. 37-44.
- A3. Sanathanan, C.K. and J. Koerner (1963), "Transfer Function Synthesis as a Ratio of Two Complex Polynomials," IEEE Trans., Vol. AC-8, pp. 56-58.
- A4. Tao, K.M. and P. Zunde (1981), "On Levy's Identification, Its Generalization and Applications," Int. J. Sys. Science, Vol. 12, No. 11, pp. 1317-1334.
- A5. Pond, J.M. and T.B.A. Senior (1982), "Determination of SEM Poles from Frequency Responses," Electromagnetics, Vol. 2, pp. 55-67.
- A6. Leipa, V.V. and Steven T. Pennock, "Exterior Electromagnetic Response of the NASA F-106 Aircraft," University of Michigan Radiation Laboratory Report 021155-1-F, AFWL Interaction Application Memo 41, June 1984.

APPENDIX B

LIGHTNING SIMULATION STUDIES

Recent measurements of the electric and magnetic fields of lightning processes reveal that the fields can vary on a submicrosecond time scale. The rapid variation of the electromagnetic fields implies that the currents involved in a lightning discharge also can vary on a submicrosecond scale (Refs. B1, B4, B3). Airborne measurements have directly confirmed that cloud discharge processes can have submicrosecond current rise times (Refs. B1, B5, B2).

Lightning processes with submicrosecond current and field rise times are a hazard to aircraft because aircraft resonances can be efficiently excited. Direct lightning strikes, as well as near misses, can excite resonances which pose a threat, especially to newer aircraft. The increased use of nonmetallic structural materials has reduced the electromagnetic shielding of the interior of the aircraft, making flight-critical low-voltage digital electronics susceptible to interference or damage (Ref. B6).

An aircraft in flight can become attached to a lightning channel by initiating discharges which connect to the stepped leader or to any other phase of the discharge in which there is a propagating channel. In addition, an aircraft can cause a lightning discharge which would not have occurred if the aircraft had not been there. The lightning discharge is triggered by field enhancement caused by the presence of the aircraft in a region where the electromagnetic field is already high, resulting in the generation and propagation of leaders in two directions away from the aircraft toward regions of opposite charge. Charge on the aircraft due to precipitation interactions can increase the probability of a lightning strike. Charge deposited in the wake of the aircraft due to precipitation charging can guide the lightning to the plane or shield the plane from it. An extensive discussion of the lightning-aircraft interaction is given in the paper by Clifford and Kasemir (Ref. B7).

The attachment of a typical lightning discharge to an aircraft in flight, as described in the paper by Uman and Krider, happen as follows: "A lightning leader with a typical charge density of 10^{-3} c/m approaches the aircraft at a velocity of 10^5 to 10^6 m/s. When the fields on the wings, nose, tail, and

other extremities exceed a critical value, corona will begin and outward-going discharges will be initiated. These discharges will lower the electric field at the surfaces of the plane because of shielding. The 'striking distance' is determined by the distance to the incoming leader at the time when the aircraft initiates the outward-going discharges. The time for the leader and connecting discharge to join is probably of the order to $10 \mu\text{s}$, and the striking distance is probably of the order of a plane length. When contact takes place, the aircraft will be raised to the 10^8 to 10^9 V potential of the lightning channel in a characteristic charging time determined by the channel surge impedance, roughly 1000Ω , and the aircraft capacitance 10^{-9} to 10^{-10} F . Thus the charging time will be 10^{-7} to 10^{-6} s, and the rate of change of the aircraft voltage will be 10^8 to 10^{10} V/ μs . Contact will also cause the electrical field at the surface of the plane to reverse direction, and the aircraft may produce additional corona and leaders. In any event, the leader current will propagate through the aircraft in a relatively steady fashion, and then there may be superimposed fast current pulses due to leader steps, K-changes, return strokes, or any other impulsive lightning process." (Ref. B6).

The purpose of this investigation was to investigate methods of analyzing and simulating in the laboratory a direct lightning strike on an aircraft in the frequency domain. The description of the lightning attachment process and the presence of submicrosecond components in lightning currents and fields suggest that the primary effect of a lightning attachment to an aircraft in the frequency domain would be to excite and modify natural aircraft resonances and possibly produce new resonances associated with the attachment of the highly conducting lightning channel.

The natural resonant frequencies of an aircraft can be evaluated experimentally by illuminating a scale-model of the aircraft in an anechoic chamber with a plane wave of appropriately scaled frequency and measuring the surface currents induced on the model. We felt that the effect of a lightning attachment on the natural resonant frequencies of an aircraft could be evaluated experimentally by attaching a structure simulating the lightning channel to the scale model of the aircraft, placing the model in the chamber and measuring the surface currents induced on the surface of the model airplane when it is illuminated by a plane wave.

Our primary task thus lay in choosing an appropriate lightning model and finding a structure (a wire, lossy string, etc.) which would accurately represent the lightning model in the measurement frequency range. The structure attached to the aircraft scale-model could then be used to investigate the effect of lightning attachment.

A model can be defined as a physical or mathematical construct which approximates to some degree certain aspects of natural or man-made phenomena. There are basically three levels of sophistication in the mathematical modeling of lightning.

The simplest lightning channel model, which provides the closest approximation to nature, assumes a temporal and spatial form for the channel current and then uses the current to calculate the remote fields. A more sophisticated approach involves mathematically describing the lightning channel as an RLC transmission line with distributed circuit elements that may vary with height and time. The intent there is to predict a channel current as a function of height and time, and to use this current to calculate the fields. The most sophisticated modeling method attempts to describe the detailed physics of the lightning channel using equations of conservation of mass, momentum, and energy, equations of state and Maxwells' equations (Ref. B6). Our interest in the several models is to find a valid description of the lightning channel geometry which could serve as the basis from which to find a reasonable experimental model.

For our study we chose to expand on the models used by Yang and Lee (Ref. B8). These lightning models were relatively sophisticated and used channel geometries that were amendable to experimental implementation. In addition, since the natural frequencies of a post attached to a lightning return strike were calculated analytically in the above report, the natural frequencies of a post attached to a lightning return stroke determined experimentally could be compared, thus providing a method to check the validity of the experimental model.

Yang and Lee used three lightning models, of which two were special cases of the third. The first model considered was the resistive model of Volland (Ref. B9) who showed that a lightning channel and its surrounding corona could be represented by a finitely conducting rod with an effective radius. Such a

representation can be considered a transmission line (Ref. B10). The required parameters are the effective radius r_e and the effective resistance per unit length R' . In terms of these two parameters the lightning channel has a characteristic impedance

$$Z_C^r(s) = \frac{Z_0}{2} \psi_s^r, \quad \psi_s^r = \left\{ \left[\ln \frac{sr_e}{c} \right]^2 - \frac{2\pi R' \ln \left(\frac{sr_e}{c} \right)}{s\mu_0} \right\}^{1/2} \quad (B1)$$

where s is the complex frequency, and Z_0 , c , μ_0 are the free-space wave impedance, speed of light, and permeability.

The corona-sheath model has been suggested in Reference B11 for a lightning channel and its surrounding corona. The lightning current flows only in the perfectly conducting center channel, while all the electric charges reside on an effective corona surface. The required parameters for the corona-sheath model are the effective radius of the lightning center channel r_0 and the effective radius of the corona surface r_c . The effective corona radius r_c is related to the charge per unit length of the corona via

$$r_c = \frac{|Q'|}{2\pi\epsilon_0 E_b}$$

where E_b and ϵ_0 are the air breakdown electric field and permittivity of the surrounding air respectively. This model can also be considered as a transmission line with characteristic impedance

$$Z_C^c(s) = \frac{Z_0}{2\pi} \psi^c(s), \quad \psi^c(x) = \left\{ \ln \left(\frac{sr_0}{c} \right) \ln \left(\frac{sr_c}{c} \right) \right\}^{1/2} \quad (B2)$$

A composite of the two above models, the resistive-corona sheath model, is the same as the corona sheath model except now the center channel can have a finite resistivity.

The geometries of the theoretical lightning models described were conducive to constructing experimental models, but materials from which to make the models were not available. The resistive-model could be simulated by a wire or string of appropriate size and resistivity. Wires were available with the properly scaled physical dimensions but wires with appropriate

conductivity were not. Yang and Lee evaluated the natural frequencies of a post attached to lightning channels of several different values of DC resistance per unit length. The appropriate value of natural lightning channel resistance is still a subject of much research. Thus, we would like to have experimental models with several values of channel resistance.

When the dimensions and resistivities of the lightning channels evaluated in the Yang and Lee work were appropriately scaled to correspond to the frequency range of our experimental facility, it was found that wires with DC resistances of 0.576 to 5760 Ω /ft would be necessary to duplicate the situations. The only available wires of the appropriate diameter had DC resistances varying from ~ 0 to 16.4 Ω /ft. Thus, our intent to simulate the frequency domain effect of lightning using a wire attached to a post protruding from a ground plane inside the chamber was impossible to achieve.

Measurements were, however, made with the available wires to see if the small variation in DC resistance had any effect on the response of the wires in the anechoic chamber. The wires are listed in Table B1. The same plane (c.f. Fig. 8, Sec. 3) used in the ground plane study of the F-106 was employed. One end of each wire sample was soldered to the center of a coaxial protruding from the center of the ground plane and the other was attached to a metal rod which was then stuck inside an absorber cone on the side of the chamber. The wires were illuminated with a plane wave whose electric vector was along the wire axis. The plane wave frequency was stepped from 118 to 4400 MHz and the magnitude and phase of the voltage feeding the network analyzer (50 Ω system) was recorded. The wire was then replaced by an MGL-8 B-dot sensor and the measurements repeated. Dividing the wire measurement by the MGL-8 measurement and making the response correction for the MGL-8 gives the wire response in terms of V/H_0 , where H_0 is the incident magnetic field.

A plot of the response of wire G with a DC resistance per unit length of ~ 0 Ω /ft is shown in Figure B1. A plot of the response of the wire D with a DC resistance per unit length of 16.4 Ω /ft is shown in Figure B2. From the plots it is evident that changing the resistance per unit length from ~ 0 Ω /ft to 16.4 Ω /ft has little effect on the response of the wire. The data plotted in Figures B1 and B2 have been digitally filtered with a routine which preserves 100 cycles per plot to reduce noise in the measured data.

Examination of Figures B1 and B2 shows that the phase of the wire response increases linearly with frequency. The amplitude of the wire response decreases linearly from 118 MHz to approximately 2500 MHz and then becomes fairly constant. A periodic standing wave pattern is super-imposed on the wire response and can be related to the wire length and current reflections at each end of the wire even though the tip of the wire was embedded in the absorber of the chamber wall. The responses of wires A through G were virtually the same.

As a result of these measurements we could essentially only implement the resistive model in the case of a conducting channel of infinite conductivity. To go further it is necessary to find new wire materials or other structures with which to implement the corona-sheath and resistive corona-sheath models. It has been suggested* that plastic tubing filled with a conducting electrolyte solution could be suitable for the corona-sheath model since the channel resistance could be changed by changing the electrolyte solution.

Evaluating the effect of a lightning attachment on the natural frequencies of an aircraft in the frequency domain experimentally using scale models in the anechoic chamber shows promise. However, more work needs to be done to find valid experimental models of lightning channels.

TABLE B1. LIST OF WIRES TESTED

Wire	Composition/Alloy	Gauge	Diameter (mm)	μ /ft
A	Nichrome	27	0.4064	3.19
B	Nichrome	32	0.2286	10.58
C	Chromel-A	29	0.3302	5.11
D	Chromel-A	34	0.1778	16.4
E	Alumel	29	0.3302	1.71
F	Kanthal	29	0.3302	6.89
G	Copper	22	0.7112	-0

* Baum, C.E., personal communication, May 1984.

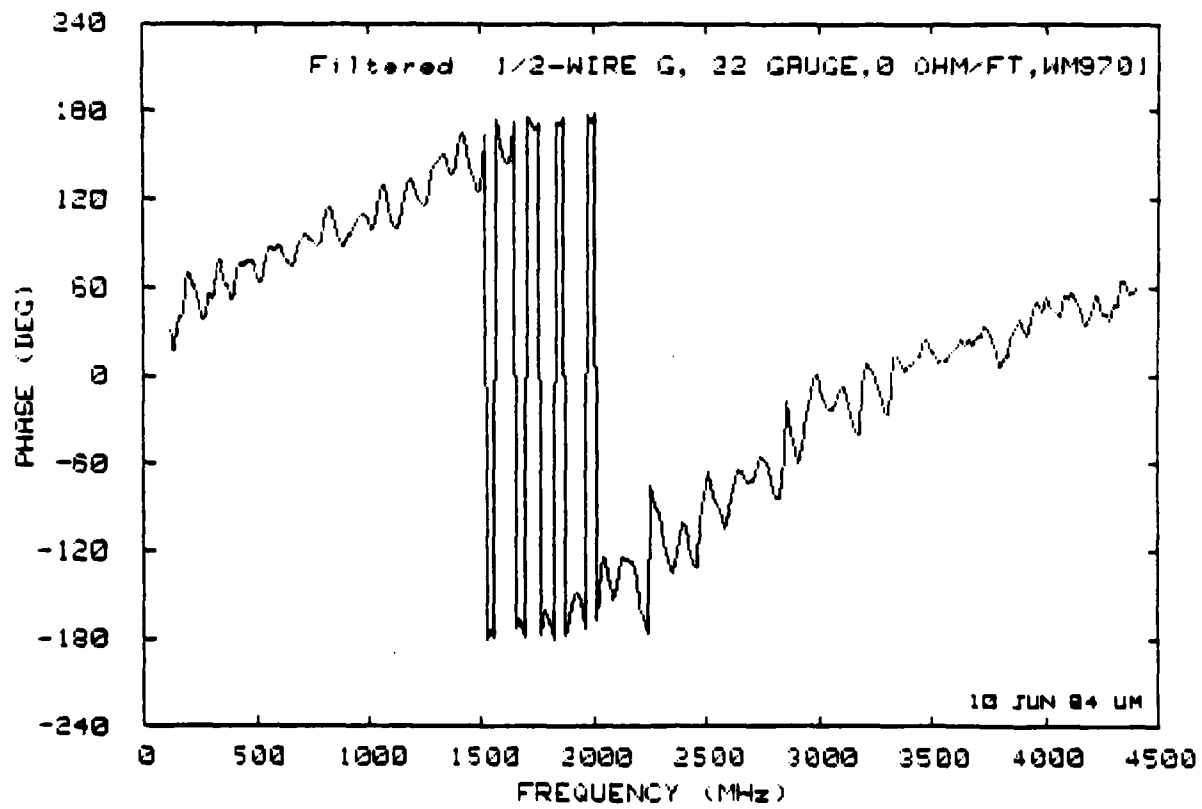
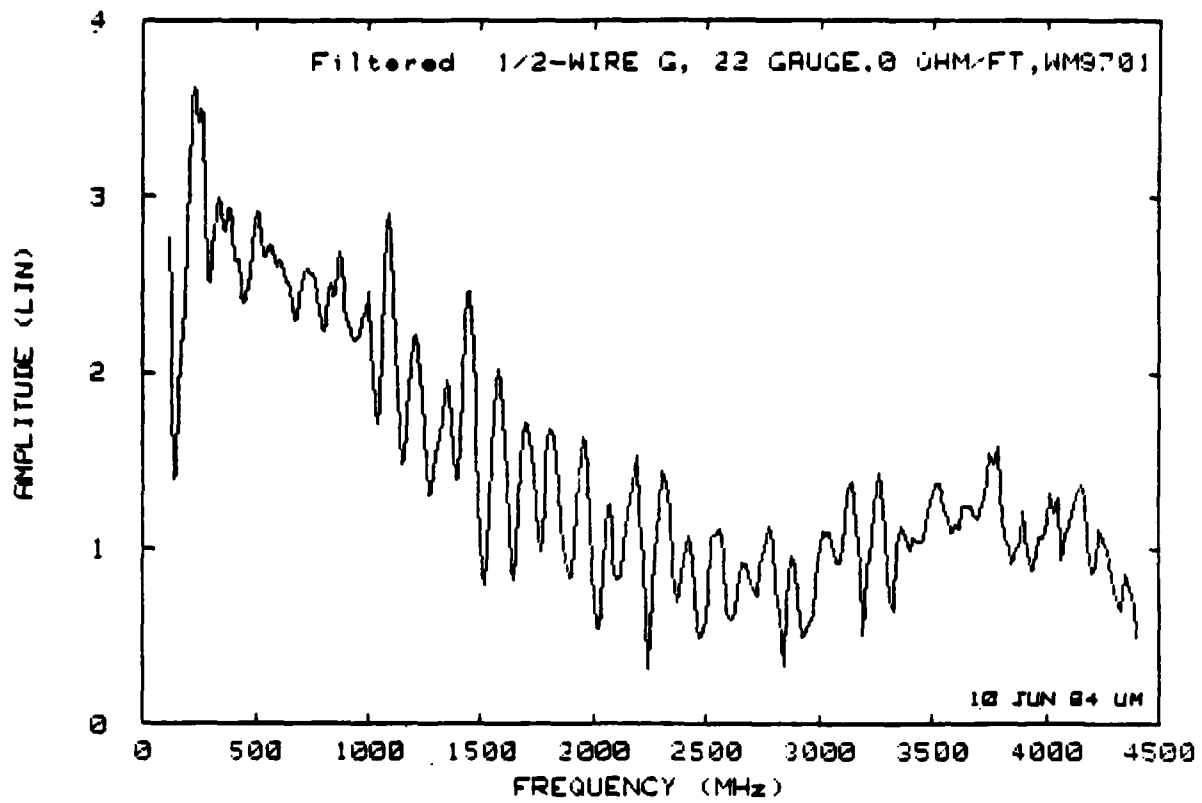


Figure B1. Voltage received by 22 gauge copper wire ($\sim 0 \Omega/\text{ft}$).

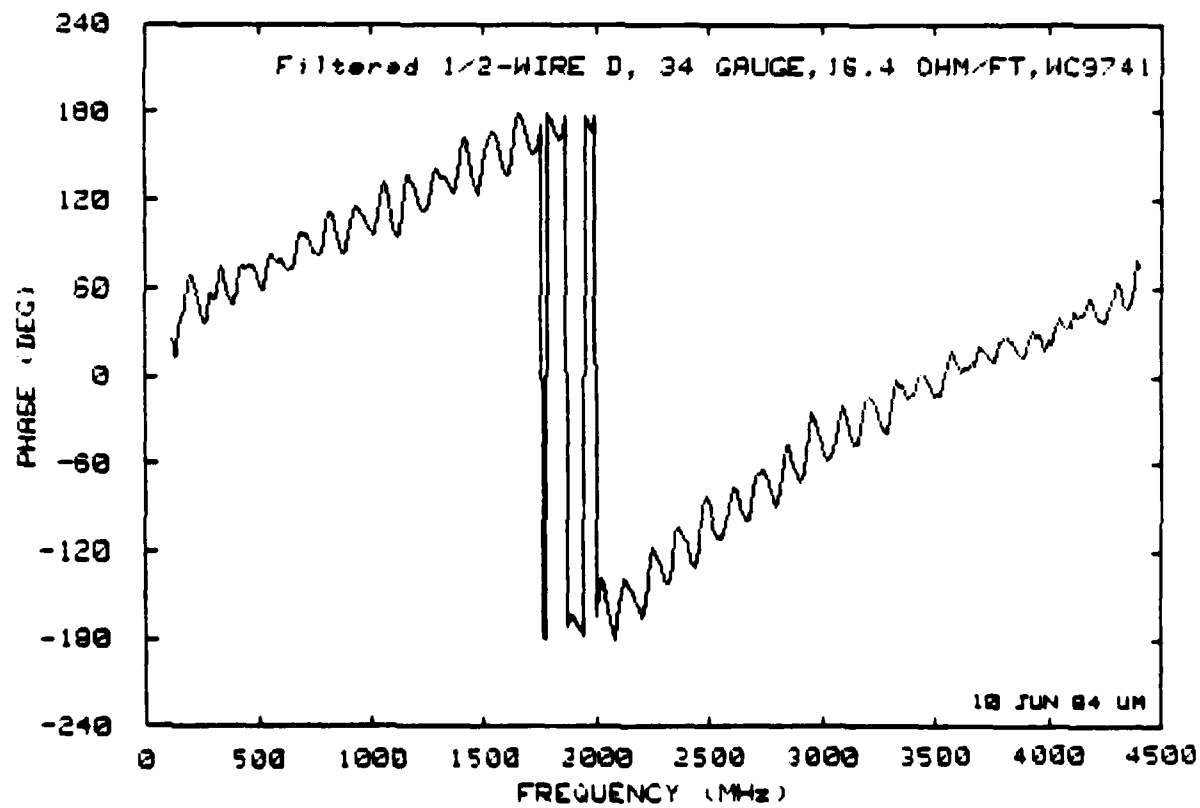
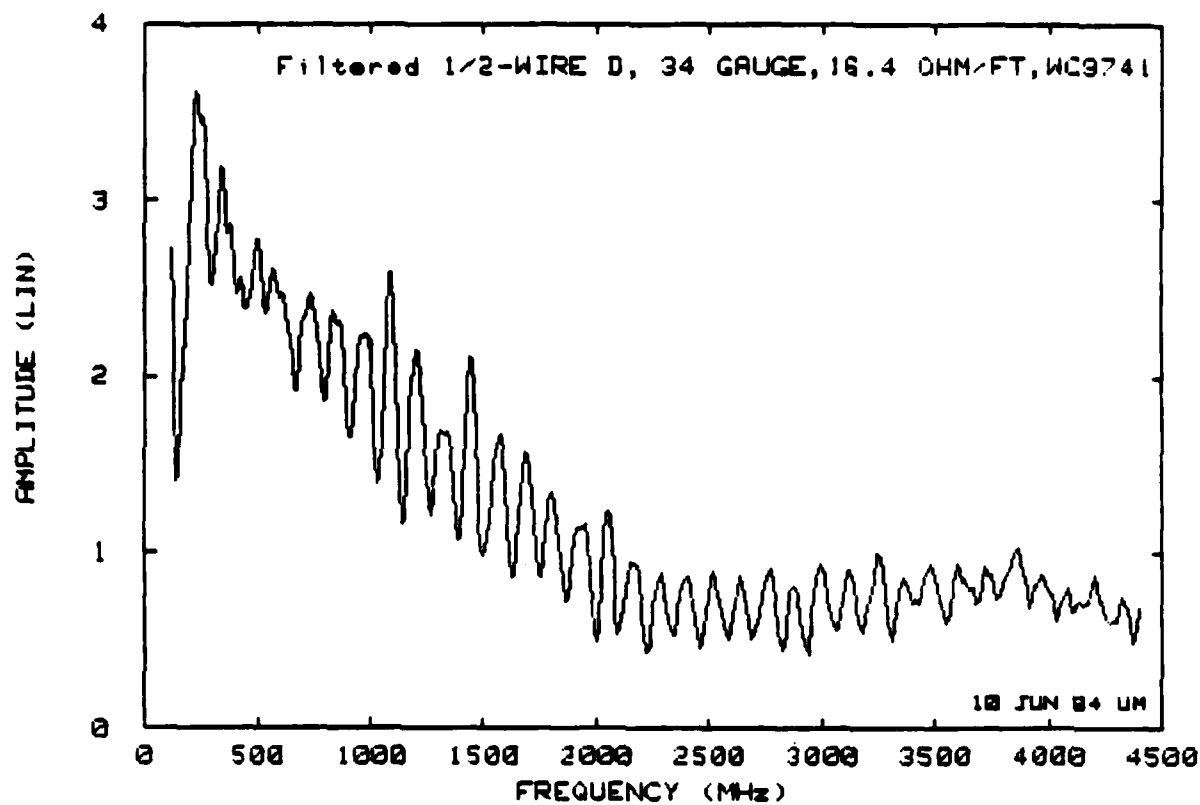


Figure 82. Voltage received by 24 gauge chromel-A wire (- 16.4 Ω /ft).

REFERENCES

APPENDIX B

- B1. Weidman, C.D. and E.P. Krider, "The Fine Structure of Lightning Return Strike Waveforms," J. Geophys. Res., Vol. 83, pp. 6239-6247, 1978.
- B2. Weidman, C.D. and E.P. Krider, "Submicrosecond Rise Times in Lightning Radiation Fields, in Lightning Technology," NASA Conf. Publ. 2128, FAA-RD-80-30, 1980b, pp. 29-38.
- B3. Weidman, C.D., E.P. Raider, and M.A. Uman, "Lightning Amplitude Spectrum in the Interval from 100 kHz to 20 MHz," Geophys. Res. Lett.; Vol. 8, pp. 931-934, 1981.
- B4. Baum, C.E., E.L. Breen, J.P. O'Neill, C.G. Moore, and D.L. Hall, "Measurement of Electromagnetic Properties of Lightning with 10 nanosecond Resolution in Lightning Technology," NASA Conf. Publ. 2128, FAA-RD-80-30, 1980, pp. 39-82.
- B5. Clifford, D.W., E.P. Krider and M.A. Uman, "A Case of Submicrosecond Rise Time Current Pulses for Use in Aircraft Induced Coupling Studies," presented at 1979 IEEE-EMC Conf., IEEE Rep. 77CH-1383-9 EMC, Library of Congress Catalog No. 78-15514.
- B6. Uman, M.A. and E.P. Krider, "A Review of Natural Lightning: Experimental Data and Modeling," IEEE Trans. on Electromagnetic Compatibility, Vol. EMC-24, No. 2, pp. 79-112, May 1982.
- B7. Clifford, D.W. and H.W. Kasemir, "Trigger Lightning," IEEE Transactions on Electromagnetic Compatibility, Vol. EM2-24, No. 2, pp. 112-122, May 1982.
- B8. Yang, F.C. and K.S.H. Lee, "Natural Frequencies of a Post Attached to a Lightning Return Stroke," Air Force Weapons Laboratory, DC-TR-1026.310-3*, April 1983.
- B9. Vollano, H., "A Waveguide Model of Lightning Currents and Their Electromagnetic Field," on Lightning Technology, NASA Conf. Publ. 2128, FM-RD-80-30, pp. 3-18, April 1980.
- B10. King, R.W.P., et al., Antennas in Matter, The MIT Press, Cambridge, MA, 1981.
- B11. Baum, C.E., "Properties of Lightning Leader Pulses," Lightning Phenomenology Notes, Note 2, Air Force Weapons Laboratory, Kirtland AFB, New Mexico, December 1981.

* Draft

END

10-86

DTIC